THE BEAUTY AND CHARM PRODUCTION CROSS SECTIONS IN 250 GEV/C PION-NUCLEON INTERACTIONS

Christopher Lynn Darling

Yale University

1993

ABSTRACT

THE BEAUTY AND CHARM PRODUCTION CROSS SECTIONS IN 250 GEV/C π^+-NUCLEON INTERACTIONS

Christopher Lynn Darling
Yale University
May 1993

By determining the production cross sections for heavy flavor hadrons, we test the theoretical predictions from perturbative quantum chromo-dynamics (QCD). In the case of pion induced beauty production, the few published results do not resolve the issue of the applicability of perturbative QCD. This analysis is undertaken in order to help resolve this situation. We determine the total beauty and charm production cross sections using an analysis of single electron decay products. We extract the cross sections per nucleon from the two-dimensional distribution of electron p_T^2 versus impact parameter (d) to the primary vertex. We place an upper limit on the beauty production cross section of $\sigma_{b\bar{b}} < 105$ nb at the 90% confidence level, where the limit includes both statistical and systematic errors. The charm production cross section is determined to be $\sigma_{c\bar{c}} = 13.9^{+2.4}_{-2.3}(\text{stat})\pm 1.8(\text{syst})$ μb, which is in good agreement with next-to-leading order QCD predictions and other measurements.

THE BEAUTY AND CHARM PRODUCTION CROSS SECTIONS IN 250 GEV/C π^+-NUCLEON INTERACTIONS

A Dissertation
Presented to the Faculty of the Graduate School
of
Yale University
in Candidacy for the Degree of
Doctor of Philosophy

By
Christopher Lynn Darling
May 1993

The Fermilab E769 Collaboration

G.A. Alves,[1] J.C. Anjos,[1] J.A. Appel,[2] S.B. Bracker,[5] L.M. Cremaldi,[3]
C.L. Darling,[8] R.L. Dixon,[2] D. Errede,[7] H.C. Fenker,[2] C. Gay,[5] D.R. Green,[2]
R. Jedicke,[5] D. Kaplan, [4] P.E. Karchin,[8] S. Kwan,[2] I. Leedom,[4]
L.H. Lueking,[2] G.J. Luste,[5] P.M. Mantsch,[2] J.R.T. de Mello Neto,[1]
J. Metheny,[6] R.H. Milburn,[6] J.M. de Miranda,[1] H. da Motta Filho,[1]
A. Napier,[6] A.B. d' Olivera, A.C. dos Reis,[1] S. Reucroft,[4] W.R. Ross,[8]
A.F.S. Santoro,[1] M. Sheaff,[7] M.H.G. Souza,[1] W.J. Spalding,[2] C. Stoughton,[2]
M.E. Streetman,[2] D.J. Summers,[3] S.F. Takach,[8] Z. Wu[8]

[1] *Centro Brasileiro de Pesquisas Físicas, Rio de Janeiro, Brazil*
[2] *Fermi National Accelerator Laboratory, Batavia, Illinois, 60510*
[3] *University of Mississippi, University, MS 38677*
[4] *Northeastern University, Boston, MA 02115*
[5] *University of Toronto, Toronto, Ontario, Canada, M5S 1A7*
[6] *Tufts University, Medford, MA 02155*
[7] *University of Wisconsin, Madison, WI 53706*
[8] *Yale University, New Haven, CT 06511*

Acknowledgements

During the last seven years, I have benefited greatly from new friends and mentors. I have earned this degree because of the encouragement they have given me; for this and more they have my deepest thanks.

Foremost, I thank Aylâ, who was always there to give comfort, love and physics lessons. I never thought I would fall in love with a physicist...you have proven me wrong. A special thanks to mom and dad for their encouragement and love. You were right.

I have had the honor of working with many fine people both at Yale and Fermilab. Above all, I thank my advisor, Paul Karchin, for showing me how to think and being an outstanding example of a physicist. I also thank the E769 collaboration, particularly Jeff Appel and Jeff Spalding, for sharing their physics expertise. It has been a privilege working with all of them.

For wonderful times both at work and play, I thank Abhay Deshpande, Vinay Singh, Brian Lund, Ali Serpengüzel, Randy Hans, Moe Foucher, Steve and Cindy Takach, Ali Rafatian, Lee Lueking, Mika Masuzawa, Bryan MacKinnon, Rob Harr, Chris Liapis, ZhongXin Wu, Bill Ross, Karen Ohl, Frank Rotondo, Ram Ben-David, Jeff Snyder, Doug Bergman, John Sinnott and Dick Majka. Additionally, I would like to thank Elliott Wolin for advice in all matters of life and for many a game on the much-too-big racquetball court. I thank Jean Slaughter for acting as my advisor-by-proxy while I was at Fermilab. I thank Sara Batter and Jean Belfonti without whom I could not have survived all of these years. Thanks also to Rochelle Lauer for her friendship and help in finding me half a million blocks here and there. Thanks to Dr. Christopher Alliegro for inspired discussions of the ξ parameter. A special thanks

to Lisa Chen-Tokarek for her exceptional organizational skills. Final thanks to Peter Martin for all he did to make graduate student life bearable. He is a master of his trade.

Contents

List of Figures

List of Tables

Chapter 1

Introduction

1.1 The Standard Model

The standard model (SM) of strong and electroweak interactions is based on a local $SU(3)_c \otimes SU(2)_L \otimes U(1)_Y$ gauge symmetry and describes all known particles and their observed interaction properties, excluding the gravitational interaction. As a result, it is the standard against which new experimental results are compared. The observed physics of the SM can be described by the interaction of the set of spin-$\frac{1}{2}$ fermions which are the charged leptons (e, μ and τ), their neutrinos (ν_e, ν_μ and ν_τ), the six quarks (u, d, s, c, b and t), each coming in three "colors", and the corresponding antiparticles. There is evidence supporting the existence of all of these fermions except for the t quark, which is postulated, and the τ neutrino, for which the evidence is indirect.

The interactions between the fermions are mediated by a set of spin-1 gauge bosons. These are the photon (γ) and the massive intermediate vector bosons ($W^\pm$ and Z^0) for the $SU(2)_L \otimes U(1)_Y$ electroweak sector and the eight massless gluons (g) which couple the $SU(3)_c$ color charge of quarks and mediate the strong interaction described by quantum chromo-dynamics (QCD).

The fermions are grouped into generations, or families, as shown in Table 1.1. This suggests a structure associated with the mass of the fermion, where the first generation consists of the lightest fermions. Each generation consists of a massive lepton,

its corresponding neutrino and two quarks. The quarks are further subdivided by their coulomb charge, with each generation having one quark of each charge. The neutrinos participate only in the weak interaction; the massive leptons participate in the electromagnetic and weak interactions; the quarks participate in all three interactions. This is demonstrated in the table by the columns associated with coulomb and color charge, where, for example, the electron neutrino has zero coulomb charge and is therefore not affected by the electromagnetic force. The column labelled Color *dof* represents the number of color degrees of freedom for the given particle.

Table 1.1: Properties of the three generations of fermions, the gauge bosons and the Higgs scalar.

Particle	Symbol	Spin	Coulomb charge	Color *dof*	
Electron neutrino	ν_e	1/2	0	0	
Electron	e	1/2	-1	0	First
Up quark	u	1/2	2/3	3	Generation
Down quark	d	1/2	-1/3	3	
Muon neutrino	ν_μ	1/2	0	0	
Muon	μ	1/2	-1	0	Second
Up quark	c	1/2	2/3	3	Generation
Down quark	s	1/2	-1/3	3	
Tau neutrino	ν_τ	1/2	0	0	
Tau	τ	1/2	-1	0	Third
Up quark	t	1/2	2/3	3	Generation
Down quark	b	1/2	-1/3	3	
Photon	γ	1	0	0	
W Boson	$W^\pm$	1	± 1	0	Gauge
Z Boson	Z^0	1	0	0	Bosons
Gluon	g	1	0	8	
Higgs scalar	H	0	0	0	

If the physics of the electroweak sector were completely described by the symmetry $SU(2)_L \otimes U(1)_Y$, all fermions and gauge bosons would be massless [1]. Since this is not the case, we say this symmetry is spontaneously broken by invoking the Higgs mechanism. In the minimal SM, this introduces a complex scalar doublet, which breaks down the symmetry and gives the particles their masses. The masses are

essentially free parameters to be determined by experiment, and provide a measure of each particle's coupling to the scalar doublet. The result of this explanation of the particle masses requires that there be a massive scalar boson known as the Higgs boson. The Higgs boson does not couple to the photon or the gluons, thus they remain massless. An equivalent statement is that the Higgs boson has no electromagnetic or color charge. There is no direct experimental evidence supporting the existence of the Higgs boson and experimental searches rule it out in the mass range $M_H < 48$ GeV/c^2 [2].

In QCD, quarks are confined to bound states with other quarks such that free quarks are never observed. This is explained by the color charge symmetry in which each quark comes in three colors (red (R), green (G) and blue (B)), while each anti-quark comes in three anti-colors ($\bar{R}, \bar{G}$ and $\bar{B}$). All observable hadronic states are combinations of quarks and anti-quarks which are colorless. The two simplest examples of such states are three quarks, qqq, each of a different color ($R + G + B$ =colorless) and one quark and one anti-quark, $q\bar{q}$, of opposite colors (for example $R + \bar{R}$ = colorless). More complex states such as $qqqq\bar{q}$ are not forbidden by QCD, but have not yet been observed.

The quarks are referred to by names: up, down, charm, strange, truth(top) and beauty(bottom) for u, d, c, s, t and b respectively. In further discussions, beauty and charm quarks are collectively referred to as heavy quarks, while their hadrons are called heavy hadrons. The production of heavy quarks is governed by QCD which, unlike the electroweak sector, has only one free parameter: the characteristic QCD energy scale denoted by Λ, which is known to be $\sim$200 MeV. The equations of motion of the QCD Lagrangian cannot be solved exactly, so QCD predictions for production cross sections are made through a perturbative expansion of the invariant parton cross section (see Eq. 1.1). The expansion series is made in the QCD running[1] coupling constant $\alpha_s(\mu^2)$. The energy scale is determined by μ, the renormalization scale, which is chosen to be of the order of the produced heavy quark mass.

[1]A running constant is one that has different values at different energies, μ.

1.2 Pion Induced Heavy Quark Production

In this analysis, we will measure the total pion induced beauty and charm production cross sections and compare them to the theoretical predictions. These measurements therefore test the applicability of perturbation theory to QCD. The total cross section for the inclusive production of a heavy quark pair, $Q\bar{Q}$, due to a hadron-hadron collision can be expressed as

$$\sigma_{Q\bar{Q}}(S) = \sum_{i,j} \int dx_1 dx_2 \hat{\sigma}_{ij}(x_1 x_2 S, m^2, \mu^2) F_i^A(x_1, \mu) F_j^B(x_2, \mu). \tag{1.1}$$

Fig. 1.1 expresses this equation in the form of a diagram. The hadrons, labelled A and B, each contribute one parton, labelled i and j, to the processes by which the heavy quark pair is produced. In the equation, m is the heavy quark's mass, μ is the renormalization energy scale, S is the square of the hadron-hadron center of mass (CM) energy and $x_{i,j}$ are the hadron's momentum fraction possessed by its parton (i,j).

This interaction is divided into three parts, the first of which, called fragmentation, is expressed in the figure only. This is the process by which the outgoing partons (including the heavy quark pair) are formed into hadrons. We understand very little about this process, which is also known as hadronization, because it is dominated by low momentum transfer processes which preclude the use of perturbation theory. Because one experimentally measures the production properties of hadrons, not quarks, it is important that we understand the effects of fragmentation. This is discussed in more detail in Section 1.3 and in Chapter 6 when experimentally derived information is used to describe charm and beauty fragmentation.

The second part of the interaction describes the parton momentum distributions within the beam and target hadrons. This is done via the structure functions $(F_{i,j})$, which are determined from experiment and evolved to the renormalization scale μ. This is discussed further when we introduce the structure functions used for the theoretical cross section predictions.

The final part of the interaction is represented by $\hat{\sigma}$, which is the total short-distance cross section for the production of the heavy quark pair. This is the part of

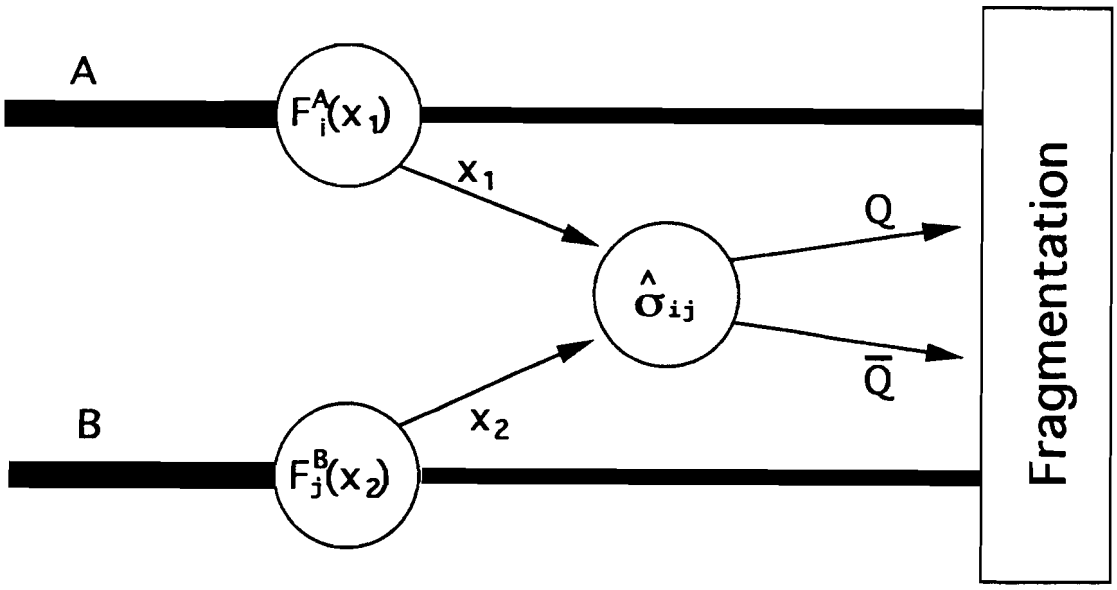

Figure 1.1: Heavy quark production via a hadron-hadron collision.

the interaction that can be calculated from perturbation theory, which is discussed below.

Total heavy quark production cross section calculations for pion-nucleon and proton-nucleon interactions complete to $\mathcal{O}(\alpha_s^3)$ are published [3, 4, 5]. The calculations are composed of the leading order (LO) diagrams shown in Fig. 1.2 and their radiative corrections (Next to Leading Order - NLO), examples of which are shown in Fig. 1.3. In Fig. 1.3a, the diagrams include the emission and absorption of a virtual gluon. These diagrams interfere with the leading order diagrams to contribute to $\mathcal{O}(\alpha_s^3)$. Fig. 1.3b shows examples of real gluon emission which contribute directly to $\mathcal{O}(\alpha_s^3)$. In addition to the radiative corrections, a new set of diagrams enter at the order α_s^3. These are known as quark-gluon scattering diagrams and look like $qg \rightarrow qQ\bar{Q}$.

Fig. 1.4 and Fig. 1.5 show the perturbative QCD predictions of the pion induced production cross sections for charm and beauty respectively as a function of beam

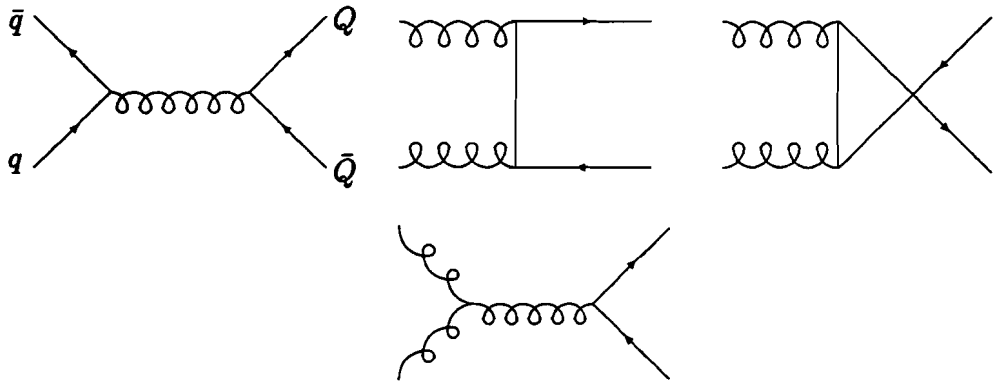

Figure 1.2: The leading order diagrams for the production of a heavy quark pair.

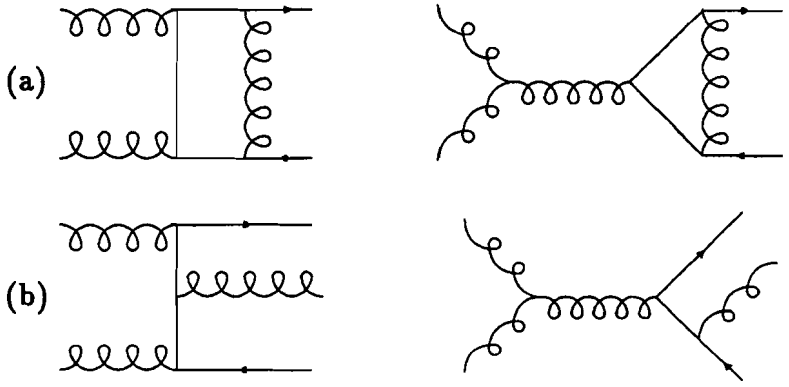

Figure 1.3: Examples of next-to-leading order diagrams for the production of a heavy quark pair.

momentum. The calculations use $m_c = 1.5$ GeV/c^2, $m_b = 4.75$ GeV/c^2, $\Lambda = 200$ MeV and $\mu = m_Q$. The Duke and Owens [7, 8] set 1 parton distribution functions are used for the pion and nucleon. These functions are determined by an analysis of experimental results from deep-inelastic lepton-nucleon scattering, high mass di-lepton distributions and J/ψ x_F distributions (the Feynman-x variable is defined to be $x_F = \frac{p_\parallel}{p_{\parallel\, max}} \simeq \frac{2p_\parallel}{\sqrt{S}}$). For these figures, the solid line is the LO+NLO prediction, while the dashed curve is the LO prediction. The large increase in the charm cross section compared to beauty is expected when including NLO terms because

$$\alpha_s(\mu^2) \propto \frac{1}{2 \times \ln(m_Q/\mu)}, \tag{1.2}$$

where m_Q is the heavy quark mass. Smaller quark masses give larger values of α_s, which in turn means that higher order corrections are more important because α_s is the perturbative expansion coefficient.

The NLO prediction is not a perfect predictor of the total cross sections for several reasons. First, there is the uncertainty introduced by the value chosen for Λ. The value of Λ is constrained by experimental measurements of α_s, and can be anywhere from 150 to 350 MeV. Second, there is the uncertainty due to the structure functions of the initial state hadrons. This can be estimated by contrasting the cross section results derived from different structure functions. A third source of error is introduced by the choice of μ. At NLO accuracy [5], small changes in μ around the value of m_Q introduce errors of $\mathcal{O}(\alpha_s^4)$. Similarly, for n^{th} order the errors are $\mathcal{O}(\alpha_s^{n+1})$. Thus, the uncertainty due to μ decreases as more terms are included in the perturbative expansion, such that the cross section calculated to all orders is independent of μ. There are schemes [5] for choosing an optimal value for μ, e.g., the "minimal sensitivity" scheme. In this case, μ is chosen such that $d\sigma/d\mu = 0$, where σ is the NLO cross section prediction. Typically, these schemes give values of μ near m_Q, and the renormalization scale sensitivity is usually estimated by varying μ from $m_Q/2$ to $2m_Q$.

The fourth contributor to the cross section uncertainty is due to the uncertainty of the the heavy quark mass. This becomes very important near the production threshold for the heavy quark pair. The quark mass is tuned to match experimental measurements with $m_c = 1.2 - 1.5$ GeV/c^2 and $m_b = 4.5 - 5$ GeV/c^2. The remaining

contributor to the cross section uncertainty comes from the calculation method itself. Since the cross section is calculated via a perturbative expansion, there are always higher order corrections. Above the lowest orders, the number of terms that must be included becomes so unwieldy that higher order calculations are extremely difficult. Without actually performing the calculations for the higher order terms, their contribution can only be estimated. Estimates of the theoretical uncertainties due to all of the above items are made in References [3, 5, 6]. For both charm and beauty, the total cross section prediction typically varies by a factor of two to four as a function of lab momentum as a result of the above mentioned uncertainties. In subsequent plots of the total cross sections, the NLO predictions will be shown with uncertainty estimates of a factor of two in order to set a scale of reliability for comparing to experimental results.

At a lab momentum of 250 GeV/c for the pion (which is 21.7 GeV in the CM frame), the dominant mechanisms contributing to beauty and charm production are different. Because only a fraction of the pion-nucleon CM energy is involved in the parton-parton interaction which produces the heavy quark pair, beauty production occurs near threshold ($\sim 2 \times m_B \simeq 10$ GeV). Near threshold, the dominant contribution comes from quark anti-quark annihilation. At 21.7 GeV, this contributes approximately 2/3 of the total cross section, while gluon-gluon fusion contributes the balance. The contribution of the quark-gluon scattering diagrams is negligible. For charm production at 21.7 GeV, we have a very different situation as this is far above the heavy quark pair production threshold. The gluon-gluon fusion diagrams contribute 97% of the cross section, while the balance is due to quark anti-quark annihilation. Again, quark-gluon scattering contributions are negligible.

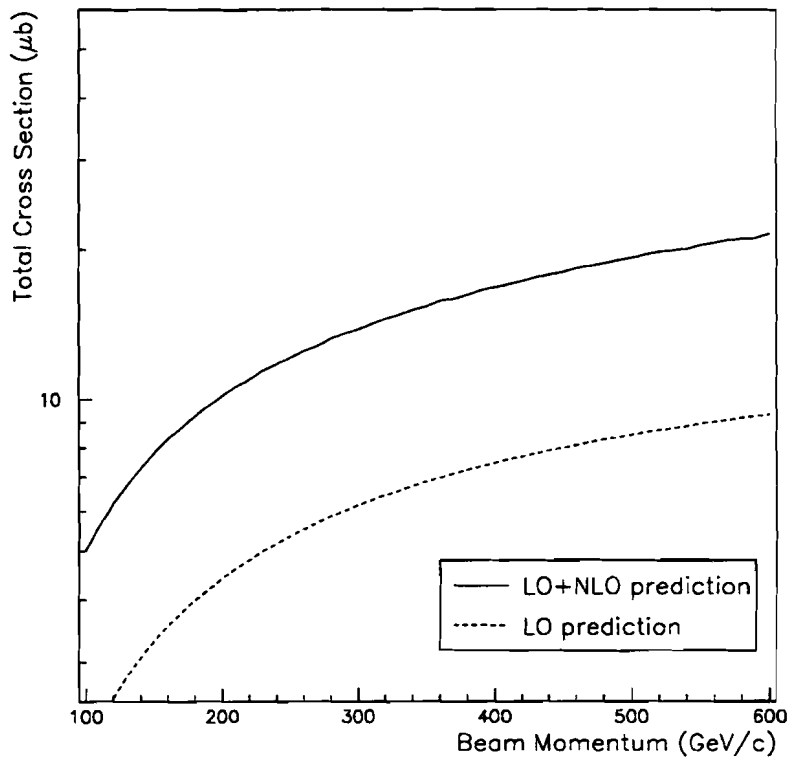

Figure 1.4: The perturbative QCD cross section prediction for $\pi N \rightarrow c\bar{c}$ as a function of beam energy.

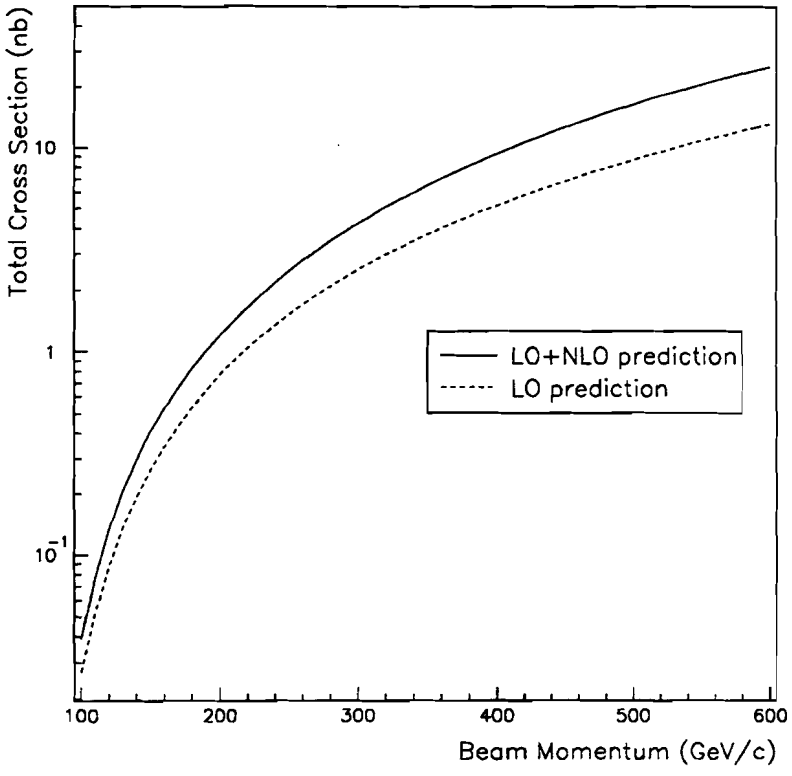

Figure 1.5: The perturbative QCD cross section prediction for $\pi N \rightarrow b\bar{b}$ as a function of beam energy.

1.3 Review of $\pi^{\pm}$ Induced Heavy Quark Production Results

If the SM is to continue as the theory that explains the observable interactions of all elementary particles, perturbative QCD to some order must correctly predict experimentally measured cross sections for $\pi^{\pm}N \rightarrow Q\bar{Q}$ within theoretical uncertainties. In the case of charm, this assumes that the charm quark mass is large enough, and consequently that the perturbative expansion coefficient (see Eq. 1.2) is small enough, for the series to converge. Thus, measurement of these cross sections is a test of QCD.

1.3.1 Pion Induced Charm Production

Recently published measurements (see Table 1.2) of exclusive decays of charged and neutral D mesons produced at $x_F > 0$ from pion induced interactions can be used to test the SM predictions. The E769 measurement shown in the table is preliminary and is not yet published.

Table 1.2: Recent measurements of the pion induced open charm cross section.

Experiment	Meson	$\sigma(\pi^{\pm}N \rightarrow D + X, x_F > 0)\mu$b/nucleon	Reference
NA32	all D	$6.7^{+0.8}_{-0.7} \pm 0.4$	[9]
200 GeV/c π^-			
NA32	$D^0/\bar{D}^0$	$6.3 \pm 0.3 \pm 1.2$	[9]
230 GeV/c π^-	$D^{\pm}$	$3.2 \pm 0.2 \pm 0.7$	
E769	$D^0/\bar{D}^0$	$7.43 \pm 0.27 \pm 0.33$ (preliminary)	[10]
250 GeV/c $\pi^{\pm}$	$D^{\pm}$	$3.84 \pm 0.70 \pm 0.45$ (preliminary)	
NA27	$D^0/\bar{D}^0$	10.1 ± 2.2	[11]
360 GeV/c π^-	$D^{\pm}$	5.7 ± 1.5	
E653	$D^0/\bar{D}^0$	$22.05 \pm 1.37 \pm 4.82$	[12]
600 GeV/c π^-	$D^{\pm}$	$8.66 \pm 0.46 \pm 1.96$	

To compare with the theoretical prediction, we must convert the experimental measurements into estimates of the total production cross section. We do this based

on two approximations. First, we estimate the fraction of charm produced in the region defined by $x_F > 0$. From this, the data can be converted into estimates of charm production for all x_F. Reference [3] shows the NLO charm cross section prediction as a function of x_F in the range $x_F > 0$ for pion-proton interactions at $\sqrt{S} = 23$ GeV. This distribution peaks at $x_F \simeq 0.05$ and is approximately symmetric about the peak. Furthermore, we note from reference [41] that the LO x_F distributions[2] do not appreciably change over the range of $\sqrt{S}$ values for which data exists ($19.4 < \sqrt{S} < 33.6$ GeV). Each cross section measurement is then converted to an estimate for all x_F by multiplying the experimental measurement by a factor of two.

To convert the D meson production cross section measurements into estimates of the total charm cross section, we begin by expressing fragmentation as

$$\sum_{i=1}^{N_h} f(c \to X_i(c)) \equiv 1, \tag{1.3}$$

where N_h is the number of charm hadrons. The same expression holds for the $\bar{c}$ quark and $f(c \to X_i(c)) = f(\bar{c} \to X_i(\bar{c}))$ is assumed. We further assume that fragmentation is independent of $\sqrt{S}$ over the range for which data exists. The published measurements are made from decays of D^+ and D^0 (plus their charged conjugates) because most of the charm cross section involves the production of one of these mesons. In other words we can make the approximation,

$$\sum_{i=1}^{N_h} f(c \to X_i(c)) \simeq f(c \to D^+) + f(c \to D^0). \tag{1.4}$$

The charm cross section measurements in Table 1.2 are shown for both signs of meson, meaning that the results are for c and $\bar{c}$ quark production. Since each event with a charm quark must also have an anti-charm quark, the sum of the D meson cross sections overestimates the total cross section by a factor of two when using Eq. 1.4. Therefore, the total charm cross section is approximated by the sum of the production cross sections for charged and neutral D mesons produced in the $x_F > 0$ region:

$$\sigma(c\bar{c}) \simeq \sigma(D^+, x_F > 0) + \sigma(D^0, x_F > 0). \tag{1.5}$$

[2]LO predictions of the x_F distribution have been published for many values of $\sqrt{S}$. This is not true for NLO predictions.

This means that the two approximations tend to cancel one another out. It is the fragmentation approximation that introduces the larger uncertainty to this estimate. The x_F approximation is valid down to about 10%, while the fragmentation approximation is valid to about 30%. Therefore, the estimate of the cross section underestimates the actual production cross section by 20-30%.

Fig. 1.6 shows the NLO prediction for the charm production cross section with the theoretical uncertainty discussed earlier. Also included are the total cross section estimates from the recent measurements of the D meson production cross sections. One can see that these measurements are very close to the central value for the prediction. Therefore, perturbative QCD seems to be a good predictor for the pion induced charm production cross section. One expects this to be true for beauty too because the heavier quark mass makes for a faster converging perturbative series.

1.3.2 Pion Induced Beauty Production

There are fewer published results (see Table 1.3) for pion induced open beauty production compared to charm because the beauty cross section is so much smaller. These measurements are superimposed on the theoretical prediction of Fig. 1.7. The large error bars and spread of the central values around the prediction warrant another measurement. The WA75 result is based on one event seen in emulsion, therefore the production cross section is only an estimate. WA78 and NA10 analyze events with multiple high transverse momentum (p_T) leptons (muons in this case). By requiring two or more in an event, the minimum bias background is greatly reduced.

Historically, the results of the multiple lepton analyses have been viewed skeptically because the measurements are based on a small number of events. In addition, there are concerns about background processes (particularly muons from charm hadron decays) causing events to be mis-identified as beauty events. What follows is an argument we have used to test the published results. The two analyses above have different criteria by which muons from charm and beauty are distinguished. As an example we consider the NA10 analysis. The reaction under study is

$$\pi^- W \rightarrow B\bar{B}X \tag{1.6}$$

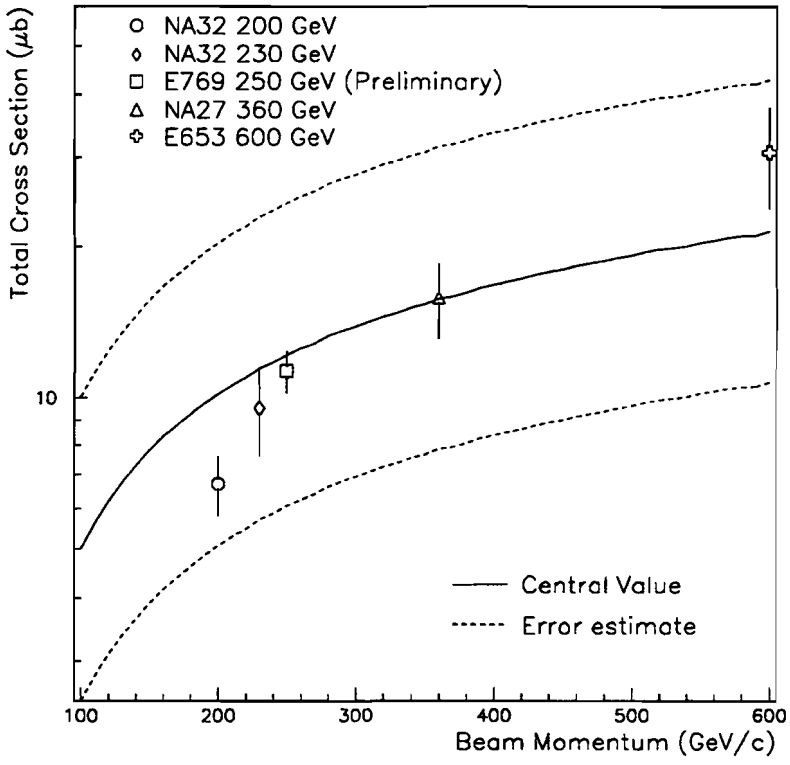

Figure 1.6: The NLO perturbative QCD cross section prediction for $\pi N \rightarrow c\bar{c}$ as a function of beam energy. Superimposed are the recent experimental measurements which are summarized in Table 1.2.

Table 1.3: Recent π induced open beauty cross section data.

Experiment	Measure	$\sigma(\pi^{\pm}N \rightarrow b\bar{b})$nb/nucleon	Reference
WA75	$B^-\bar{B}^0$	$\sim$10	[13]
350 GeV/c π^-	in emulsion		
WA78	like sign muons	$2.0 \pm 0.3 \pm 0.9$	[14]
320 GeV/c π^-	U		
NA10	tri-muons	14^{+7}_{-6}	[15]
286 GeV/c π^-	W		

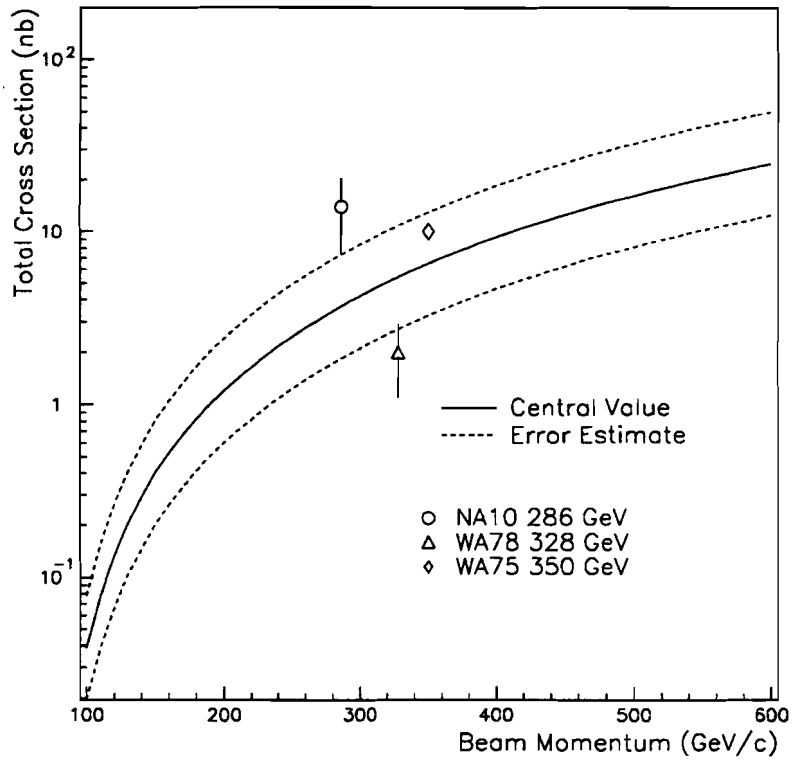

Figure 1.7: The NLO perturbative QCD cross section prediction for $\pi N \rightarrow b\bar{b}$ as a function of beam energy. Superimposed are the recent experimental measurements which are summarized in Table 1.3. The WA75 measurement is shown without an uncertainty.

where both B mesons decay semi-leptonically. In addition, at least one of the two mesons produces another muon via

$$B \rightarrow \mu^- D(\rightarrow \mu^+ X)X'$$
$$\bar{B} \rightarrow \mu^+ \bar{D}(\rightarrow \mu^- X)X'.$$

The NA10 trigger requires two muons having transverse momenta $p_T(\mu 1) > 0.8$ GeV/c and $p_T(\mu 2) > 1.4$ GeV/c. A search for a third muon is performed offline; it must have $p_T(\mu 3) > 0.5$GeV/c. Furthermore, they have stated [15], without further comment, that muons from charm do not cause the trigger to fire. This assumption needs investigation, as muons from charm can contribute to contamination of the trigger in two ways. One way this can occur (called Case 1 below) is through a beauty event in which a muon from beauty has $p_T > 1.4$ GeV/c and a muon from charm has $p_T > 0.8$ GeV/c. The other way (Case 2) is from a charm event in which both charm hadrons decay to muons that satisfy the trigger requirements. We can estimate these contaminations by calculating effective cross sections for the processes, expressed as $\sigma'(Q\bar{Q}) = \sigma(Q\bar{Q}) \times ACC(p_T(\mu 1) > 0.8, p_T(\mu 2) > 1.4)$, where ACC is the fraction of the time the two muons satisfy the trigger requirement. Case 1 can be immediately discarded as a significant background source because it requires a high p_T lepton from charm in addition to the beauty event. The NA10 beauty cross section is $\sim$14 nb. We have performed a Monte Carlo (MC) simulation of the trigger and found that only one out of 1000 leptons from charm decay have $p_T > 0.8$ GeV/c, putting $\sigma'(b\bar{b})$ in the picobarn range. The contamination of the beauty measurement due to case 1 is negligible.

To check the significance of the contamination from case 2, we have performed a MC simulation of charm quark events from 250 GeV/c pion-nucleon interactions, which is very close to the NA10 energy of 286 GeV/c. From this MC simulation we find $ACC = 2.8 \times 10^{-5}$. Assuming $\sigma(c\bar{c}) = 15\mu$b, this yields $\sigma'(c\bar{c}) = 15\mu$b $\times(2.8 \times 10^{-5}) = 0.42$ nb. Recalling their beauty cross section measurement is $\sim$14 nb, there is no significant contamination due to case 2 either.

This supports the argument that the multiple lepton analysis used by NA10 is is not contaminated by charm. This demonstrates that an analysis of single tracks

from a decay vertex can be used to extract a production cross section. This is the foundation upon which the analysis to be described in the next section is based.

1.4 Summary of the Analysis Technique

Because of the apparent successes of multiple lepton analyses used to extract the beauty cross section, we adopt a similar approach. In this analysis, the π^+ induced total beauty production cross section is determined from inclusive semi-leptonic decays of beauty hadrons. We do this by studying events with a single high p_T electron, which is where this analysis differs from the ones mentioned above. Normally, background processes would dominate a single lepton analysis such that a beauty cross section could not be extracted. However, in this case, we use a technique correlating electron p_T and impact parameter (d) to the production vertex. The analyses discussed above were not able to measure the electron's d. Our intention is to use this new information to reject a larger fraction background than would otherwise be possible.

In this analysis, we will measure both the beauty and charm production cross sections through a study of their semi-leptonic decays. At the quark level, the semi-leptonic decay of a heavy hadron proceeds as $Q \rightarrow Q'W^{\mp}$, where Q is a $b(c)$ quark, Q' is a $c(s)$ quark, and W is the virtual charged intermediate vector boson, which subsequently decays to an electron and an electron neutrino ($W^{\pm} \rightarrow e^{\pm}\nu_e(\bar{\nu}_e)$). The electrons from such decays are characterized by their p_T and miss distance, or impact parameter (d), to the production vertex. By correlating the p_T and d of the electron candidate through an analysis of the two dimensional distribution of electron p_T versus d, the number of electrons from both heavy quark types are determined without restricting the p_T range over which the electrons from charm can be produced (as is done in the NA10 analysis described above). Once a model is adopted describing how often each heavy quark type decays to an electron, the heavy quark cross sections can be calculated. This introduces a model dependency which will be discussed in more detail later. Because of the consistent agreement between theory and measurement in the case of charm (see Section 1.3), the charm measurement made in this analysis will

provide a check that the analysis technique is reliable. The values to which the results will be compared can be taken from the NLO QCD predictions from Figures 1.4 and 1.5. These values are $\sigma(c\bar{c}) \simeq 12\mu$b and $\sigma(b\bar{b}) \simeq 2$nb.

Chapter 2

Spectrometer

The analysis presented here is performed on data taken by Fermilab fixed target experiment E769 at the Tagged Photon Laboratory (TPL) from 1987-88. E769 uses a charged hadron beam of π, K and p incident on a multi-foil target in order to study the properties of charm hadro-production. The target is constructed of thin foils of Al, Be, Cu and W separated along the beam direction. The primary purpose of this experiment is to measure the atomic mass dependence, the differential cross section as functions of x_F and p_T of the charm hadron and the total charm production cross section. In each case, the study is performed for a particular beam type. The TPL apparatus [16, 17, 18] is a large forward acceptance spectrometer with good vertex resolution via a silicon microstrip detector (SMD). The calorimeters, muon wall, threshold Čerenkov counters and most of the drift chambers were used originally in E516; E691 added silicon planes and more drift chambers. Both previous experiments used a photon beam, E516 with a hydrogen gas target and E691 with a beryllium target. The E769 spectrometer differs from E691 in several ways:

- A 250 GeV/c hadron beam is used instead of a photon beam from bremsstrahlung of 250 GeV/c e^-.
- Tracking and identification of the beam particle are added.

- Two SMD planes downstream[1] of the target improve the vertex resolution.
- Proportional Wire Chambers (PWC) downstream of the target for improved tracking.
- The Data Aquisition (DA) System is redesigned to write data to tape at a rate of 1.8 MB/sec, which is a rate increase of 4.5 from E691.

This chapter is organized into sections devoted to each subsystem of the spectrometer and other items involving a general discussion of the apparatus. Throughout this chapter, the reader is referred to illustrations of the target and downstream regions of the spectrometer shown in perspective (Fig. 2.1) and cross section (Fig. 2.2) views.

2.1 The Accelerator and Beam

The hadron beam used in E769 is produced in a multi-stage process (see Fig. 2.3). This process begins with a negatively ionized hydrogen source which is accelerated to 750 keV/c by a Cockcroft-Walton accelerator. This beam, with a current of approximately 50 mA, is injected into a 200 MeV/c linear accelerator that operates at a frequency of 52 MHz. As a result, the ions are collected into buckets that are 2 ns wide and separated by 19 ns, a beam structure which is seen throughout the rest of the process. The hydrogen ions are then stripped of both electrons as they are injected into the booster stage which accelerates the protons to 8 GeV/c, with a beam current of approximately 40 mA. Once they reach this energy, the protons are injected into the main ring which accelerates them to 150 GeV/c. At this stage, the protons are injected into the Tevatron, which is an accelerator ring located just above the main ring and of the same circumference. The difference is that the Tevatron uses superconducting magnets to bend the protons around the ring. The higher magnetic field strengths of these magnets allow the protons to be accelerated up to 800 GeV/c.

[1]The beam flows from upstream to downstream. These terms are often used to describe the position of one device in the spectrometer relative to another.

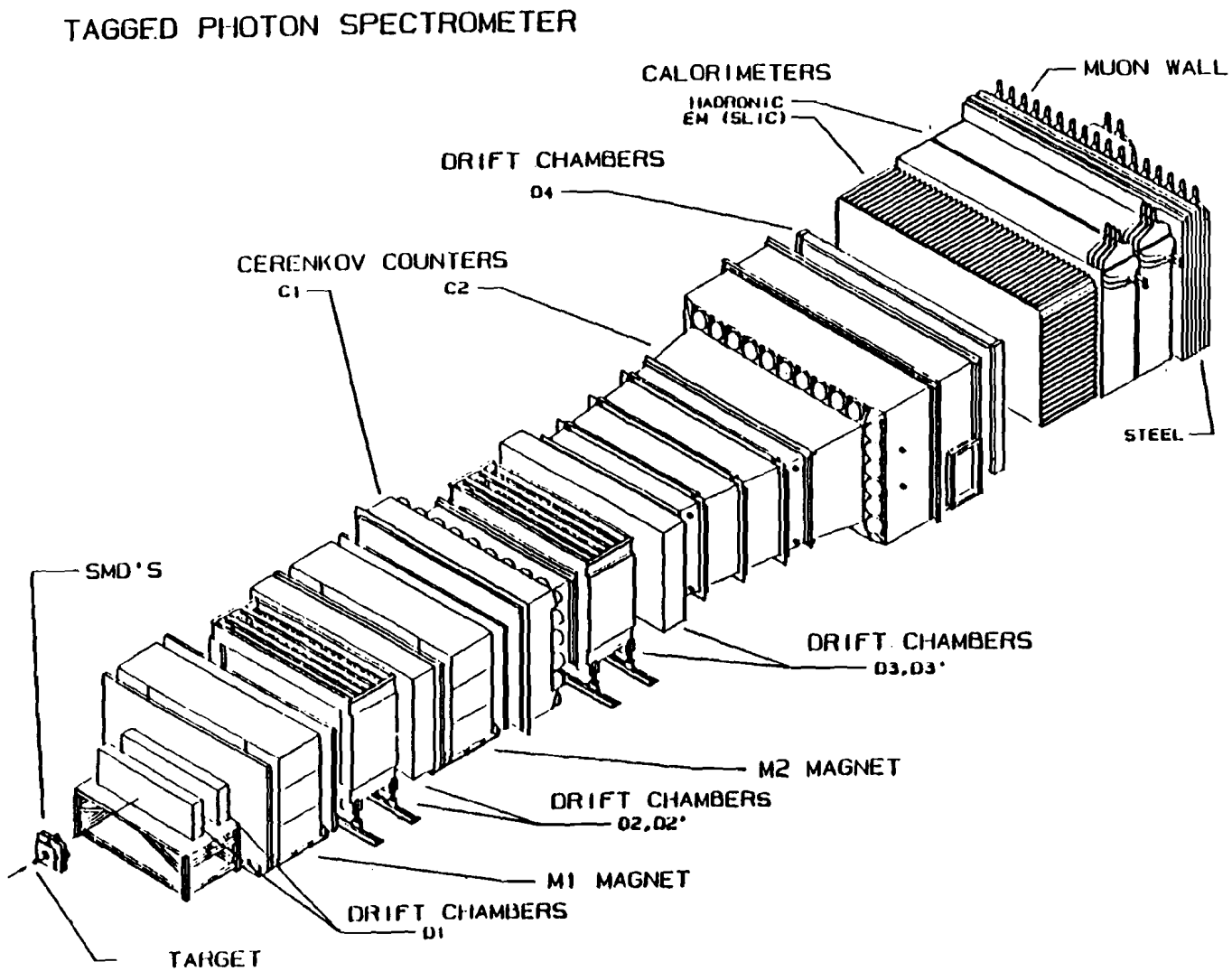

Figure 2.1: Perspective view of the E769 Spectrometer.

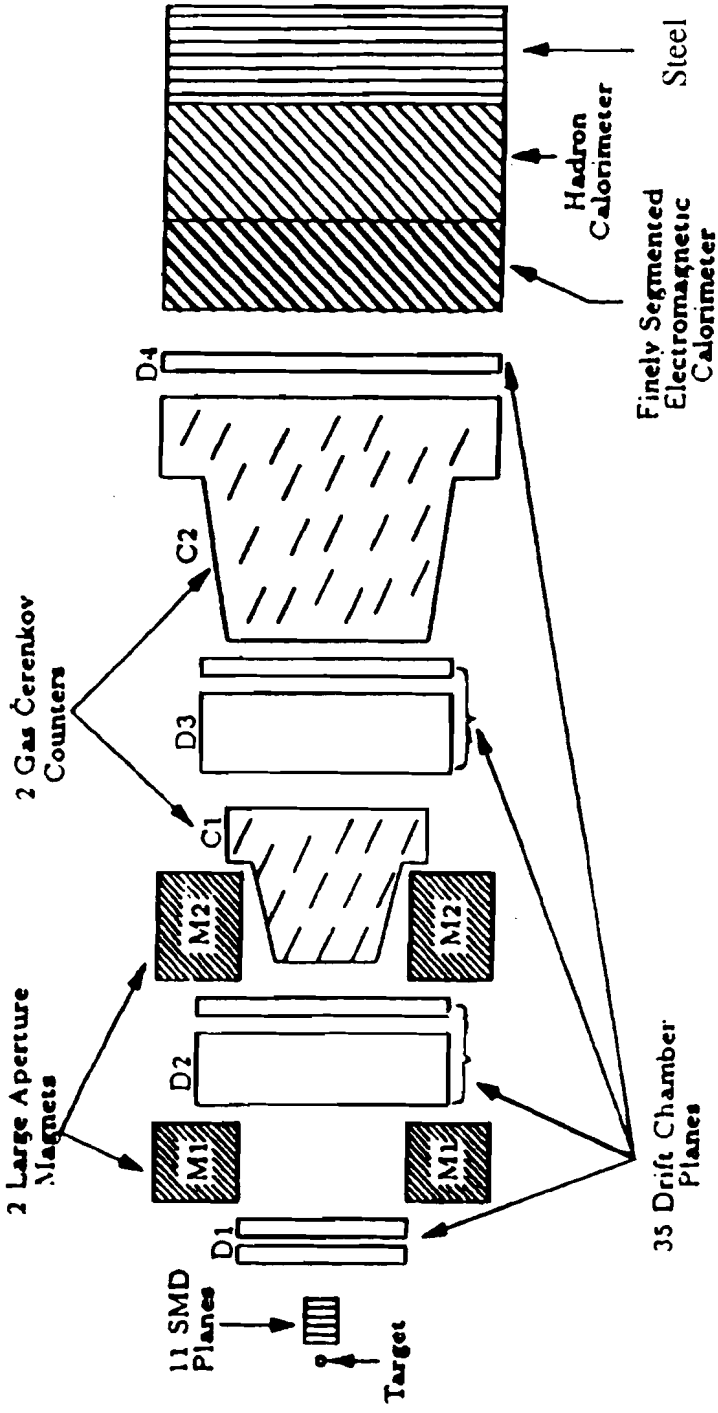

Figure 2.2: Cross Section view of the E769 Spectrometer (not to scale).

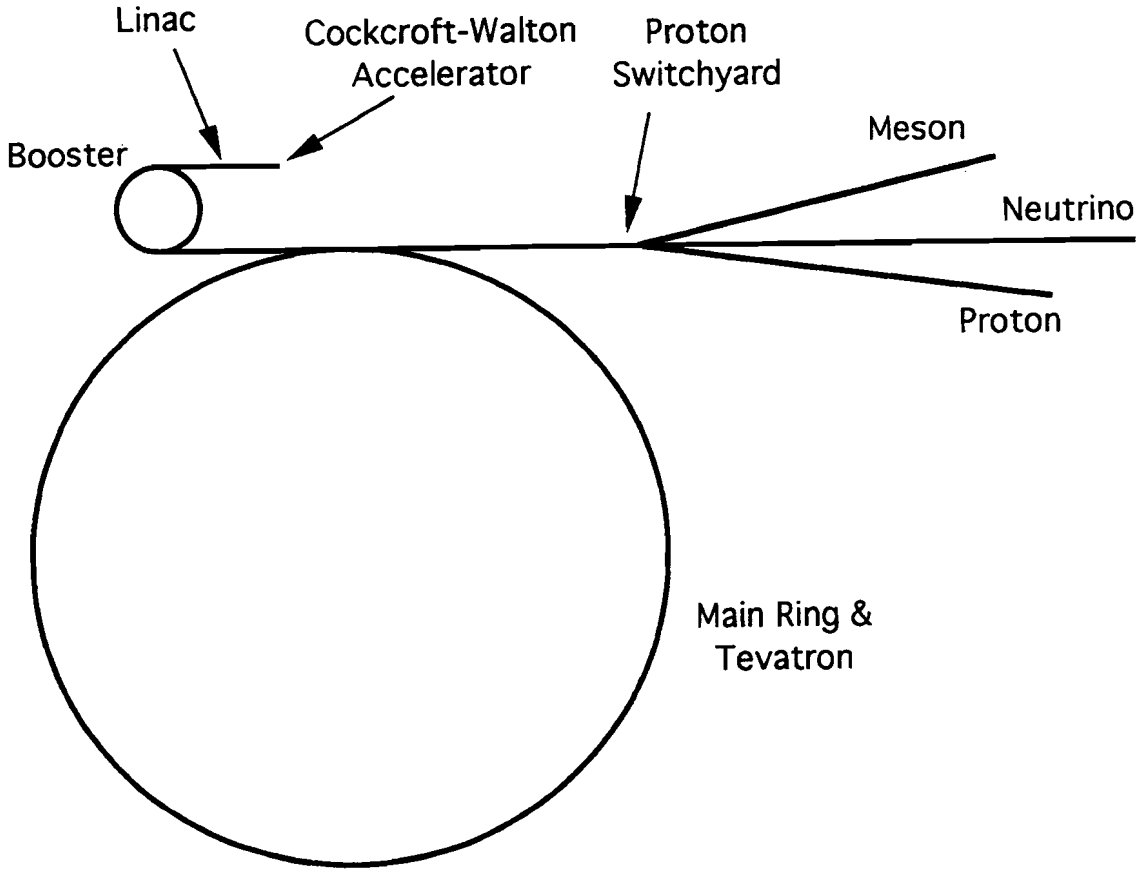

Figure 2.3: The Fermilab proton accelerator and distribution system.

The protons are extracted in spills of 22 s every minute and sent to a "switchyard" which splits the beam to each of the fixed-target experimental sites.

The TPL primary proton beam, which has a flux of approximately 10^{12} protons/spill, interacts with a 30 cm Be target. A dipole magnet downstream of this target selects out a 250 GeV/c charged secondary hadron beam composed of π, K and p which is transported to the experimental area. The magnet's current can be reversed so that the charge of the particles can be selected. For the first half of the run, the magnet transported negatively charged beam. The second half of the run was dedicated to positively charged beam. The result is a typical secondary hadron beam rate $\sim$1 MHz. Table 2.1[19] shows the beam composition, determined by a study using the beam particle identification detectors described below.

Table 2.1: E769 Beam Composition.

Particle Type	Negative Beam	Positive Beam
π	$93 \pm 1\%$	$61 \pm 3\%$
K	$5.2 \pm 0.7\%$	$4.4 \pm 0.2\%$
p	$1.5 \pm 1\%$	$34 \pm 3\%$

2.2 Beam Particle Identification

2.2.1 DISC

The Differential Isochronous Self-collimating Čerenkov (DISC) [20, 19] is one of two detectors used to determine the beam particle identity (called beam-tagging). A particle emits Čerenkov light when its speed exceeds the phase velocity of light in the medium. By measuring the angle of emission of the Čerenkov light with respect to the particle's direction, its speed is determined by

$$\cos\theta_c = \frac{1}{\beta n} \tag{2.1}$$

where θ_c is the Čerenkov angle, β is the speed of the particle in units of the speed of light and n is the index of refraction of the medium. Since all of the beam particle types have the same momentum, knowing the speed is equivalent to knowing the identity.

The DISC was designed and built at CERN and was installed at TPL for experiment E769. It is five meters long and half a meter in diameter. The beam traverses the DISC along its cylindrical axis, passing through approximately 8 atmospheres of He gas. The Čerenkov light is reflected by a mirror (see Fig. 2.4) at the exit aperture of the DISC which images the ring of light onto a diaphragm located at the focal point of the mirror. The mirror has a hole of radius 2.5 cm in its center to allow the particle to exit the detector. A circular slit is cut in the diaphragm at a radius of 10.75 cm and an array of eight phototubes looks for Čerenkov light imaged on the slit. From this geometry, one notes that the detectable angle of Čerenkov radiation is fixed. The DISC detects different particle types by adjusting the pressure of the

He gas, thus changing the index of refraction. A value of n is chosen so as to satisfy equation 2.1 for fixed values of θ_c and β. The phototubes are assigned to pairs and analyzed in quadrants. If at least one phototube in each quadrant sees light, a particle of the appropriate type is assumed to have passed through. Also seen in the figure are chromatic and coma correctors. The chromatic corrector is a triple lens system of two SiO_2 lenses with a NaCl lens in between, which compensates for the fact that the He index of refraction is wavelength dependent. The coma corrector is a SiO_2 lens which corrects for aberrations introduced by the mirror.

The He pressure is selected by performing a test to see where the DISC is most efficient for detecting the particle of interest. A pressure curve is made using an online program which can vary the He pressure between beam spills and then record the number of phototubes that fire for each beam particle. Fig. 2.5 shows the number of times six phototubes fired versus the He pressure. The left-most peak is that due to pions, the bump on its right shoulder is the kaon peak, and the rightmost peak is due to protons. Because the kaon and pion peaks overlap, when the DISC was set to detect kaons (which was most of the time) a pressure slightly above the kaon peak was chosen.

2.2.2 TRD

The Transition Radiation Detector (TRD)[21] is the other beam-tagging system. Transition Radiation (TR) is emitted whenever a charged particle passes from one medium to another when the media have different indices of refraction. In order to get appreciable radiation, the following condition must be satisfied[22] (assuming $\gamma \gg 1$):

$$n(\omega)\gamma\theta \lesssim 1 \tag{2.2}$$

where $n(\omega)$ is the frequency dependent index of refraction of the material, θ is the angle the radiated photon makes with respect to the particle's trajectory and γ is the relativistic factor $\frac{1}{\sqrt{1-\beta^2}}$. The photons emitted by this process are what the TRD detects.

Fig. 2.6 shows a diagram of a TRD module. 24 such modules are stacked in the

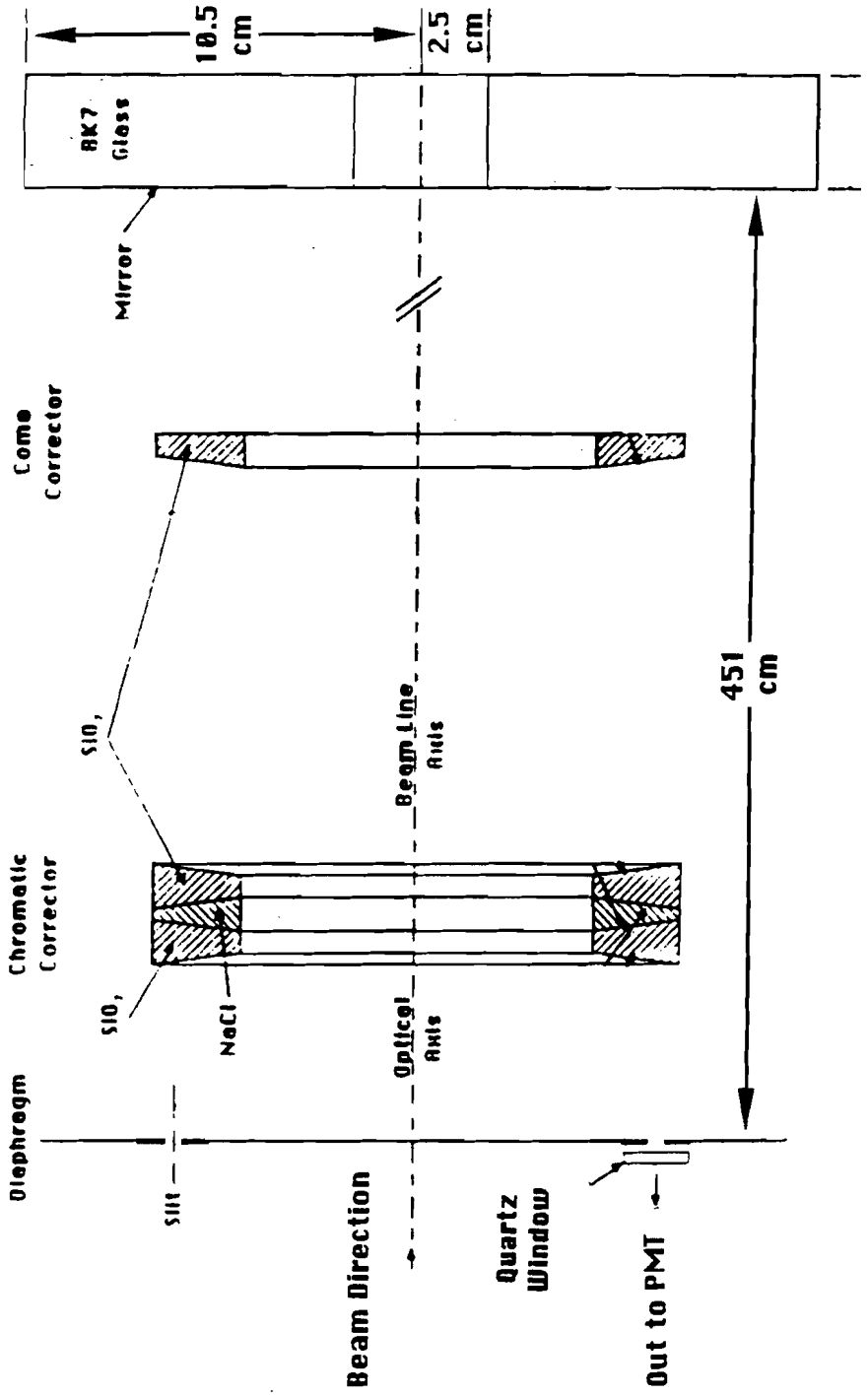

Figure 2.4: Schematic of the DISC optical system.

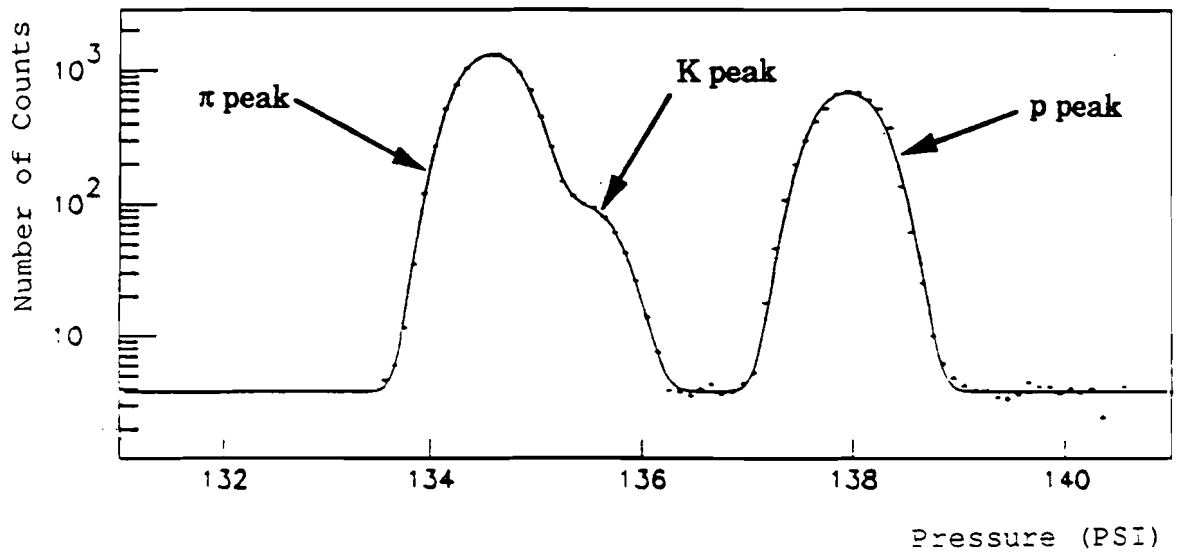

Figure 2.5: DISC counting rate vs. DISC pressure.

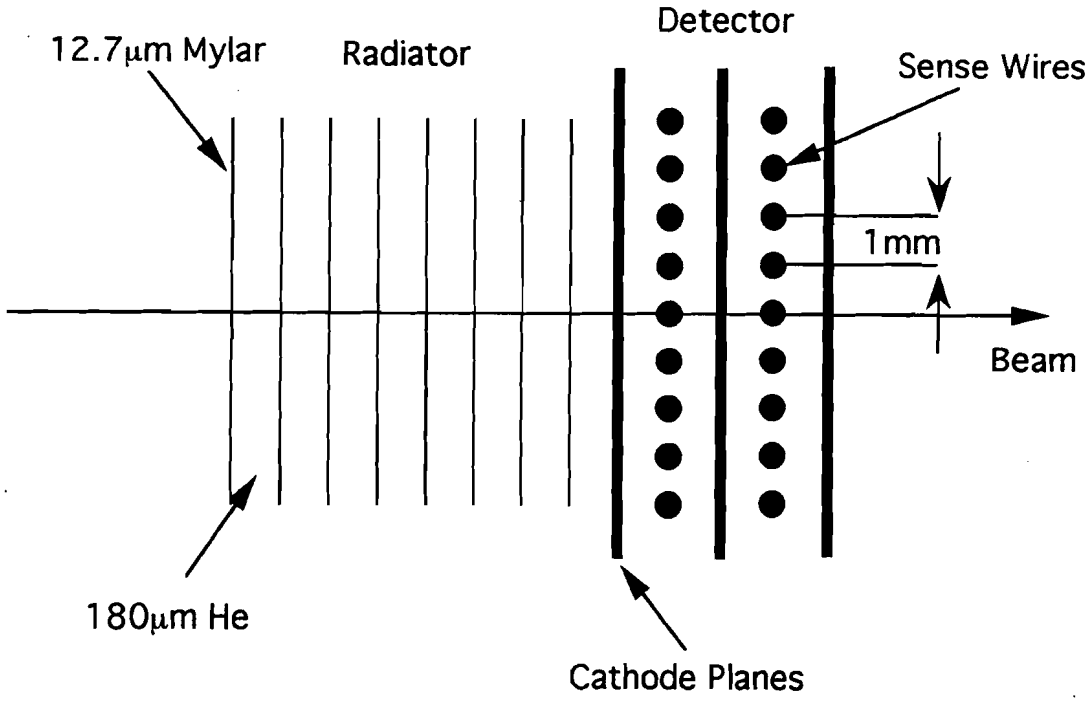

Figure 2.6: Diagram of a TRD module.

beamline each consisting of a radiator volume and a detector volume. The radiator volume consists of 200 12.7μm layers of polypropylene interleaved with sheets of 180μm nylon netting. The netting serves as a gap spacer for the polypropylene and the gaps are flushed with He gas. The detector volume consists of two 64 wire proportional wire counter (PWC) planes with 1 mm wire spacing in a 90% Xe/10% methylal gas mixture. The combined photon detection efficiency of the two planes is 85%.

Because of their higher γ factor, pions emit more transition radiation photons than do kaons or protons; this fact is used to identify pions. The signals from the PWC wires are integrated for 100 ns. Then the signals from four adjacent wires of a plane are added, amplified and discriminated to form a digital signal. If any of these 16 outputs for the plane is in the on state, a TR photon is assumed detected. For a

beam particle to be called a pion, at least 9 of the 48 planes must see photons.

Throughout the run, the TRD is used to distinguish pions from protons. This combined with the DISC pressure set to detect kaons allows the beam particle to be identified. The DISC information is used first. If it sees a kaon, the particle ID is complete. If not, the TRD information is used to determine if the particle is a pion or a proton. Fig. 2.7 shows a contour plot of the number of phototubes fired versus the number of TRD planes fired for a subset of the data. From this plot the separation of the three particle types is clear. The peak for high phototube count is due to kaons. Of the other two, the proton peak is the one with the low TRD plane count. The background to the pion signal caused by protons is due to δ-rays (energetic electrons produced by collisions of a particle with a medium) being mistaken for TR photons, because the γ of the proton is so much lower than that of the pion that its TR is negligible. The efficiency for detecting δ-rays is $\sim$10%/plane, so a lower cut on the number of TRD planes that see photons is sufficient to remove most of the contamination. The beam particle identification will be discussed further in Sec. 5.3.1.

2.3 Beam Tracking

A set of proportional wire chambers (PWC) and silicon microstrip detectors (SMD) are located between the beam tagging system and the target. These are used to reconstruct the trajectory of the beam particle. With this information, two advantages are gained. First, one has the ability to project the track into the target to help identify the production vertex. Second, one can identify events with more than one beam particle in them.

The reader is referred to Section 2.5.1 for a description of the SMD planes used for beam tracking and the principle of operation of an SMD. A PWC consists of a set of parallel, equally spaced wires between two cathode planes used for position measurement of charged particles traversing the chamber. The volume between the cathodes is filled with a gas with which the charged particle interacts. Most of the energy given up to the medium is in the form of excitation and ionization of the atoms.

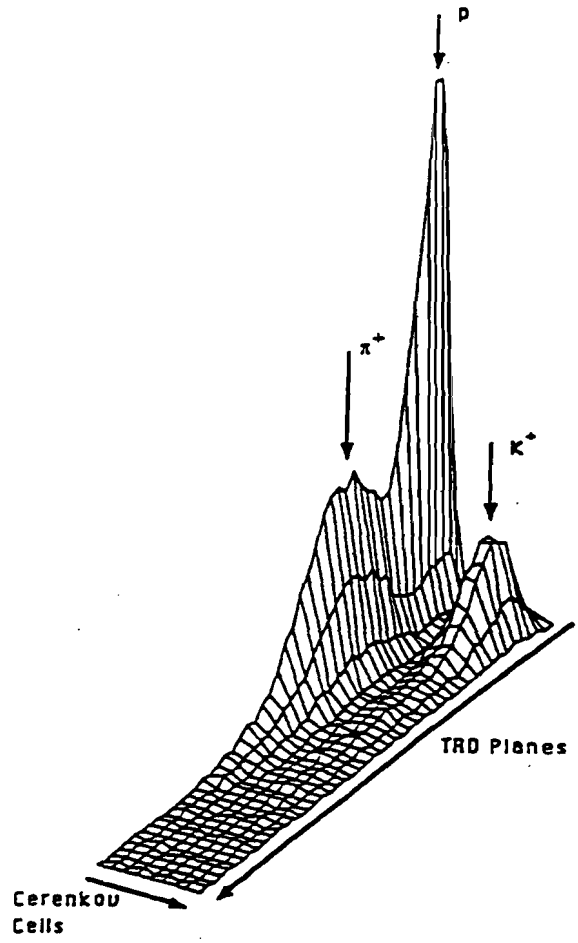

Figure 2.7: Distribution of TRD plane count vs. DISC phototube count.

The ionization is amplified by avalanching due to the presence of a high electric field near the anode sense wires. The charge is then collected at the sense wires for a spatial measurement.

For E769, the beam tracking PWC system consists of two clusters of four planes each. Within a cluster, there planes are arranged in x, x', y and w views. An x' view is offset from an x view by one-half of the sense wire spacing. A w view is an x rotated by $-60°$. Each plane consists of 64 sense wires with 1 mm wire spacing. The active volume of the chambers are filled with a gas mixture of 17% CO_2/.3% Freon/82.7% Ar.

2.4 Target

The E769 target consists of thin foils of Be, Al, Cu and W stacked longitudinally in the beam as illustrated in Fig. 2.8. The foils are separated by 1.6 mm gaps along the beam direction so that the foil responsible for the interaction can be determined from the vertex information derived from the SMD system. This configuration was chosen because it provides a convenient way to study the A-dependence of the charm cross section. The high Z targets are located upstream, to minimize multiple scattering effects of secondary tracks. Table 2.2 summarizes the target characteristics. The thickness of each foil was measured at five different points with a micrometer. An average for each foil is calculated and these averages are combined to obtain an overall average for each material type. The scintillator entry in the table represents the interaction counter (see Sec. 2.12), which is an allowed target.

2.5 Downstream SMD

Fixed target charm experiments were revolutionized with the addition of SMDs. With them single track resolutions similar to the best values from bubble chambers are obtained. In addition, the need to inspect a series of photographs or plates for interesting physics (as in the case of bubble chamber and emulsion experiments) is avoided. The SMD events are analyzed via computer algorithm making it possible

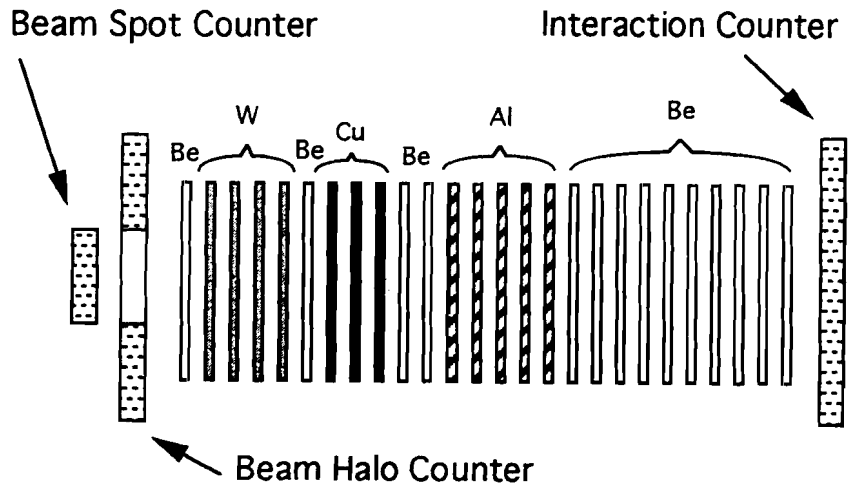

Figure 2.8: Schematic of the E769 target.

Table 2.2: E769 Target Information.

Material	Number of foils	Average thickness per foil (μm)	$\lambda_{Int}(\%)$	$\lambda_{Rad}(\%)$
Be	14	259.5	0.893	.0103
Al	5	252.7	0.320	.014
Cu	3	253.8	0.506	.0533
W	4	95.3	0.397	.11
Scintillator	1	3175	0.400	.0075
Total	26	–	2.516	.20

to reconstruct far more events in the same amount of time.

To collect a large sample of charm decays requires, among other things, the ability to record a large set of data over a reasonable period of time. This demonstrates the other advantage of the SMD because, depending on the amount of money spent on the system, a system can be constructed with essentially no dead time[2]. Bubble chambers on the other hand require cycle times on the order of 100 ms before they can accept another event. The implemented system for reading the silicon information for E769 is discussed below.

2.5.1 Principle of Silicon Particle Detectors

A silicon microstrip detector starts out as a wafer of pure silicon. In the case of the E769 planes, the dimensions are typically 5 cm $\times$ 5 cm $\times$ 300 μm. The bottom of each plane (called a backplane) is doped with a uniform n-type layer of arsenic which is then covered with a thin layer of aluminum (see Fig. 2.9). The other side of the silicon wafer is implanted in strips with boron, forming p-type layers. These strips are also covered with a thin layer of aluminum. The p-i-n structure from strip to backplane is reverse biased with a DC voltage, depleting the region. Position measurements are made by detecting the ionization due to the coulomb interaction of charged particles traversing the silicon. For a minimum ionizing particle passing through a 300 μm thick silicon plane, approximately 25,000 electron-hole pairs are produced. This charge is collected by the strips, which are connected to external electronics for amplification, discrimination and storage.

2.5.2 Specific SMD Information for E769

The E769 SMD system (see Fig. 2.10) consists of 13 planes constructed in two phases. The nine most downstream planes were installed for experiment E691. They are grouped into stations of three planes each, referenced by a number from one to three. The other four planes were installed for E769 and are slightly different. They are grouped into stations of two planes, referenced by letters A and B. The A station (not

[2]Dead time is the time a device needs before it can look at the next event.

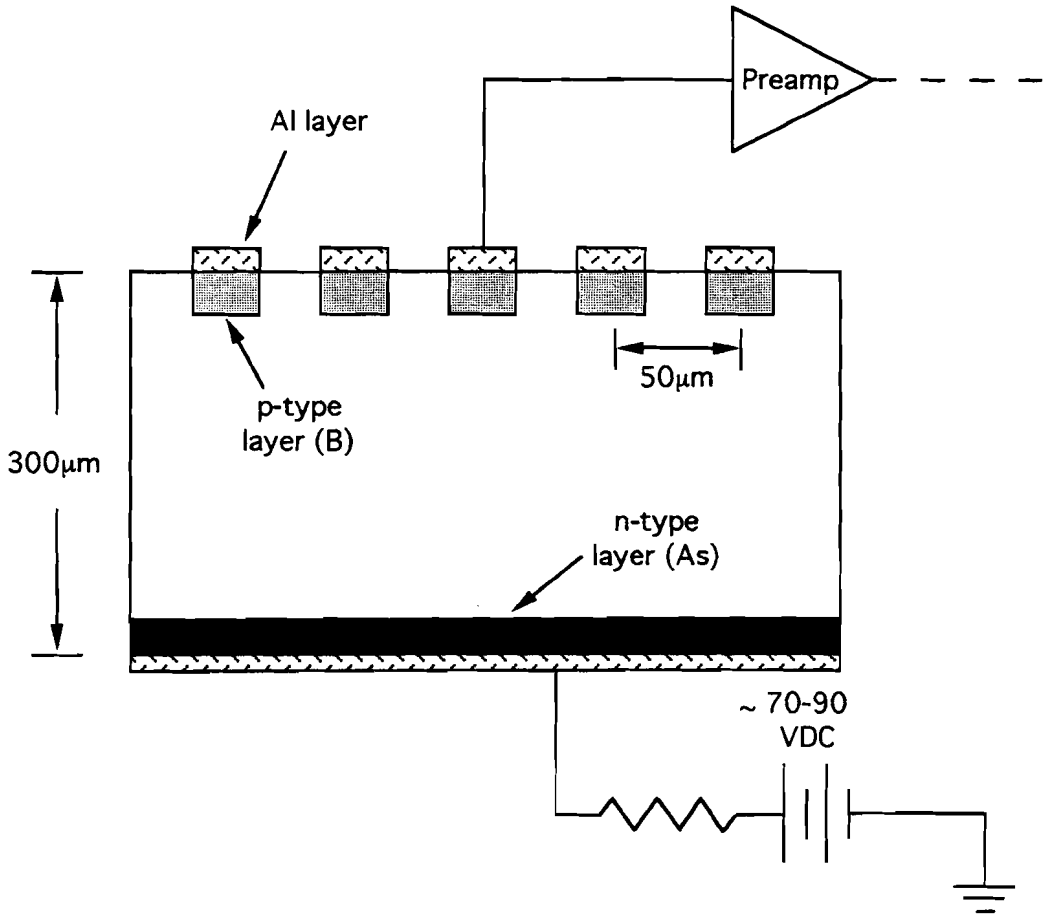

Figure 2.9: Cross section view of a typical SMD plane.

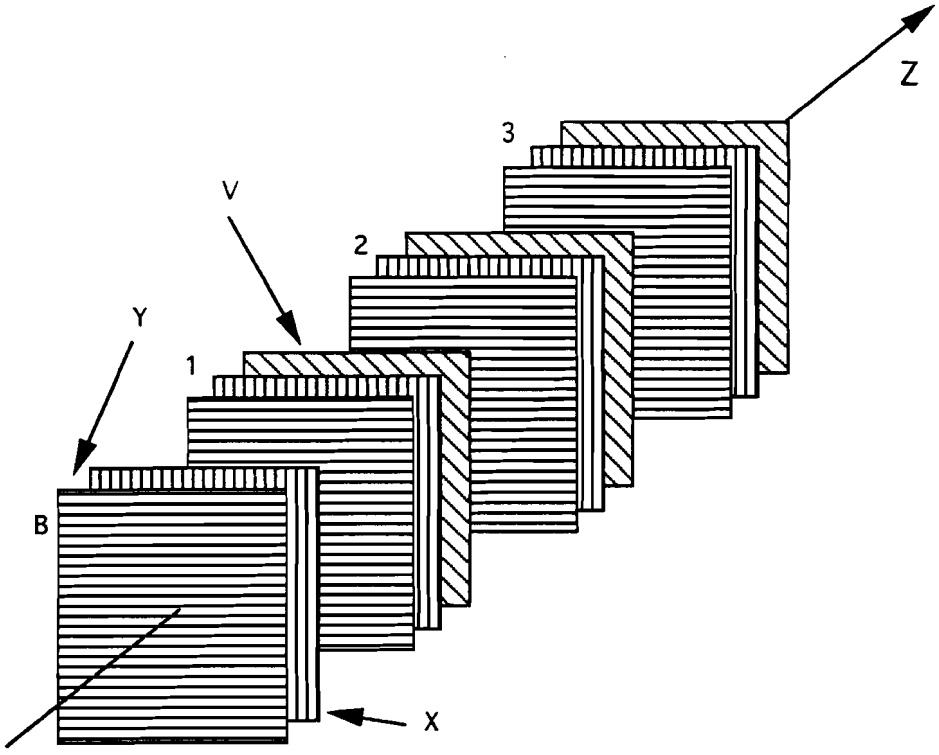

Figure 2.10: Downstream silicon plane positions.

shown in the figure above) is located upstream of the target and is not used in this analysis. Its characteristics are discussed in this section as a matter of convenience. The two silicon subsystems are discussed separately below. The planes which are new for this experiment are subsequently referred to as the E769 planes. Similarly, the planes installed for experiment E691 are referred to as the E691 planes. We make the distinction by history because there are slight differences in their manufacture and readout.

Both Table 2.3 and Fig. 2.10 show the z positions of the silicon planes, where the origin of the coordinate system is chosen near the downstream face of the interaction counter. The silicon plane positions are chosen under two constraints. First, we require well measured track slopes and intercepts. This favors planes widely spaced.

Second, we require a large angular acceptance[3] which favors planes positioned close to the target. The errors on the track slopes and intercepts determine the vertex resolution, so minimizing them is very important. The E769 downstream SMD system is completely contained within 25 cm of the interaction counter. Such an arrangement yields an angular acceptance of ± 100 mr which is approximately the acceptance of the drift chamber and calorimeter systems.

E691 Silicon Planes and Readout Electronics

All E691 planes are of 50 μm pitch and are depleted with a bias voltage of 90 VDC. Each plane within a station is oriented in a different view: x, y, and v (an x-view rotated by 20.5°). Table 2.3 summarizes their characteristics.

The signals from the silicon strips are read out by two-stage amplification. The first stage, known as the pre-amplifier stage, is performed on a hybrid card, constructed from both surface-mounted components and thick-film resistors. The four-channel cards are contained in silver plated aluminum boxes (called "card cages") in groups of 32. The card cages serve both as protection and rf shielding. They are ohmically mounted directly to the housing of the silicon planes, which are also rf shields. The pre-amplifier cards were manufactured and tested by Laben and each channel has a current gain [23] of $\sim$200 and a rise time $\sim$3 ns. Typical pre-amplifier output for a minimum-ionizing particle is 1 mV.

The single-ended output is sent via shielded flat cable to a "readout card" of eight channels (two preamp cards per readout card). This is where the second stage amplification and discrimination is performed. The input signal is amplified and compared to a reference. If the input is above threshold, this channel registers a hit. The other task of the card is to send the collected information out to the digitizing system by the use of a shift register. This is a device that is driven by an external clock and sends its digital information synchronized with the clocking signal. For further information on the preamplifier and readout cards see references [24, 25].

[3]The acceptance is the fraction of the charged particles produced in an interaction that pass through the active detector area.

E769 Silicon Planes and Readout Electronics

The E769 silicon planes are constructed with 25 μm pitch strips in their center and 50 μm pitch strips in their wings. The planes are depleted with a bias voltage of 70 VDC. Table 2.3 summarizes their characteristics with two entries for the pitch and number of strips in the planes of the A and B stations. The first is for the 25 μm strips and the second is for the 50 μm strips. There are 151 50 μm strips instrumented on each side of the central region for the B station planes.

As with the E691 planes, the silicon strips are read out via two-stage amplification using a hybrid card pre-amplifier. Each card contains four channels and 32 of them are mounted per card cage. The card cages mount directly to the silicon plane rf shield. These pre-amplifier cards differ from the others in that the output is differential, meaning that each channel has two signal outputs, one inverted with respect to the other. The pre-amplifier cards were manufactured and tested by Laben and each channel has[26, 27] a current gain of $\sim$1000 and a rise time of $\sim$5 ns. Typical pre-amplifier output for a minimum ionizing particle is $\sim$1 mV.

The differential output of the preamplifier is sent via twisted ribbon cable to the readout card. This eight channel readout card is identical to the above except that it has a modified front end to accommodate the differential input. The front end modification takes the difference of the inputs thus doubling the signal and subtracting any common mode noise such as rf pickup.

2.5.3 Read Out Electronics and Architecture

Electronics for reading out silicon strips can be organized in any fashion suiting the designer. For vertex measurements, the strips are typically amplified and discriminated so that each strip output has only two states, on or off. These outputs are then sent to an address digitizer which sends them to a storage device such as magnetic tape. There are three schemes for extracting the data to the digitizer: parallel, serial or a combination of the two. In a parallel design, every strip has its result sent to the digitizing system by a separate line of electronics. In this way, besides overhead, the full system is read out in the time it takes to read out one channel of data. In

Table 2.3: SMD Plane Specifications.

Station	View	Pitch (μm)	Active Area (mm^2)	Number of strips instrumented	Nominal z Position (cm)
A	y	25/50	9.65×28.75	386/0	-17.3
	x	25/50	9.65×28.75	386/0	-17.0
B	y	25/50	24.75×28.75	386/302	0.2
	x	25/50	24.75×28.75	386/302	0.6
1	x	50	25.6×25.6	512	1.9
	y	50	25.6×25.6	512	2.9
	v	50	25.6×25.6	512	6.7
2	y	50	38.4×50.0	768	11.0
	x	50	38.4×50.0	768	11.3
	v	50	38.4×50.0	768	14.9
3	x	50	50.0×50.0	1000	19.9
	y	50	50.0×50.0	1000	20.2
	v	50	50.0×50.0	1000	23.8

the serial scheme all output signals are sent to the digitizing system via one line of communication and the data stream is sometimes referred to as a chain of data. The full time to read out this system (ignoring overhead) is the total number of channels multiplied by the time it takes to read out one channel. In the hybrid scheme, the full system is split up into a set of serial communication lines. Its readout time is the number of channels read out in the largest chain of data times the time it takes to read out one channel.

With the parallel system one achieves the fastest possible readout time, i.e., the lowest dead time. However except for the case of a few strips of silicon, the cost of implementing a completely parallel design is prohibitively expensive. The lowest cost per channel is attained by using the serial design. The problem with it, however, is that it is by definition the slowest scheme. It is for these reasons that a hybrid scheme was chosen for E769. The implemented system contains eight chains of data, where a chain contains the output of anywhere from a few hundred to 1500 strips. Each chain is read out at a rate of 5 MHz, so the full system is read out in 300 μs. Further information may be obtained from reference [25].

2.6 Downstream PWC

The PWC principle of operation was described in Section 2.3. E769 has two PWC planes downstream of the target, each consisting of 288 wires with 2 mm spacing. The active volume is filled with a gas mixture of 17% CO_2/.3% Freon/82.7% Ar. The planes are located downstream of the silicon planes with one upstream of the D1 drift chamber station (see below) and the other between the two D1 chambers. Their purpose is to provide position measurements in the y-view to aid the silicon tracking, because there are no y planes in D1.

2.7 Drift Chamber

A drift chamber (DC) is a PWC with field shaping wires added between the sense wires to make the electric field throughout the medium approximately uniform. With this setup, the drift time of ionization caused by the traversing charged track is linearly proportional to the distance the charge travels to the sense wire. By counting the time delay between a reference time and the signal arrival, the position of the track is determined.

The E769 DC system consists of 35 planes, grouped into four stations (D1, D2, D3 and D4). The first three stations make position measurements just before tracks enter a spectrometer magnet and just after they exit it. D4 is located close to the calorimeters which helps when calorimeter energy clusters are matched with tracks. In addition, this separation from D3 provides a lever arm for measuring the track slopes and intercepts.

Drift chamber position measurements have two uses. They complement the tracking information from the silicon in cases where the number of silicon hits for a given track is low. They are also used to make the momentum assignments to the tracks because this information allows one to trace the track through the analyzing magnets.

Each station is divided into assemblies, which describe the orientation of the sense wires. D1 is composed of assemblies in the u, v, x and x' views. An x' view is the

same as an x view, except that it is offset by half a cell width[4], in order to resolve ambiguities. The u and v views are tilted by $\pm 20.5°$ with respect to vertical (the direction of the x-measuring sense wires). The other three stations have assemblies in the u, v and x views. All of the chambers have a gas mixture of 50% ethane/50% Ar with ~1% ethanol. The ethanol prevents quenching and acts as a age-prevention agent. See Table 2.4 for a summary of the drift chamber system characteristics. Further information may be obtained from [19].

Table 2.4: Drift Chamber Characteristics.

	D1	D2	D3	D4
Nominal Active Area($x \times y$, cm^2)	90×90	190×170	250×220	510×360
Cell Size(x, cm)	.45	.95	1.59	3.18
(u/v, cm)	.48	.89	1.49	2.97
Nominal z position(cm)	174	442	988	1744
Num. of Assemblies	2	4	4	1
Views	$xx'uv$	xuv	xuv	xuv
Num. of Planes	8	12	12	3
Nominal Efficiency(%)	91	85	88	69
Nominal Resolution(mm)	.41	.35	.32	1.20

Because of the high beam rate, the drift chambers have a reduced track detection efficiency in the central region (called a hole). The size of the hole is rate dependent and is separately parameterized from data for positive and negative beam polarities. This parameterization is used in the MC simulation of the DC tracking.

2.8 Analyzing Magnets

E769 uses two analyzing magnets that bend charged tracks in the xz plane, which runs parallel to the ground. The most upstream magnet (M1) is run at 2500 Amperes, giving a p_T kick of ~.21 GeV/c. M2 is run at 1800 Amperes, giving a p_T kick of ~.32 GeV/c.

[4]A cell for a given sense wire is the gas volume between its two nearest field shaping wires.

The field strengths and shapes were measured for E516 by dividing the field region into a three-dimensional grid and making measurements of the field at points on the grid with a Hall probe. This information is used during reconstruction of data to determine track momenta in conjunction with the DC position measurements. It is also used in the MC simulations to swim the charged tracks through the spectrometer.

2.9 Threshold Čerenkov

Two Čerenkov counters provide $\pi/K/p$ separation of charged secondaries. They are threshold counters in that gas mixtures used in the Čerenkov volume are chosen to provide discrimination of these hadrons in the momentum range expected. The most upstream Čerenkov counter (C1) contains pure N_2, while C2 contains 80% He/20% N_2. Both operate at atmospheric pressure. Further information can be obtained from references [28, 19]. The Čerenkov counters are not used in this analysis because they cannot provide π/e separation for momenta greater than 6 GeV/c. According to our Monte Carlo simulation (see Chapter 4), only 5% of the electrons from beauty are found below 6 GeV/c. Because this fraction is so small, the Čerenkov information is not used in the identification of electrons.

2.10 Calorimeters

A calorimeter is a device which measures the total energy deposited by a particle. The type of calorimeter referred to here is called a sampling calorimeter, because the shower medium is alternated longitudinally with a detection medium to periodically measure the energy so that the shape and depth of the shower can be determined. There are two main types of sampling calorimeters, depending on whether the incident particle initiates an electromagnetic or hadronic shower. Material for a particular type is chosen to optimize the detection of a given type of shower. These are the only detectors in the spectrometer that detect long-lived neutral particles (in addition to charged particles). The TPL spectrometer has both types of sampling calorimeter. They are discussed in the following two sections.

2.10.1 Electromagnetic Calorimeter

An electromagnetic(EM) calorimeter detects particles by the EM interaction with a heavy Z material. It is used for detecting and absorbing the energy of photons and electrons (and positrons) via pair production and bremsstrahlung. A fraction of the charged particles emitted by the shower process are seen in the detection media and the signal detected is proportional to the energy of the incident particle.

The Segmented Liquid Ionization Calorimeter (SLIC) [29, 30, 16] is the EM calorimeter used in E769. Together with the Hadronic Calorimeter (see Section 2.10.2) energy clusters are defined and assignments are made to charged tracks when appropriate. The calorimeter information is also used for electron and photon identification.

The SLIC (see Fig. 2.11), 4.8 m high by 2.4 m wide, consists of 60 sheets of 0.17 cm thick lead, which cause the electromagnetic showers, alternated with 60 1.3 cm thick layers of liquid scintillator. To prevent the lead sheets from poisoning the liquid scintillator, they are clad with aluminum. Each layer of scintillator is segmented (see Fig. 2.12 into 3.175 cm wide channels created by corrugated aluminum. All of the aluminum is coated with teflon in order to internally reflect the scintillator light down the channel to the collection end. The index of refraction of teflon is less than that of the scintillator fluid, so much of the scintillating light undergoes total internal reflection. One end of the channel is capped with a highly reflective mirror. At the other end, the light is sent through a wave shifter bar. In this bar, the scintillator light is absorbed and re-emitted at a different frequency that can be detected by a photomultiplier tube (PMT). Each PMT signal is sent to a gated ADC which integrates for approximately 160 ns after the interaction occurs.

There are three orientations of SLIC channels: the u, v and y views, where u and v are $\pm 20.5°$ to vertical. Twenty alternating layers of each view make up the SLIC. Because the outer part of the SLIC has a relatively low occupation, the signals from these segments (within a view) are combined in pairs, effectively doubling the channel width. The central channels are read out singly. Table 2.5 summarizes the SLIC characteristics. The fractional energy resolution of the SLIC is $12\%/\sqrt{E}$ [30], where E is measured in GeV, for isolated showers.

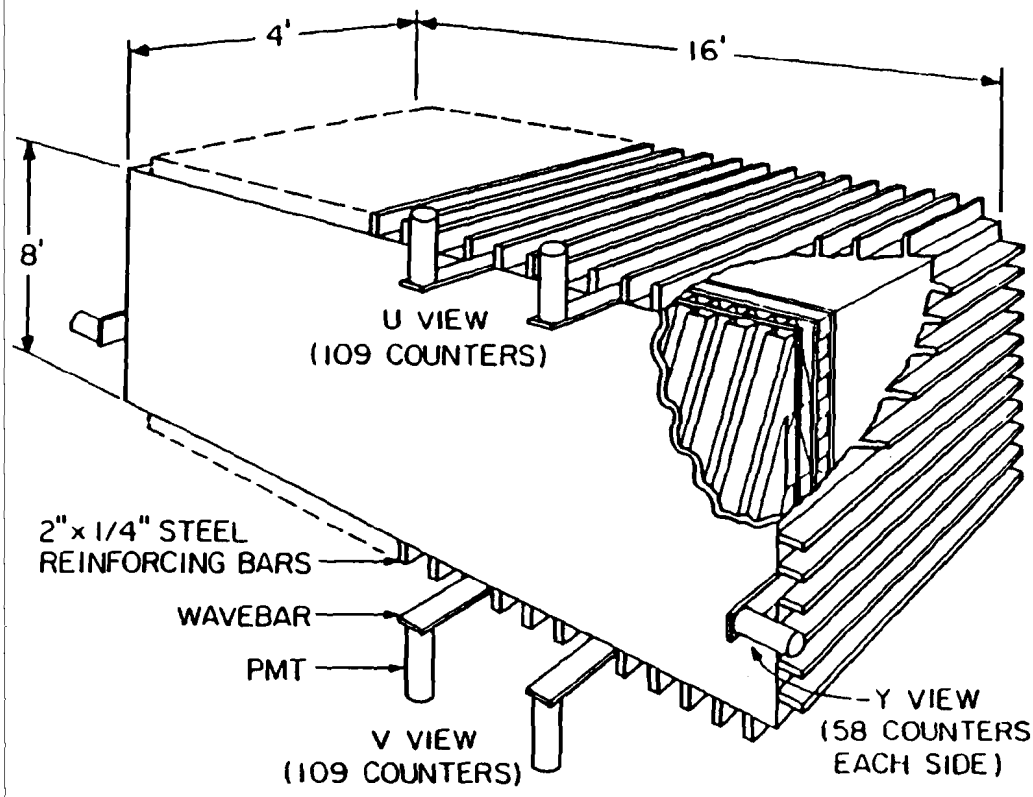

Figure 2.11: Perspective view of the SLIC.

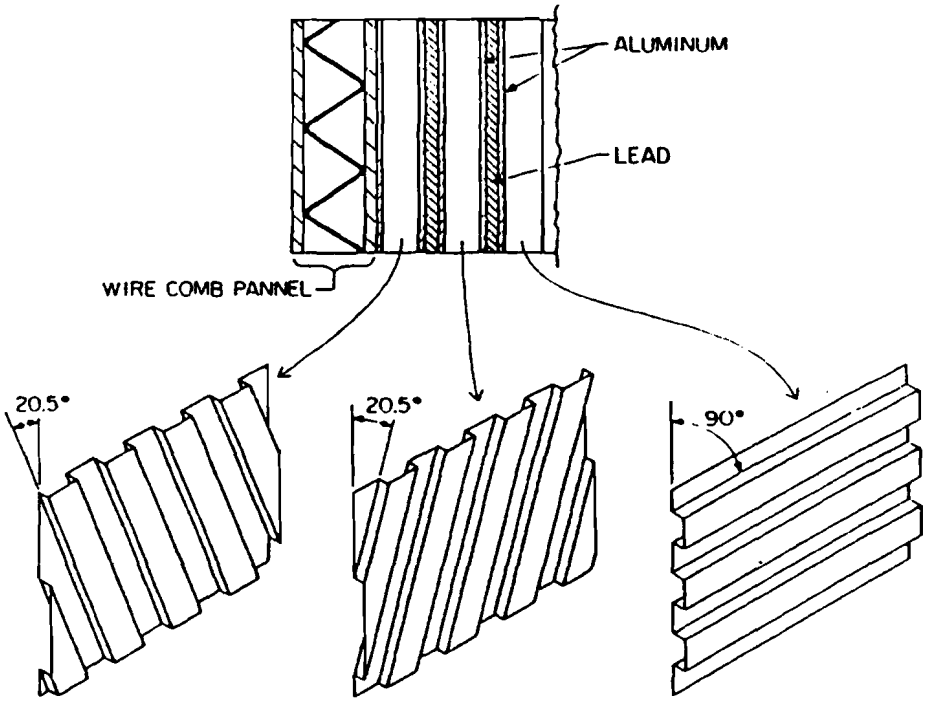

Figure 2.12: Cross section of SLIC scintillator and radiator layer.

Table 2.5: SLIC Characteristics. All distances are in cm.

Nominal z Position	1900
Number of Layers	60
Number of Single Width Channels Per View(uvy)	51 52 82
Number of Double Width Channels Per View(uvy)	58 57 34
Pb Layer Thickness	0.163
Al Layer Thickness	0.010
Scintillator Layer Thickness	1.27
Single Channel Width	3.175
Total Number Radiation Lengths	21.5
Total Number Interaction Lengths	2.1
Acceptance, vertical	$\sim \pm 66$ mrad
Acceptance, horizontal	$\sim \pm 128$ mrad

2.10.2 Hadronic Calorimeter

A hadronic sampling calorimeter is constructed in a similar way to a EM sampling calorimeter. A typical hadronic shower[31] is characterized by multi-particle production with $\langle p_T \rangle \simeq 0.35$ GeV/c. Hadronic showers tend to be wider than electromagnetic showers, which is a signature used to distinguish between the two. Among the secondary hadrons produced in the calorimeter are π^0s, most of which decay to photons that cause EM showers. The charged secondaries that enter the sampling media are then detected.

Fig. 2.13 shows a diagram of the Hadronic Calorimeter (HAD). It is 4.9 m high by 2.7 m wide and consists of 36 alternating layers of radiator and scintillator. The radiator is a 2.5 cm thick steel plate. The scintillator is a doped acrylic segmented into 33 strips for x views, and 19 strips for y views. The strips are 14.48 cm wide by 0.95 cm thick. The signals from the scintillators are organized by strip number into upstream and downstream groups so that for each (x, y) there are four output signals: upstream and downstream in both views. The scintillator light is detected by PMTs which, like those for the SLIC, are read out by gated ADCs. The HAD

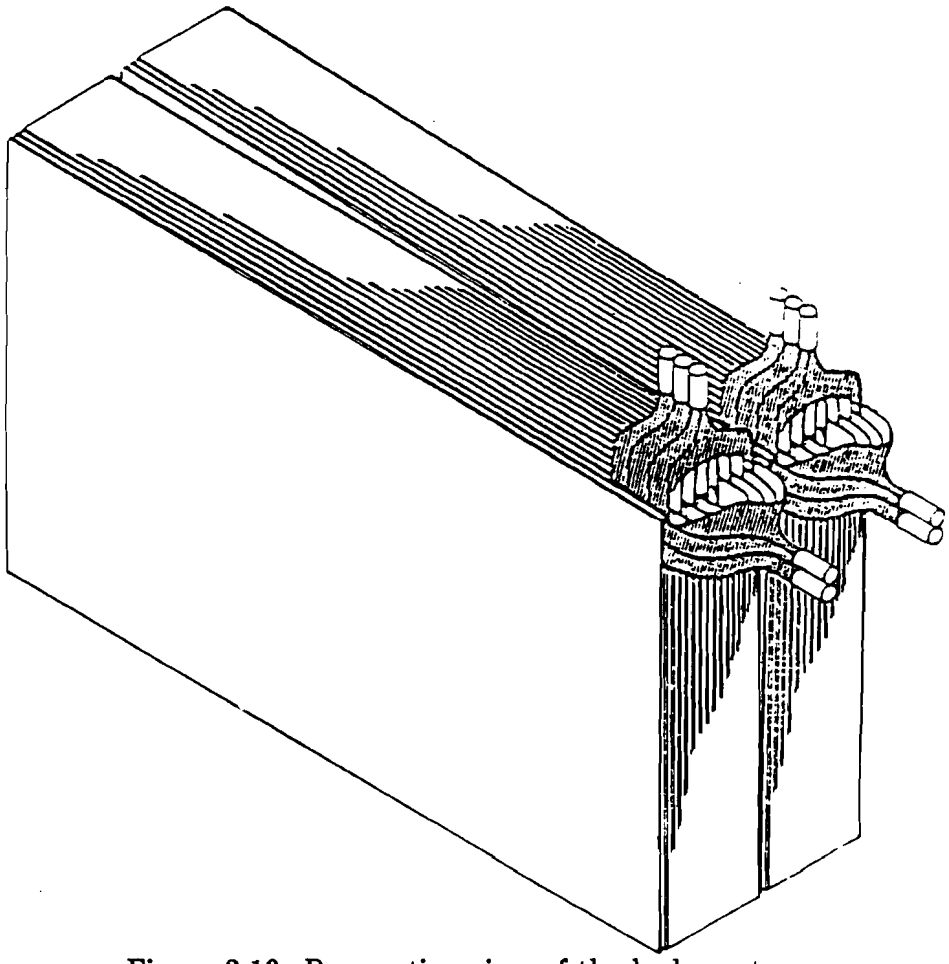

Figure 2.13: Perspective view of the hadrometer.

ADC gate time is approximately 250 ns. The fractional energy resolution of the hadrometer is $75\%/\sqrt{E}$ [34], where E is measured in GeV, for isolated showers. The HAD characteristics are shown in Table 2.6 and further information can be obtained from [34, 16].

2.11 Muon Wall

Downstream of the calorimeters, 40 in of steel range out hadrons, leaving mostly muons. Downstream of this absorber, a segmented wall of acrylic scintillators is arranged in the x-view. A y position is determined offline from the arrival time of the signal relative to the trigger as recorded with a TDC. The scintillators are 18 in wide in the central region and 24 in wide in the outer regions.

Table 2.6: HAD Characteristics. All distances are in cm.

Dimensions($x \times y \times z$)	$490 \times 270 \times 158$
Nominal z Position	2041
Number of Layers	18
Number of Channels Per View(xy)	33 19
Steel Layer Thickness	2.54
Scintillator Layer Thickness	0.95
Single Channel Width	14.48
Total Number Radiation Lengths	52.8
Total Number Interaction Lengths	5.9
Acceptance, vertical	$\sim \pm 66$ mrad
Acceptance, horizontal	$\sim \pm 120$ mrad

2.12 Trigger

There are five triggers used in E769 to write events to tape: Interaction, E_T(standard), E_T(kaon), E_T(high) and Electron, where E_T stands for transverse energy. They are discussed individually below. For the discussions that follow, the reader is referred to the diagram (see Fig. 2.14) of the scintillators in the beam and target region implemented in the trigger logic. The most upstream pair of scintillators are known as the TRD-beam because they are located just downstream of the TRD modules. Next are the beam halo counter and the beam spot counter, which are located just upstream of the target. The coincidence of TRD-beam and beam spot in anti-coincidence with the beam halo defines a beam particle, known as 'Good Beam'. The purpose of the beam halo counter is to veto those hadrons that will miss the target or approach it with a large angle of incidence. The interaction counter is the last of the trigger scintillators, and is located immediately downstream of the target. Its purpose is to detect when a beam hadron interacts with the target which is done by putting a threshold cut on the output of the counter requiring a signal equivalent to five or more minimum ionizing particles.

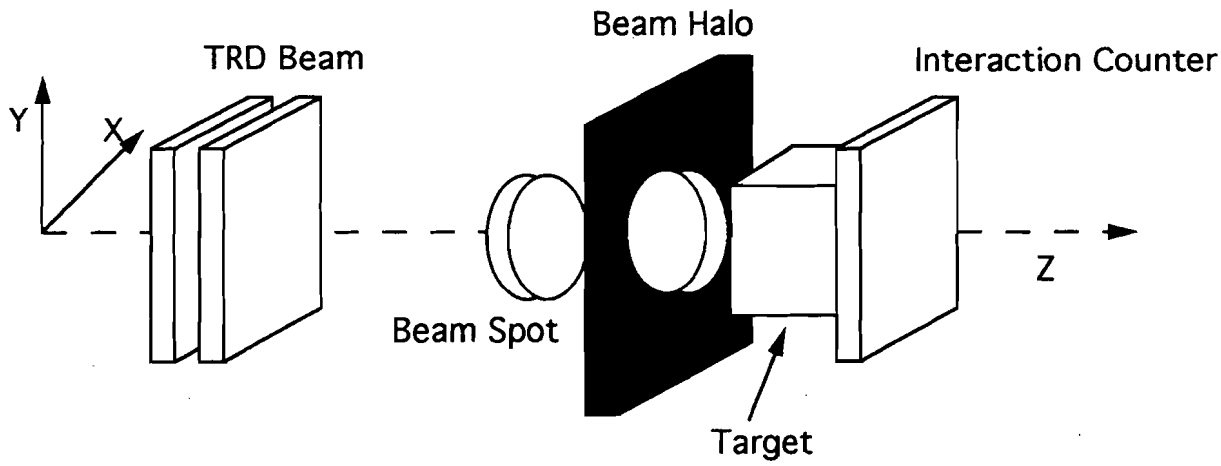

Figure 2.14: Schematic of the trigger scintillators.

2.12.1 Interaction

In a search for events containing a heavy quark, the most obvious requirement is that the beam interact with the target. As the E769 target consists of only ~2% of an interaction length, relatively speaking, this doesn't happen very often. This trigger determines when an interaction occurs, and all of the other triggers use the Interaction trigger as one of their requirements. The trigger is defined to be 'Good Beam' in coincidence with a target interaction. Studies show that approximately 50% of minimum bias events pass this trigger while nearly 100% of the charm events pass this trigger.

Interaction events are recorded for efficiency studies of other triggers. The E769 beam rate is approximately 1 MHz, which means interactions occur at a rate of 20 kHz. Since this raw event rate is much too high for the Data Aquisition (DA) system, interaction triggers that are written to tape are prescaled by factor of about 40. A prescaler is a device that counts the number of input signals it receives; upon receiving the nth input, where n is set by the user, it sends one output signal.

2.12.2 E_T Triggers

All other triggers in E769 are based on total E_T because, on average, heavy quark events have a higher E_T than minimum bias events. The transverse energy for all of the triggers is calculated via an online weighted sum of the signals from the segmented electromagnetic (SLIC) and hadronic (HAD) calorimeters. The weighting is chosen to approximate $E_T = Esin(\theta)$, where θ is measured from the target center to the calorimeter channel center with respect to the beam direction.

One of two thresholds is used for each of the remaining triggers. E_T(standard) and E_T(kaon) use the lower threshold, which requires $E_T \gtrsim 4$ GeV. During positive beam running, imposing the E_T requirement yields an event rejection factor of 1.3 above the interaction trigger requirement. In addition, E_T(kaon) requires that the DISC sees the kaon. Since the kaon beam flux is significantly smaller than the total beam flux, E_T(standard) triggers are prescaled throughout the data run by factors ranging from five to 60 in order to maximize the number of E_T(kaon) events on tape.

The higher threshold is used for the E_T(high) and Electron triggers, which requires $E_T \gtrsim 8$ GeV. The higher event rejection results in a sample enriched with heavy quark events. During positive beam running, imposing this E_T requirement yields an event rejection factor of 5.2 above the interaction trigger requirement. A typical prescale value for E_T(high) is five. In addition to the E_T requirement, the Electron trigger requires a significant energy deposit ($E_T \gtrsim 0.5$ GeV) in a single channel of the SLIC's y view, in a search for high E_T electrons. The Electron trigger enriches the data with heavy quark events because both charm and beauty quarks decay semi-leptonically $\sim$10% of the time while high E_T electrons are rare in minimum bias events. The Electron trigger was installed in the latter part of the run, consequently, only positive beam data is recorded with it. The rejection factor of the Electron trigger is 130, which is the reason these triggers were not prescaled. With a rejection power of 54 above the interaction trigger, the high E_T electron requirement is responsible for most of the event suppression. The overall trigger rejection is less than the product of the individual rejections ($54 \times 7 = 378$) because the two requirements are correlated.

At times during the second half of the run, the beam rate was high enough that more than one beam particle traversed the detector during its live-time. This multiple-beam particle flux causes two problems. First, the TRD distinguishes protons from pions by the number of planes that see photons. The TRD needs approximately 100 ns to integrate the TR photon energies, so if two particles traverse the detector in this time, more planes fire than for one particle which makes the particle ID more difficult. Second, when more than one beam particle interacts, the measured event E_T increases which causes a shift in the calorimeter measurements. This happens because of the 100 ns gate width for the E_T on-line discriminators from which the E_T trigger tests are constructed. This affects the trigger rates and the physics yield per trigger. Even so, the effect is small as is demonstrated in Fig. 2.15 which shows the E_T distribution of positive data events with more than one beam particle per event and without. To prevent recording such events, a signal called the beam-killer was installed for the E_T(standard) and E_T(high) triggers. The beam-killer looks for a second beam particle coming within 150 ns (about seven buckets) before or after the particle causing the interaction and vetoes such events. This was achieved

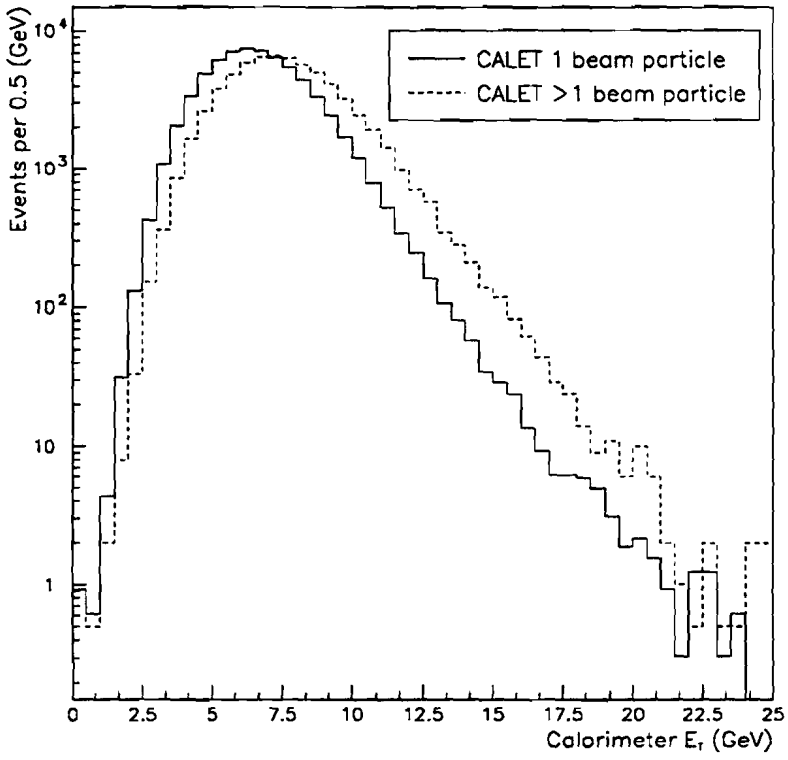

Figure 2.15: E_T distribution of positive data with and without the beam killer.

via a scintillator coincidence in the beam and some time delay modules. The time resolution of the PMTs of these scintillators is on the order of the bucket separation, so it is not possible to veto events with more than one particle in a bucket.

2.13 Data Aquisition

The Data Aquisition (DA) system has three tasks: front end digitizing, event building and event storage. DA performance is measured by its speed of data taking and its dead time. The E769 DA system can process 450 events/s (1.8 Mb/s) with a dead time of 25%. A description of the DA is made below; further information can be obtained from reference [35].

Each subsystem of the spectrometer is read out by a CAMAC (Computer Automated Measurement and Control) based front end digitizing system consisting of seven CAMAC crates. Each crate is read out simultaneously by a readout buffer in a VME (Versa Module Europa) crate; the data transferred is called an event fragment since it consists of the information from one subsystem only. Each buffer has two 32 kb sections of memory and can store two event fragments at once. This allows one event fragment to flow into one set of memory while the previous fragment is being read out of the other.

The event fragments are combined into complete events by a system of VME based event builders working in parallel. The complete events are then written to one of three 6250 bpi (9-track) tape drives. The data aquisition rate during the beam spill is typically 1.5 Mb/s, but the tape drives record data at 0.6 Mb/s. Therefore, the output events are sent to a buffer and the tapes record data both during the spill and interspill. Because of the high data rate, a 6250 tape is filled in approximately five minutes. This is the reason for using three tape drives in sequence, as it gives ample time ($\sim$5-10 minutes) to change a tape.

Chapter 3

Event Reconstruction

After recording data on magnetic tape, the next step is convert the recorded information into information that can be interpreted through physics analysis. This is called data reconstruction and is the subject of this chapter. Reconstruction of the E769 data [33] was primarily performed on two computer systems: the ACP farm and the Silicon Graphics farm. The ACP (Advanced Computer Project) farm is a VME based system of Motorola 68020 processors, designed and constructed by the Fermilab Computing Division. Each ACP node has one processor which performs 0.7 MIPS (millions of instructions per second). The system is composed of 400 such nodes. Of these, 130 were dedicated to the E769 data reconstruction. The Silicon Graphics farm consisted of four model 4D/240S computers manufactured by Silicon Graphics. Each of these has four 15 MHz R3000 processors of 16 MIPS each. With both farms, data reconstruction was completed in approximately one year.

The reconstruction, which is based on the E691 reconstruction algorithm, is performed in stages but are all performed within one job. The stages are PASS0, PASS1, PASS2 and DST. In PASS0, events are read to determine items of interest such as ADC pedestal values for the calorimeters, hot SMD channels and TRD distributions. These are used in the subsequent reconstruction stages. In PASS1, tracks are constructed and track momenta are determined. This begins with tracks being formed from SMD hits. Then these tracks are extrapolated into the DC system for tracking through the magnets. In PASS2, the silicon tracks are combined to make vertices,

the Čerenkov information is assigned to tracks and energy clusters are formed from SLIC and HAD information. In addition, energy clusters are assigned to charged tracks and the electron ID is performed. Most of the CPU time is spent performing the PASS2 analysis. The last stage stores the event in data summary tape (DST) format in which the raw data information (the data recorded by the DA system) is thrown away. This is done to compress the event so that more events can be placed on a tape. Below is a more detailed discussion of the PASS1 and PASS2 stages of reconstruction. More details can be found in [25, 24].

3.1 PASS1

3.1.1 Tracking

Tracking in the region upstream of the analysis magnets is performed first with a prioritorized system using hits from the E691 planes, followed by pattern recognition using PWC and D1 hits. Hits from the E769 planes are not used initially because of their low detection efficiency. For each view, initial track reconstruction is performed by constructing tracks with one hit from each E691 plane. Hits in two of the planes define a road through the third plane. If the third plane has a hit within this road, a two-dimensional (2D) track candidate is formed in that view. Once all 2D track candidates are formed in all three views, matching between views is performed. 2D track candidates from two views are combined to form a 3D track. This candidate is projected onto the third view. A real track is formed if there are 3, 2, or 1 hits in this view consistent with the projection.

Throughout this procedure, as hits are used to form real tracks they are removed from subsequent track reconstruction, i.e., hit sharing is not allowed. Tracks with hit patterns-per-view of 3-2-2, 3-2-1 and 2-2-2 (in this order) are constructed next. In those views with less than three hits, supporting hits are required from PWC and D1 hits. At this point, real tracks are constructed using the hits from the E691 planes[1]. The result is projected into the E769 planes. Hits in these planes found consistent

[1]PWC and D1 hits are not used because these detectors have poorer spatial resolution than do the SMDs.

with the projected track are included in a fit to determine the slopes and intercepts of the track for the region of the spectrometer upstream of the analyzing magnets. Otherwise, the projected track itself is used to determine the track parameters. Only those tracks fits with a low χ^2/dof are retained.

After the SMD tracks are formed, they are projected through both analyzing magnets to D3 in the yz plane, the non-bend view of the magnets. By finding clusters at the appropriate positions there is further evidence that the tracks are not fake. D3 is used instead of D2 because it a has a lower density of tracks in its center. D4 is not used because it doesn't have many planes. The x positions of the matching clusters, combined with a single bend-point approximation for both magnets, are used to establish the particle's trajectory through the spectrometer so that DC clusters in D1, D2 and D4 can be assigned to tracks. Subsequently, a more thorough fitting procedure is performed in which the track slopes, intercepts and momentum are determined. This fit uses SMD, PWC and DC clusters along with a field map of the analyzing magnets to minimize the χ^2 of the trajectory. At this point, cuts are placed on the total χ^2/dof for the trajectory and on the number of SMD hits per track. Afterwards, any remaining DC clusters are formed into tracks originating downstream of the SMD system.

For each track, a 16 bit word is recorded in the event which notes the DC stations that contribute hits to it. This information is recorded in a bitwise fashion and is referred to as the category of the track. The lowest order bit is on when the track has hits from D1. The next order bit is used for D2, and so on. So, a category 7 track has hits from D1, D2 and D3 ($1 + 2 + 4 = 7$).

3.2 PASS2

3.2.1 Vertex Reconstruction

The vertex reconstruction algorithm takes as input tracks fitted only with the silicon hits and begins by forming two track vertex candidates. Even when the tracks come

from a common vertex, their distance of closest approach (impact parameter) is non-zero due to finite measurement error. Sometimes, therefore, there will be more than one vertex into which the track will fit. The philosophy is to report all reasonable track combinations that could form a vertex, thus making a conservative estimate of the number of vertices, erring on the side of overestimating.

The vertex reconstruction can be visualized as checking the overlap of a list of ellipsoids, where the axes lengths of the ellipsoid are taken from the error matrix of the vertex. The algorithm begins by forming two track vertices with a constrained fit, i.e., that is they are assumed to come from a common point. A vertex is kept if its $\chi^2/dof < 2.0$. Then, tracks are added one at a time to get as many of them to make a vertex as possible. From the left over tracks failing the vertex cut, one tries to make new vertices, considering even those tracks that are already being used in another vertex, i.e., track sharing between vertices is allowed.

3.2.2 SLIC Reconstruction

After running PASS0 on data to establish the gains for the calorimeter channels, the ADC values are converted to energies. Adjacent channels whose outputs are above a 75 MeV threshold are grouped together, the result being called a cell. The cells are subdivided into sectors, which are sets of channels clustered about local maxima within the cell. These sectors are then fit via a stepwise regression [32], which is a linear least squares fitting technique, to determine significant sectors and divide the total cell energy among them. In addition, the transverse energy distribution of each sector is fit to a linear combination of an electromagnetic shower shape and a hadronic shower shape to describe the character of the shower. Next a candidate list is made of all uvy sector triplets whose v and y sector positions predict the u positions, the result being a set of energy clusters. These clusters are then fit by stepwise multiple regression which assigns energies and energy errors to them. Those sectors which are not assigned are tested by pairs with the hypothesis that they are photons from π^0 decays which are created in the target. If the invariant mass of the pair is near the π^0 mass, their energies are combined to form the π^0 energy.

Once energy is assigned to tracks and neutrals have been formed, two analysis

variables for each particle are introduced. They are called JCAL and ICAL and are of interest to those who wish to perform an analysis of E769 data. The general reader does not need to be concerned about them. Both variables are documented in the MONIPAM Fortran code library. JCAL is a flag which notes any unusual condition observed during reconstruction which might require careful consideration before the particle is used for physics analysis. For charged tracks, JCAL normally holds the value of the track's index in the track list. One reason for JCAL to be different from the track index is if the track is used to reconstruct a neutral particle, e.g., an electron found to come from a photon conversion. ICAL is a rough guess of the identification of the particle based on amount of EM energy, hadronic energy and a signal in the correct location of the muon wall. With this and tracking information, identification categories are electrons, muons, pions, kaons, protons and neutrals. The last task performed in the calorimeter reconstruction is the electron identification on the charged tracks which have energy clusters assigned to them. This is discussed below.

3.2.3 Description of Electron Identification

Most of the charged secondaries from an interaction are hadrons. By studying the shower characteristics of charged particles in the SLIC, electrons can be identified in the presence of this hadron background. This section describes the method of the electron identification procedure developed and implemented by Rollin Morrison of UCSB for E691. A detailed discussion of the electron identification can be found in Appendix A. The fact that E691 was a photo-production experiment with a different CM energy from E769 (a hadro-production experiment) does not significantly alter the ability to distinguish pions from electrons. The environment characteristics which affect identification, such as the average charged track multiplicity and average occupation of calorimeter channels, are similar between the two.

For each charged track, the electron ID algorithm calculates EPROB[2] which represents the likelihood that the track is an electron. Though not a probability, the

[2]For E769 collaborators, EPROB is known in the reconstruction as the fortran function EMPNEW. The resulting value of this function is stored in the track array EMPROB.

larger the number the more likely it is that the track is indeed an electron. This number is used as a cut in the analysis.

The idea is to study the behavior of $e^{\pm}$ and $\pi^{\pm}$ in the calorimeters, and develop a series of tests which can be used to distinguish them. EPROB is based on a factorization hypothesis of the charged track characteristics, meaning that the characteristics are uncorrelated and independently contribute information that can be used for e/π separation. As an analogy to this assumption, consider the following example. Imagine the space of functions parameterized by many variables. Applying the factorization hypothesis is equivalent to restricting consideration to the set of functions that are separable. By studying the characteristics independently, the parameterization process is simplified because we ignore cross terms between the analysis variables.

Samples of $e^{\pm}$ from $\pi^{\pm}$ are studied as a function of

- the track momentum,
- the radial position of the energy cluster in the calorimeter,
- the amount of energy deposited in the hadrometer,
- the position difference between the track and the shower centroid,
- the transverse distribution of the shower about the centroid and
- the difference between the energy measured in the electromagnetic calorimeter and the momentum measurement.

From these studies, we construct the probabilities $P(e \rightarrow e)$ and $P(\pi \rightarrow e)$ which are the probability that an electron is identified as an electron and the probability that a pion is mis-identified as an electron respectively. From these probabilities, we construct the likelihood (EPROB) that a given track is an electron:

$$\begin{aligned} \text{EPROB} &\equiv 100 \times \frac{P(e \rightarrow e)}{P(e \rightarrow e) + P(\pi \rightarrow e)} \\ &= 100 \times \frac{1}{1 + \frac{P(\pi \rightarrow e)}{P(e \rightarrow e)}}. \end{aligned}$$

A value of EPROB is calculated for each charged track that is reconstructed in the spectrometer. To ascertain the performance of the electron identification, one needs a

source of $e^{\pm}$ and $\pi^{\pm}$. The electron identification efficiency and pion mis-identification probability can be determined as a function of EPROB observing the electron and pion signals before and after cutting on EPROB. A study of this sort has been performed and is discussed in Section 5.2.

SLIC Performance and its Effect on Electron Identification

In this section, we discuss the performance of the SLIC prototype in a test beam of 4 GeV/c electrons [29]. The prototype differs from the SLIC only in that it consists of five channels transverse to the beam which has no bearing on electron shower studies. We focus on those aspects of the detector response which have an immediate bearing on its ability to perform the electron identification. There are two plots from this study which are of interest to us here. The first is shown in Fig. 3.1 in which we see the energy spectrum measured in the calorimeter where the value plotted is the sum of the signals from the five channels. The abscissa is shown in units of the central channel's energy, i.e., the energy in the central channel is defined to be one. This plot demonstrates that $1/1.455 = 69\%$ of the energy of the electron's shower is deposited in the central channel. In addition, we see that the energy resolution is $\sigma/\mu \simeq 9\%/\sqrt{E}$. Note that the energy resolution of the SLIC (Section 2.10.1) is slightly worse than this because it operates in a busier environment. This plot demonstrates the utility of studying the momentum-energy difference of a track when performing the electron identification.

The showers due to electrons and pions will look very different. A shower initiated by an electron will occupy only a few channels, while a shower initiated by a pion will be wider, which has two effects. First, if the pion shower is not fully contained in the SLIC (either because of punch-through or a shower which is not transversely contained), the SLIC energy is an underestimate of the track's energy. Second, an electron shower has a greater chance of having all of its energy associated with the track. The wider the shower the greater the probability that it will overlap with another shower and at times share its energy with the other cluster.

Another important aspect of the calorimeter is its position resolution, which is demonstrated in Fig. 3.2 for a typical set of events. The value $\sigma = 0.23$ cm is

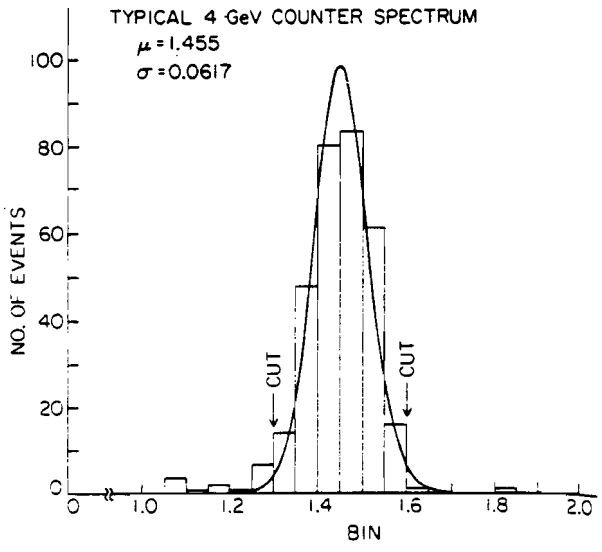

Figure 3.1: Energy resolution of the SLIC prototype in a 4 GeV/c electron beam. The signal is the sum from five channels and is normalized so that the central channel has value one.

the standard deviation of the mean of the distribution. Because of the finite electron beam size, this value is larger than the true resolution, but serves to set the scale. The shower position resolution is used in the electron identification procedure to remove photons whose showers overlap with charged track showers. In addition, because a pion's shower tends to be wider than an electron's shower, the uncertainty of a pion shower's central position is larger than that of an electron. Thus this is another way to distinguish electrons and pions.

3.3 Pair Strip

E769 recorded approximately 400 million events on 10,000 nine track tapes. In DST format, this would correspond to approximately 3700 nine track tapes. Because this is an unreasonable number of tapes with which to do physics analysis, two things were done. First, the DST events were written to exabyte tapes, which reduces the number to approximately 300. Most of these events are from either minimum bias interactions or interactions with few secondaries passing through the geometrical acceptance of

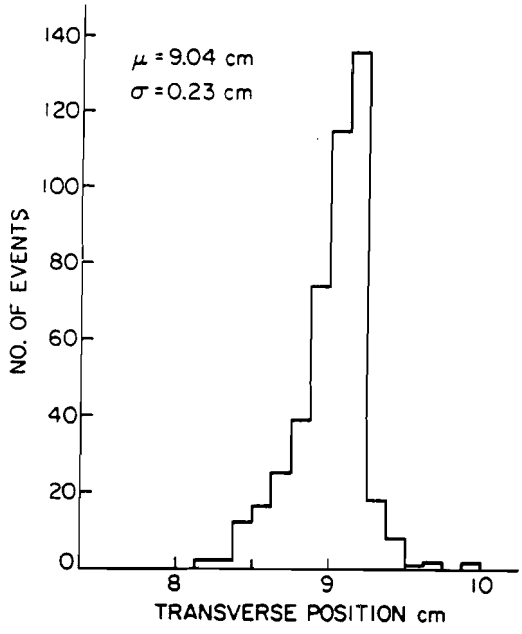

Figure 3.2: Position resolution of the SLIC prototype in a 4 GeV/c electron beam. The width of this distribution is dominated by the electron beam size.

the spectrometer. The number events is further reduced by analyzing each event with a fast filtering algorithm known as the pair strip. The purpose of the pair strip is to enrich the data sample with heavy quark events while spending as little CPU time per event as possible.

The pair strip algorithm reads DST events and selects those containing more than one vertex. Since the vertex reconstruction is done in PASS2, the DST event already has a vertex list. In the case that the event passes the strip cuts, it is this list that is retained. From the vertex list, the one with the most tracks is designated as the primary (production) vertex. New vertices are constructed one at a time from all two track combinations. If either or both of the tracks is in the primary vertex, they are removed and the primary is refit without them. If the event passes the cuts shown in Table 3.1, it passes the pair strip. The quantities $z(pri)$ and $z(sec)$ are the z positions of the primary and candidate secondary vertices, $\sigma(pri)_z$ is the error on the primary vertex position and $(\chi^2/dof)_{sec}$ is the χ^2 per degree of freedom of the secondary vertex. RAT is a product of ratios for secondary tracks. The numerator is the impact parameter of the track to the secondary vertex. The denominator is the

Table 3.1: Pair strip cuts.

Variable	Cut
$z(pri)$	> -6 cm
$\sigma(pri)_z$	< 180 μm
$z(sec)$	> -6 cm
$(\chi^2/dof)_{sec}$	< 5.0
RAT	< 0.06
SDZ	> 6.0
$PT2DK$	> 0.1 (GeV/c)^2

impact parameter of the track to the primary vertex. The expression for RAT is

$$RAT = \prod_{i=1,2} \frac{b(sec)_i}{b(pri)_i} \tag{3.1}$$

where $b(pri)_i$ and $b(sec)_i$ are the impact parameters of the candidate secondary track to the primary and secondary vertices respectively. SDZ describes the statistical significance of the separation of the primary and secondary vertices and is defined as

$$SDZ = \frac{z(sec) - z(pri)}{\sqrt{\sigma(sec)_z^2 + \sigma(pri)_z^2}} \tag{3.2}$$

where $\sigma(sec)_z^2$ is the error in z of the secondary vertex position. PT2DK is the sum of the squares of the p_T of the secondary tracks:

$$PT2DK = \sum_{i=1,2} (p_T^2)_i, \tag{3.3}$$

where the p_T is defined relative to the momentum sum of the two tracks. With these cuts, the event rejection is approximately ten. Thus, 26 million reconstructed electron trigger events (all from the positively charged beam data) are reduced to 2.5 million on the pair strip tapes. The number of pair strip tapes is reduced from 300 to 30.

Chapter 4

Monte Carlo Simulation

In this chapter, the Monte Carlo (MC) simulation of heavy quark events is described. Included in the MC analysis is a simulation of the detector response. MC events are then reconstructed and analyzed in the same way as the data. We simulate the heavy quark decays for two reasons. First, we need to know that acceptance due to analysis cuts, detector efficiencies, trigger effects, etc. With this, we can correct our measurements to obtain the total cross sections. The other reason is that our method for determining the heavy quark cross sections requires that we know the shapes of the p_T^2 and d distributions that are used in the data fit. In principle, the analysis cuts change these shapes, so they must be determined from the MC simulation.

4.1 The Event Simulator & Digitizer

The MC Simulator uses Jetset v.6.2 [36] and Fritiof v.1.3 [37], both packages from CERN. Jetset is used to decay the particles and Fritiof is used to simulate the nuclear fragmentation of the event. For Jetset, the particle masses, lifetimes and branching fractions are updated to current Particle Data Group [2] values. In addition to these packages, the heavy quark pair is produced according to LO QCD predictions with $m_c = 1.7$ GeV/c^2, $m_b = 5.0$ GeV/c^2, $\Lambda = 200$ MeV and $\mu = m^2$. Finally, the MC simulator performs a full simulation of the event in the spectrometer including multiple scattering, secondary interactions, pair production and bremsstrahlung. The

simulation of bremsstrahlung of electrons is detailed in the section below.

After MC events are generated and simulated in the spectrometer, the event is converted into hits and phototube signals for each detector in the spectrometer. The inefficiency and noise of each detector are included, as determined from real data. This information is then placed into the data format so that it can be treated in the same manner as a data event.

Bremsstrahlung of Electrons

The MC simulator was specially modified for this analysis to include the effect of bremsstrahlung on the electrons that pass the analysis cuts, whether or not they are from heavy quark decays. Bremsstrahlung is the radiation of photons due to the charged particle interacting with the material through which it passes and it dominates over losses due to ionization when the particle is ultra-relativistic. Therefore, bremsstrahlung of other particle types is not considered. Both the nucleus and the orbital electrons contribute to bremsstrahlung [38]. The interaction probability for the nucleus is proportional to Z^2 and the probability for the atomic electrons is proportional to Z. For the materials considered here (the target foils, and interaction counter) the nuclear contribution dominates even when including the screening effects the atomic electrons have on the nuclear charge. The probability density that an electron will emit bremsstrahlung radiation reducing its energy by a factor of $e^{-\zeta}$ is given by (valid for small amounts of material only)

$$\frac{dN}{d\zeta} \propto e^{-\zeta}\zeta^{bx-1}, \tag{4.1}$$

where x is the thickness of the material in radiation lengths and b describes the material dependence of the medium and is approximately constant ($\sim$1.3 for the target materials and scintillator). In other words, the relationship between the initial (E_i) and final (E_f) energies of the electron that emits bremsstrahlung radiation is $E_f = E_i e^{-\zeta}$. Recall from Sec. 2.4 that the target and scintillators combined are only 20% of a radiation length. Performing a change of variable $y = e^{-\zeta}$ Eq. 4.1 becomes

$$\frac{dN}{dy} \propto (-\ln y)^{bx-1}, \tag{4.2}$$

where y is the fraction of energy the electron has remaining after radiating the photon.

When an electron in the MC simulation passes the analysis cuts, a random number is generated according to the above distribution to determine how much energy it loses. Bremsstrahlung is only applied as a correction to the p_T distribution of the electrons. This means we neglect the effect on the electron identification, which is done for the following reason. In the MC simulation, when an electron does not emit bremsstrahlung radiation, it is the same as if it were a larger momentum electron that did. This is true because the photon is radiated in the target region in the direction of the electron. The electron then passes through the analysis magnets and is kicked away from the photon. By the time the two particles interact in the SLIC, they are well separated and their showers do not overlap. That they do not overlap can be seen from the following example. Consider a 20 GeV/c electron with $p_T = 1 GeV/c$ in the bending view of the analysis magnets. In addition, assume that the electron emits a photon in the target which carries 6% of the electron's momentum. (More than 90% of the electrons lose no more than this.) If the target is 19 m from the SLIC and the bend of the electrons trajectory is assumed to occur 6 m from the SLIC, then the electron and photon are 22 cm apart when they interact in the SLIC. Since electromagnetic showers are typically 4-5 cm wide, these are well separated. Since the photon and electron are well separated in the SLIC, the difference between including and not including bremsstrahlung is just to modify the momentum distribution of the electrons in the MC simulation. But the electron identification categorizes the momentum in very coarse bins so that this effect is minimal. We therefore conclude, that it is appropriate to exclude bremsstrahlung corrections as far as the electron identification is concerned.

4.2 Electron Trigger Simulation

One purpose of the MC simulation is to determine the acceptance in the detector for a specific physics process. Part of the acceptance comes from the trigger with which the data is collected. Ideally, the acceptance of events collected with a E_T trigger is a step function when examined in E_T. However, because of the calorimeter resolution,

the actual distribution is a smeared step function. To correct for the effect of the trigger, we must determine the trigger acceptance as a function of E_T. One way this could be done is through a simulation of the trigger in the MC analysis. In this way, the signals from the calorimeter channels are weighted and summed in the same manner as the data trigger. This is not the method implemented here because of the complication introduced by the out-of-time energy (see Section 2.12). This causes a shift in the E_T spectrum (recall Fig. 2.15) making a MC determined efficiency in E_T unreliable without a simulation of the out-of-time energy. Instead of simulating the trigger in the MC analysis, we have parameterized the trigger efficiency from data as a function of the total p_T as measured from the reconstructed charged tracks with hits in drift chambers D1, D2 and D3. We define this quantity to be $p_T(\text{tot})$[1] and includes only those tracks with a momentum less than 200 GeV/c, at least 20 hits assigned to the track from the drift chambers, and a global track $\chi^2/dof < 5.0$. These cuts are imposed to remove fake tracks caused by high hit density in the central region of the drift chambers. This parameterization is less sensitive to the effects of out-of-time energy than E_T because the calorimeters, upon which E_T is based integrate their signals much longer than do the drift chambers. Therefore, the calorimeters are more sensitive than the drift chambers to multiple beam particles interacting in the target.

Fig. 4.1 shows the efficiency of the $E_T(\text{high})$ part of the electron trigger as a function of $p_T(\text{tot})$. This was determined from pair strip data events recorded with the interaction trigger. The trigger information for each event is stored in such a way that we know which trigger recorded the event and which other triggers the event satisfies. From these events, the efficiency for a trigger is defined relative to interaction triggers. Since the production of a heavy quark pair requires that there be an interaction, this efficiency is exactly what we need to correct MC events for the trigger acceptance. The trigger efficiency is parameterized by

$$\epsilon = P1 - \frac{P2}{1 + exp(\frac{p_T(\text{tot}) - P3}{P4})}, \tag{4.3}$$

the fitted form of which is shown in Fig. 4.1. The Pi are parameters to be determined from the fit and their values are shown in Table 4.1. When the MC analyses are

[1]This is called PT715 in the E769 analysis code

performed, this function is used to generate a weight for the event that is used to modify the electron p_T and d distributions.

Table 4.1: The fit results of the trigger efficiency parameterization as a function of p_T(tot).

Quantity	Value
P1	0.858 ± 0.017
P2	0.817 ± 0.019
P3	4.281 ± 0.049
P4	1.137 ± 0.030
χ^2/dof	1.06

The high p_T electron contribution to the electron trigger is simulated in the MC events from the calorimeter energies. The SLIC y channels are searched for a channel with $E_T \gtrsim 0.5$ GeV, independent of the position of the electron.

4.3 Charm MC Simulator

It was mentioned in Section 4.1 that charm quarks are generated according to the LO QCD prediction with $m_c = 1.7$ GeV/c^2. The x_F and p_T distributions of this generator for charged and neutral D mesons are not the same as those measured in E769 [39] data. E769 finds that the meson x_F distribution is fit best by $d\sigma/dx_F \propto (1-x_F)^{3.9\pm.3}$ in the range $0.1 < x_F < 0.7$, and the transverse momentum dependence is best parameterized by $d\sigma/dp_T^2 \propto exp(-(1.03 \pm .06)p_T^2)$ in the range $p_T < 2$ GeV/c and $d\sigma/dp_T^2 \propto exp(-(2.76 \pm .08)p_T)$ in the range $0.8 < p_T < 3.6$ GeV/c. For this analysis, we assume that these distributions can be applied to all charm hadrons. The charm MC events are modified by weighting each hadron according to its x_F and p_T so that the weighted distribution is the same as that measured by E769.

Because the heavy quark cross sections are determined from inclusive semi-leptonic decays, in general the fragmentation model used by the MC simulator is important. Consider the case of charm. The hadrons that decay semi-leptonically have different

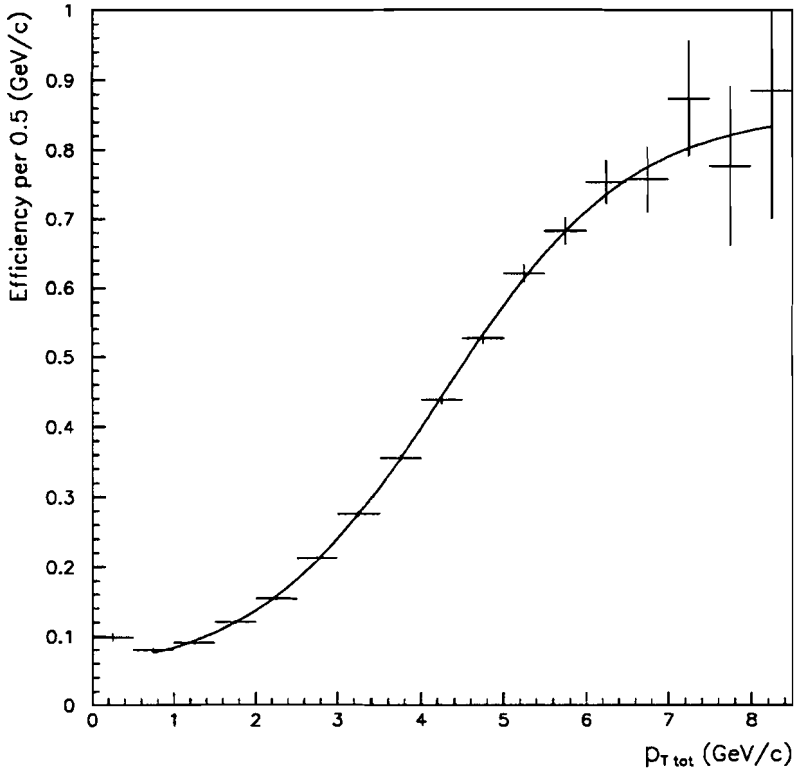

Figure 4.1: Electron trigger efficiency without the high-p_T electron requirement.

branching fractions and therefore different lifetimes. Since impact parameter information, which is used in this analysis, is correlated with particle lifetime, different fragmentation models change the analysis result by modifying the shape of the d distribution of electrons from charm.

The relative amount of each hadron produced in a charm event also determines the effective branching fraction for the $c\bar{c}$ pair because

$$B(c\bar{c} \rightarrow eX) = 2\left(\sum_{i=1}^{n} f(c \rightarrow X(c)_i)B(X(c)_i \rightarrow eX)\right) \tag{4.4}$$

where n is the number of charm hadrons($X(c)_i$) which decay semi-leptonically and $f(c \rightarrow X(c)_i)$ is the fragmentation fraction for a $c(\bar{c})$ quark into hadron $X(c)_i$. The fragmentation fractions are not well known, so different models can be put forward that obey the constraints that have been observed. This will be readdressed in Section 6.1 when systematic errors are discussed. The fragmentation model used by the charm MC simulator produces hadrons with fractions listed in Table 4.2. This table also lists the semi-leptonic branching fractions. The D_s^+ branching fraction has not been measured; the value of 10% is an estimate, which is shown in the table by the (*est*) notation.

Table 4.2: Charm MC fragmentation and branching fractions (c.c. implicit).

Hadron	Fragmentation	$B(X_c \rightarrow eX)$
D^0	0.59	0.070
D^+	0.29	0.182
D_s^+	0.09	0.100(*est*)
Λ_c^+	0.02	0.045
other	0.01	—

4.4 Beauty MC Simulator

Recall from Section 4.1 that beauty quarks are generated according to the LO QCD prediction with $m_b = 5.0$ GeV/c^2. There are no measurements of the b hadron

x_F and p_T distributions from pion induced events at our CM energy with which to compare the MC predictions. Instead, we use the perturbative QCD predictions of b quarks from References [41, 3]. The x_F distribution for b quarks is taken from a NLO prediction, while the p_T distribution for b quarks is taken from a LO prediction. At this time, there is no published NLO prediction of the p_T distribution of b quarks for pion induced beauty events near this CM energy. However, the NLO prediction is not expected to be significantly different from the LO prediction. Evidence for this comes from Reference [3], where the NLO prediction of the b quark p_T distribution from proton induced events at collider energies does not significantly differ from the LO prediction. The theoretical predictions are slightly different from the distributions produced by the MC generator. To correct the x_F and p_T distributions produced by the MC generator, we assume that fragmentation does not alter them so that the theoretically predicted b quark distributions can be applied to beauty hadrons. As in the case of the charm MC events, the distributions are modified by weighting each hadron.

Unlike the case for charm physics, all of the beauty hadrons are expected to have approximately the same lifetime which means their semi-leptonic branching fractions are approximately the same. Supporting evidence, for example, comes from current Particle Data Group values of the B meson lifetimes and the recent b baryon lifetime measurement from ALEPH [40]. As a result, different fragmentation models give the same d shape and the same effective branching fraction $B(b\bar{b} \rightarrow eX)$. So, beyond the branching fraction uncertainty, the beauty fragmentation model does not contribute uncertainty to the total cross sections.

Chapter 5

Data Analysis

The sections of this chapter are devoted to a detailed explanation of the analysis method to study charm and beauty production. This includes

- a description of the the analysis method;
- the cuts imposed on the data set, to extract the physics of interest;
- an analysis of MC events with cuts imposed;
- an analysis of the backgrounds to semi-leptonic decays.

In the discussion of the background study, the dominant sources are identified and their individual contributions are estimated.

5.1 The Analysis Method

The objective is to determine the total beauty and charm production cross sections from a search for inclusive semi-leptonic decays of heavy hadrons. Because of the missing neutrino energy, the heavy hadron cannot be reconstructed so its invariant mass cannot be calculated. Instead, the analysis studies one of the decay products: the electron. The electron from a heavy hadron decay is characterized by its miss distance to the primary vertex (d) and high transverse momentum (p_T). On average,

the heavier the quark produced, the larger the mean p_T; the longer lived the heavy hadron, the larger the d.

To motivate the analysis method, consider figures 5.1 and 5.2 which are the p_T^2 and d distributions respectively from unweighted MC events without analysis cuts for the three categories into which all events are classified: minimum bias[1], charm and beauty. Tracks from minimum bias events have a p_T^2 distribution with a peak near 0.4 (GeV/c)^2. Immediately past the peak the distribution falls very rapidly. At larger values of p_T^2 (> 2 (GeV/c)^2), the tail of this distribution flattens. In this region, minimum bias models which predict the p_T distribution become unreliable. This point will be addressed shortly. The d distribution of minimum bias events is characterized by a very sharp drop followed by an slowly varying tail. The tail of this distribution is due to strange particle decays, which have lifetimes $\gtrsim 10^2$ times larger than the longest lived heavy hadrons. For example, the K_s^0 lifetime is $c\tau \simeq 2.7$ cm while the D^+ lifetime is $c\tau \simeq 0.03$ cm. So, tracks from strange particle decays are expected demonstrate a longer d distribution than are tracks from heavy hadron decays.

Tracks from charm events have a p_T^2 distribution with a peak near 0.5 (GeV/c)^2. This distribution drops rapidly thereafter. For large values of p_T, the p_T^2 distribution of charm hadrons is parameterized well [39] by the form $exp(a - b \times p_T)$. High p_T electrons are also parameterized well by this form, as the MC simulation from this analysis will show. This shape appears as an exponential distribution with a tail when viewed versus p_T^2. The d distribution falls like a simple exponential even though these tracks come from particles with different lifetimes. The reason for this is that we measure the d from one track of a hadron decay, not the d of the hadron itself. As a result, d is not a measure of hadron lifetime though it is correlated to hadron lifetime. The effect of measuring d for one track is to mask the lifetime differences among charm hadrons such that we measure an effective lifetime. The decay length of these tracks is much longer than that from most minimum bias events, which will be useful in distinguishing between the two types.

Tracks from beauty events have a p_T^2 distribution with a peak near 1 (GeV/c)^2.

[1]A minimum bias event is one which does not produce heavy quark hadrons.

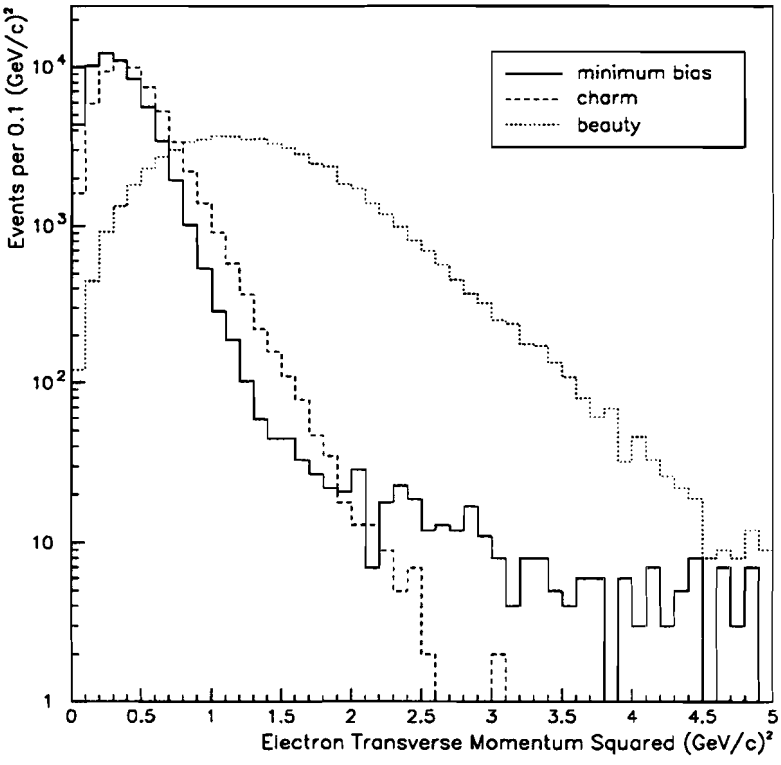

Figure 5.1: MC p_T distribution of tracks from minimum bias, charm and beauty events.

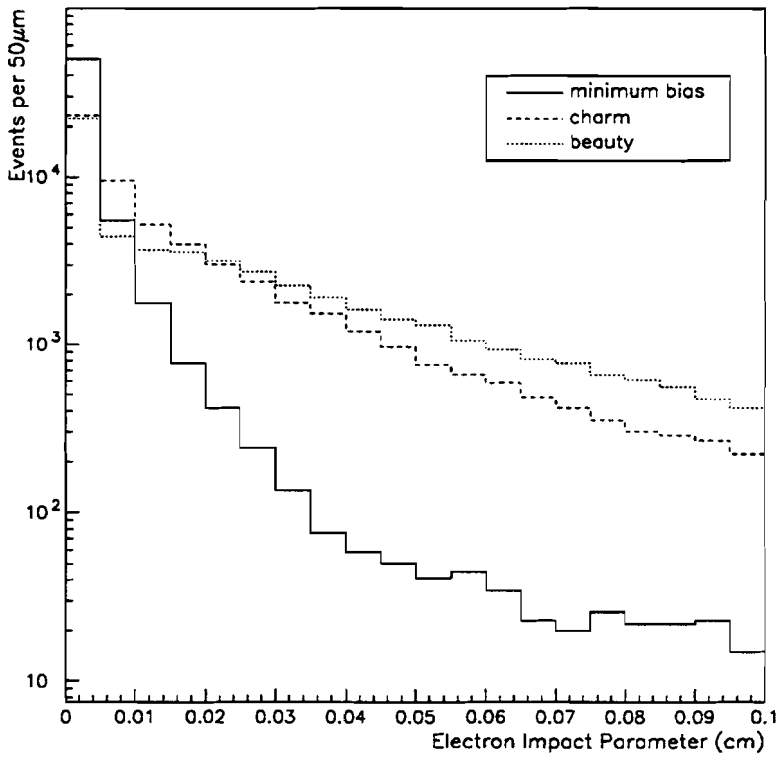

Figure 5.2: MC d distribution of tracks from minimum bias, charm and beauty events.

The distribution falls rapidly thereafter, slower than charm and minimum bias events. As in the case of charm, a single curve will describe the d distribution. This effective lifetime is close to the effective charm lifetime, so it is the p_T^2 distribution which will be most important in distinguishing the beauty signal from the charm.

The physics cross sections are extracted from a fit of the two dimensional distribution of electron p_T^2 and d. This fit involves three terms: one each for electrons from charm, electrons from beauty, and background tracks. Backgrounds are discussed below in Section 5.5 in which various sources are considered. In anticipation of this discussion, consider the background to be due to tracks from minimum bias events, so that there is no background due to heavy quark processes. All of the parameters which describe the p_T and d dependence (called shape parameters) are fixed in the fit of the data, while the amplitudes of the three terms are allowed to vary. The shape parameters for electrons from charm and beauty are taken from the MC simulations described in Chapter 4. The background shape parameters are taken from a sample of minimum bias events in the data because in the kinematic region defined by the data cuts (see below) the distribution of minimum bias events cannot be reliably predicted from MC simulation.

5.2 Electron Identification Performance

The electron identification (ID) from calorimeter information is heavily relied upon in this analysis. We need to know the acceptance of the EPROB cut for E769 data to verify that the MC simulation is correct. Furthermore, we can use the electron ID efficiency and the pion mis-ID probability determined for this cut to estimate the size of our backgrounds. To characterize the performance of the electron identification algorithm for E769 data, we have performed a study determining the electron ID efficiency and the pion mis-ID probability.

Determination of the Electron ID Efficiency

To determine the electron ID efficiency, we need a source of electrons with which we can test the electron identification algorithm. A plentiful source of electrons can

be found from photon conversions. Since the photon is massless, the electron and positron have zero invariant mass and transverse momentum relative to the direction of the photon. Because the measured quantities are smeared by the experimental resolution, the invariant mass and transverse momentum are very small but not exactly zero. To find conversion pairs, we loop over all oppositely charged two track combinations, keeping those with the following characteristics.

- Both tracks are composed of hits from D1, D2 and D3.
- Both tracks point to the electromagnetic calorimeter.
- The tracks pass within 2 cm of one another.
- No other track passes through their common vertex.
- Their relative squared p_T sum is < 0.002 (GeV/c)^2.

We define this last item to be p_T^2(sum) is defined to be

$$p_T^2(\text{sum}) = \sum_{i=1,2} (p_T^2)_i, \tag{5.1}$$

where transverse is defined relative to the direction of their momentum sum. These pairs are used to determine the efficiency by first cutting on the EPROB of one track (the first track that appears in the reconstruction list). This defines the set of electron pair candidates.

Fig. 5.3 shows the distribution of p_T^2(sum) for events passing the cuts described thus far for EPROB ≥ 99. The slowly varying part of the distribution at high p_T^2(sum) is due to background pair combinations. This part of the distribution is fit to a line, which is then extended under the peak to get the background subtracted number of electron pair candidates in the first bin ($p_T^2(\text{sum}) < 4 \times 10^{-5}$ (GeV/c)^2)). This is the electron sample and is the denominator in the efficiency ratio. Finally, the same EPROB cut is imposed on the other track of the pair. Fig. 5.4 shows that this removes almost all of the high p_T^2(sum) entries. The number of tracks that remain in the first bin after a similar background subtraction is the numerator of the efficiency ratio.

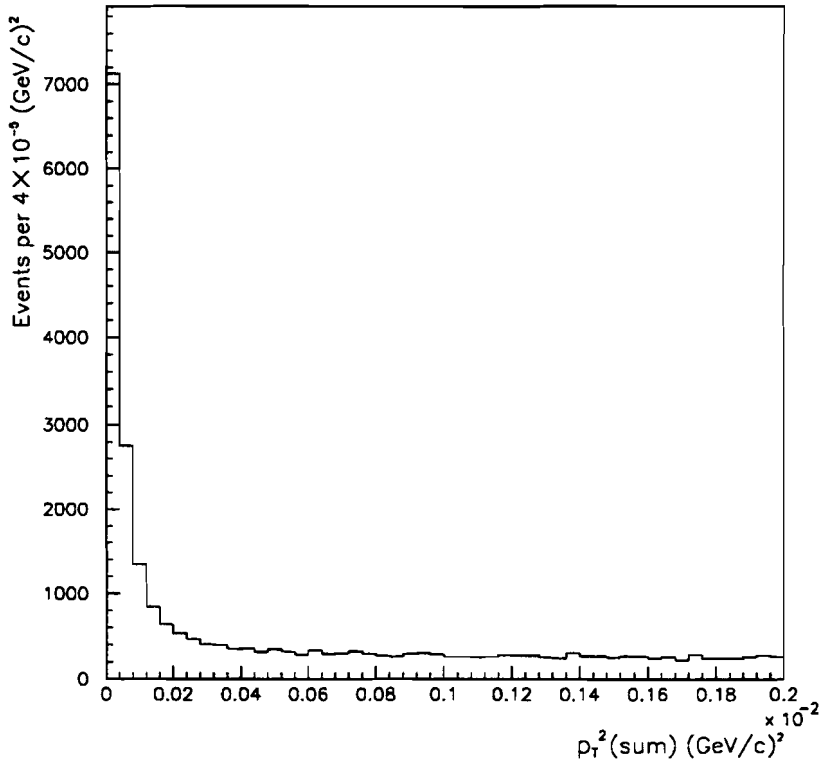

Figure 5.3: $\Sigma p_{T\,e}^2$ distribution of electron pair candidates after cutting on EPROB for one track.

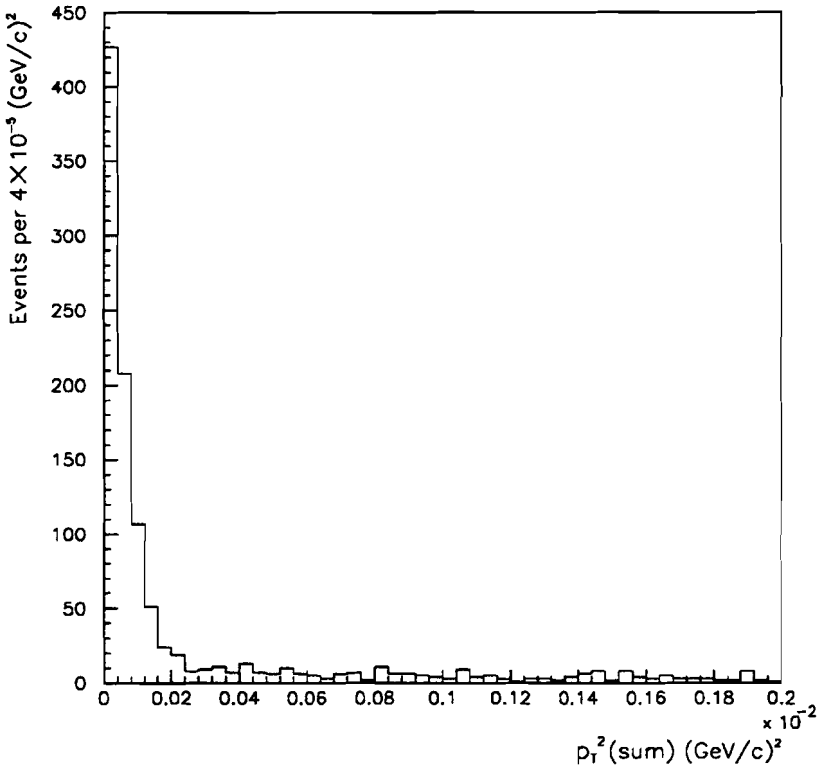

Figure 5.4: $\Sigma p_{T_e}^2$ distribution of electron pair candidates after cutting on EPROB for both tracks.

Determination of the Pion Mis-ID Probability

To determine the pion mis-ID probability, we need a source of charged pions with which we can test the electron identification algorithm. K_s^0 decays are a plentiful source of charged pions as the branching fraction for $K_s^0 \rightarrow \pi^+\pi^-$ is 69%. To find pions from K_s^0 decays, we loop over all oppositely charged two track combinations, keeping those with the following characteristics.

- The tracks have an invariant mass within 150 MeV/c^2 of the K mass.
- Their common vertex lies between the silicon planes and D1.
- The tracks pass within 2 cm of one another.
- No other track passes through their common vertex.
- The product of the Čerenkov pion probabilities for the particles is greater than 0.5

A plot of the invariant mass (see Fig. 5.5) is made of the remaining K_s^0 candidates, which is fit to a gaussian plus linear background. The width and mean are used as constants in the subsequent fits. The EPROB cut is then imposed on each pion remaining in the sample. The invariant mass is plotted for those combinations where one of the two tracks passes the EPROB cut (there was no case where both tracks passed the EPROB cut). The distribution is again fitted with a gaussian plus linear background. The mis-ID probability (ξ) is the ratio of the integral of the two gaussians

$$\xi = \frac{A \int exp(-\frac{1}{2}\left(\frac{x-m_K}{\sigma}\right)^2)dx}{2B \int exp(-\frac{1}{2}\left(\frac{x-m_K}{\sigma}\right)^2)dx}, \tag{5.2}$$

where the denominator represents the pions from the distribution before imposing an EPROB cut and the numerator represents the pions from the distribution after imposing the EPROB cut. A and B are the amplitudes of the fitted gaussian distributions. The factor of two in the denominator comes from the fact that each K_s^0 decay has two pions that could be misidentified. The two integrals in Eq. 5.2 are

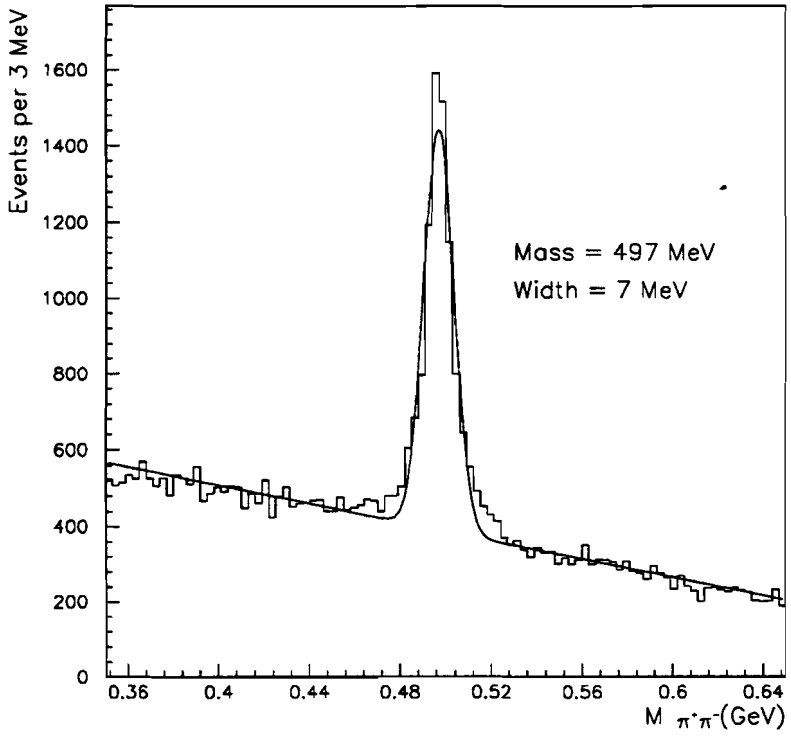

Figure 5.5: K_s^0 mass peak defining $\pi^{\pm}$ sample.

identical since the mass and width is the same in both fits. As a result, the pion mis-ID probability reduces to

$$\xi = \frac{A}{2B}. \tag{5.3}$$

Choosing the EPROB Cut Value

The electron identification efficiency and the pion mid-identification probability are determined from data for various minimum cut values of EPROB, which are shown in Table 5.1. The minimum value used in the analysis (EPROB $\geq$ 99) is chosen based on the ratio of the pion mis-identification probability to the electron identification efficiency. This ratio is shown as a function of the minimum EPROB cut in Fig. 5.6,

which demonstrates why the analysis cut value was chosen. The smaller the ratio, the greater the electron enrichment.

Table 5.1: $e^{\pm}$ ID efficiency and $\pi^{\pm}$ mis-ID probability.

Minimum EPROB	$e^{\pm}$ ID efficiency	$\pi^{\pm}$ mis-ID probability
85	0.73 ± 0.01	0.012 ± 0.002
86	0.67 ± 0.01	0.011 ± 0.002
87	0.60 ± 0.01	0.009 ± 0.001
88	0.55 ± 0.01	0.009 ± 0.001
89	0.51 ± 0.01	0.008 ± 0.001
90	0.47 ± 0.01	0.008 ± 0.001
91	0.45 ± 0.01	0.008 ± 0.001
92	0.43 ± 0.01	0.007 ± 0.001
93	0.39 ± 0.01	0.007 ± 0.001
94	0.38 ± 0.01	0.007 ± 0.001
95	0.33 ± 0.01	0.004 ± 0.001
96	0.32 ± 0.01	0.004 ± 0.001
97	0.31 ± 0.01	0.004 ± 0.001
98	0.25 ± 0.01	0.004 ± 0.001
99	0.19 ± 0.01	0.0011 ± 0.0003

5.3 Event Selection

This section describes the cuts placed on the data to select a sample of events for the beauty and charm cross section analysis. We analyze electron trigger events (see Sections 2.12.2 and 4.2) that have passed the pair strip analysis (see Section 3.3).

To select a clean sample of events on which to impose physics cuts, we require

- the primary vertex in the target,
- at least two tracks in the primary vertex and
- an electron candidate with the following track characteristics:

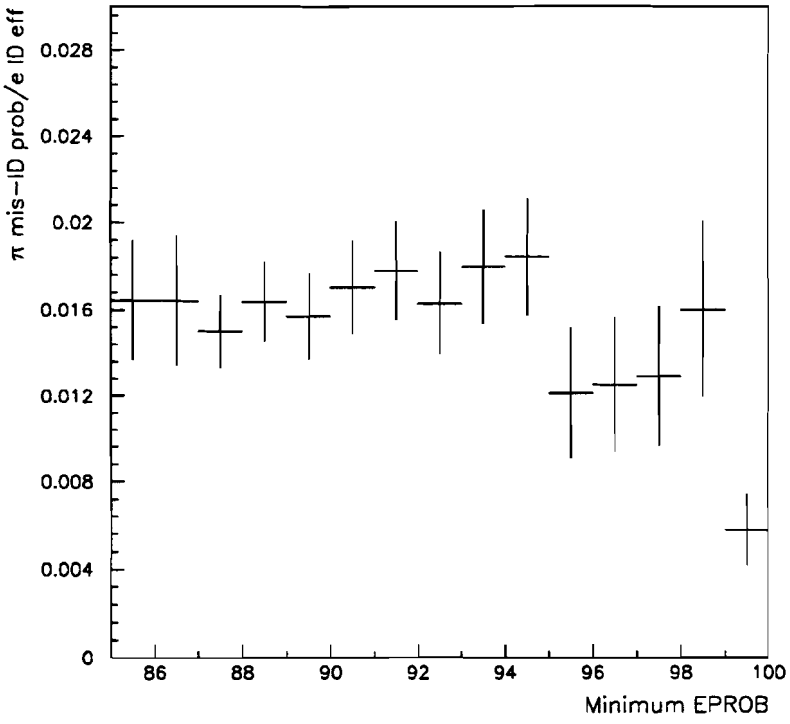

Figure 5.6: Plot of the ratio of the pion mis-identification probability efficiency to the electron identification efficiency as a function of the minimum EPROB value.

- the track is composed of hits from D1, D2 and D3,
- at least two hits from the silicon planes,
- at least 20 hits from the drift chambers,
- $\chi^2/dof \leq 5.0$ from a fit to the SMD hits only,
- $\chi^2/dof \leq 5.0$ from a global fit of SMD and DC hits and
- a trajectory pointing to the fiducial area of the calorimeters.

Other analysis cuts, which require more detailed explanations, are described below.

5.3.1 Beam Particle ID Cut

In Chapter 2 it was noted that the E769 beam is composed of $\pi^{\pm}, K^{\pm}$ and $p^{\pm}$. In Table 5.2 are the results of a study integrating the beam particle flux for each particle type in each data region. A data region is a portion of the data run characterized by different beam conditions. These conditions are 210 GeV/c negative beam (R1), 250/c GeV negative beam (R2), 250 GeV/c positive beam (R3 & R4). For R1-R3, the DISC pressure is set to detect kaons while for R4 it is set to detect protons. The tabulated values are the integrated beam fluxes to which the detector was sensitive. This is not the same as the actual flux because of computer dead-time[2].

In this analysis, we study the π^+ beam sample because of three considerations. First, the data which is analyzed was collected with a trigger that was installed only for the positively charged beam data. Second, the pion induced cross section for beauty and charm is predicted to be higher than that due to protons at our CM energy because the gluon distribution of pions is stiffer than that of protons (recall that gluon-gluon fusion the dominant process for charm production and a large contributor to beauty production). Finally, the pion beam flux is so much higher than the kaon beam flux that the chances of seeing beauty production are best with the pion induced data. The integrated π^+ beam flux ($\simeq 1.6 \times 10^{11}$) is the sum of the R3 and R4 integrated fluxes.

[2]The time during which the DA system's memory buffers are full. Triggers are inhibited until there is room in the buffer to accommodate another event.

Table 5.2: Hadron integrated beam flux for the different regions of the data, which are described in the text.

Particle	R1	R2	R3	R4
π	1.305×10^{10}	6.349×10^{10}	1.525×10^{11}	1.121×10^{10}
K	6.323×10^{8}	1.843×10^{9}	5.871×10^{9}	8.874×10^{6}
p	2.474×10^{6}	6.097×10^{6}	7.941×10^{10}	2.915×10^{9}

Since the particle identification is not perfect, there is an efficiency and a contamination associated with tagging the pions. The efficiency is the probability that pions are correctly identified while the contamination is the probability that kaons and protons are called pions. In this analysis, with a pion efficiency of 87% a negligible kaon contamination and a 2% proton contamination is achieved. The TRD pion detection efficiency is determined by setting the DISC at a pressure so that it is sensitive to pions. The TRD efficiency is that fraction of DISC tagged pions that the TRD also identifies as pions. The contamination due to kaons and protons is determined by setting the DISC pressure so it is sensitive to the particle of interest. The TRD contamination is the fraction of DISC tagged particles that the TRD identifies. The proton contamination, in principle, reflects as an error in the total cross sections because some of the interactions in the analysis sample come from the wrong beam particle type. However, cross section errors due to other effects will turn out to be much larger, so this error is neglected.

5.3.2 Target Cut

The z position of the primary vertex is required to be in the target region. Because the scintillator which detects the interactions contains approximately 15% of the material in the target region, it is an allowed target in this analysis. The allowed z position of primary vertices is from $-5.50 \leq z \leq 0$ cm. The primary vertex is defined to be the most upstream vertex with the most tracks.

5.3.3 Number of Vertices

The number of vertices identified by the vertex reconstruction algorithm is correlated to the kind of physics event being analyzed, as is illustrated by the following. A typical minimum bias event has one or two vertices. One of these is the primary vertex and the other can be due to such things as strange particle decays, secondary interactions or photon conversions. A charm event has three vertices (the primary and two secondaries from the charm decays), while a beauty event has five vertices (the primary, two secondaries from beauty decays and two tertiaries from charm decays). We require each event to have at least three vertices in order to reduce the minimum bias and charm backgrounds. The charm background is reduced by this cut because there is an efficiency for reconstructing vertices due to geometrical acceptance of the SMDs, finite tracking resolution, etc. As discussed in Section 3.2.1, the number of vertices determined during the reconstruction is actually a conservative overestimate of the number of physics vertices, though it is an estimator of the actual number. As a result, some minimum bias events will also pass the cut.

5.3.4 Electron Identification

A charged track is considered an electron candidate if it passes a particle identification (ID) test composed of information from the DC, SLIC and Hadrometer (see Section 3.2.3). Relatively speaking, electrons are a rare occurrence in a hadro-produced event. By far, the most commonly produced particle is the pion, both charged an neutral. Being able to efficiently extract the electron signal is critical to the success of this analysis. This means a large hadron rejection is needed, since percentage-wise even a small hadron background can swamp the physics signal. Muons are expected to have approximately the same abundance as electrons. They are not considered a potential source of background because they are observed as minimum ionizing particles in the calorimeters. Photons are a source of background when a charged track can be projected into the calorimeter at the point where the photon interacts. A cut value on the electron ID probability of $\geq 99.$ was chosen which (see Table 5.1) is approximately 20% efficient for detecting electrons and has 0.1% mis-ID probability

for pions.

5.3.5 Transverse Momentum

The most powerful of the analysis cuts is the cut on the electron candidate's transverse momentum, which can be seen from Fig. 5.1. The electron candidate is required to have a p_T in the range $2 \leq p_T^2 \leq 10$ (GeV/c)^2. The upper bound is chosen simply because this is no data beyond it. The minimum is chosen to remove background, i.e., tracks from minimum bias and charm interactions and is based on acceptance arguments. We assume a cross section and a number of events we want to see in the final sample. From this, a minimum allowed acceptance can be determined, which is used to constrain the p_T cut. Combining the beam flux and target information with the effective branching fraction $B(b\bar{b} \rightarrow eX) = 0.214$, for every electron in the analysis sample that comes from beauty the acceptance is $ACC(b \rightarrow eX) = \frac{0.0168}{\sigma(b\bar{b})}$/electron where the cross section is in nanobarns. We want 10 electrons from beauty in the analysis sample and we assume a beauty cross section of 10 nb. This yields an acceptance (for all cuts) of ~1.7%. With a cut of $p_T^2 > 2$ (GeV/c)^2, the overall acceptance is 1.3%. A tighter cut in p_T will not be helpful unless some other cut is loosened (assuming the beauty cross section is at most 10 nb – recall the theoretical prediction is 2 nb).

5.3.6 Impact Parameter to Primary Vertex

The impact parameter (d) of the electron candidate to the primary vertex is the distance of closest approach of the track when extrapolated back to the primary vertex. The candidate track is required to have d in the range $50 \leq d < 1000\mu$m. The upper limit corresponds to 2.5 B particle lifetimes and is imposed to remove tracks that do not come from heavy quark decays, such as tracks from strange particle decays or secondary interactions.

5.4 Monte Carlo Analysis

5.4.1 Charm

Two million semi-leptonic charm decays were generated, simulated in the detector and reconstructed. The charm hadrons are weighted for the trigger acceptance and the charm hadron x_F and p_T distribution corrections. The acceptance for an electron from a semi-leptonic heavy quark decay to fall within the two dimensional fit area of d and p_T^2 is then calculated as

$$ACC_Q = \frac{\sum_{i(p_T^2)} \sum_{j(d)} g_Q(i,j) w(\mathcal{X}_F) w(\mathcal{P}_T) w(ELE)}{\sum_{i(p_T^2)} \sum_{j(d)} f_Q(i,j) w(\mathcal{X}_F) w(\mathcal{P}_T)} \tag{5.4}$$

where Q is the heavy quark type, i is the index for the bins in p_T^2, j is the index for the bins in d, $g(i,j)$ is the number of electrons in bin i,j after analysis cuts are imposed, $f(i,j)$ is the generated number of electrons in bin i,j, $w(\mathcal{X}_F)$ and $w(\mathcal{P}_T)$ are the x_F and p_T weights of the electron's parent and $w(ELE)$ is the weight due to the electron trigger simulation. From this, the charm acceptance is determined to be $ACC_c = 1.42 \pm .09 \times 10^{-4}$.

Plots of electron p_T^2 and d, which include the weights, are made of the electrons from charm that pass the analysis cuts. Because the distributions are weighted, they are fit by the least squares method to determine the shape parameters. Fig. 5.7 shows the fitted p_T^2 and d weighted distributions for electrons from charm where the vertical scale is in arbitrary units. The p_T^2 distribution is fit to the form $exp(P1 - P2 \times p_T)$ as discussed at the beginning of this chapter. The d distribution form is $exp(P3 - P4 \times d)$. The shape parameters are $P2 = 4.5 \pm 0.5(GeV/c)^{-1}$ and $P4 = 69 \pm 9(cm)^{-1}$, which will be fixed in the fit of the data.

5.4.2 Beauty

100,000 semi-leptonic beauty decays were generated, simulated in the detector, and reconstructed. The beauty hadrons are weighted to include the trigger acceptance and

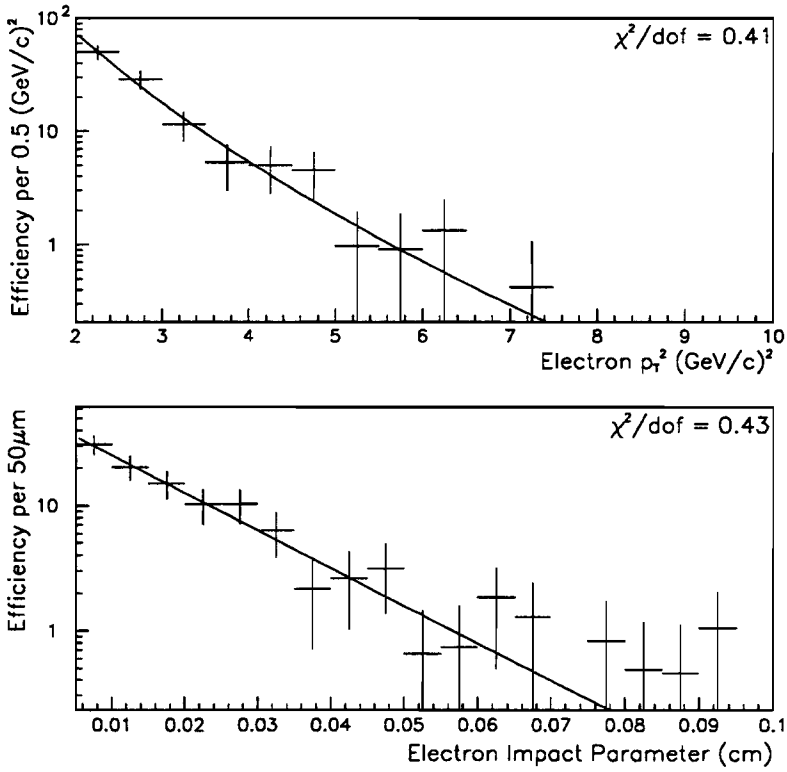

Figure 5.7: p_T^2 and d distribution of charm MC electrons.

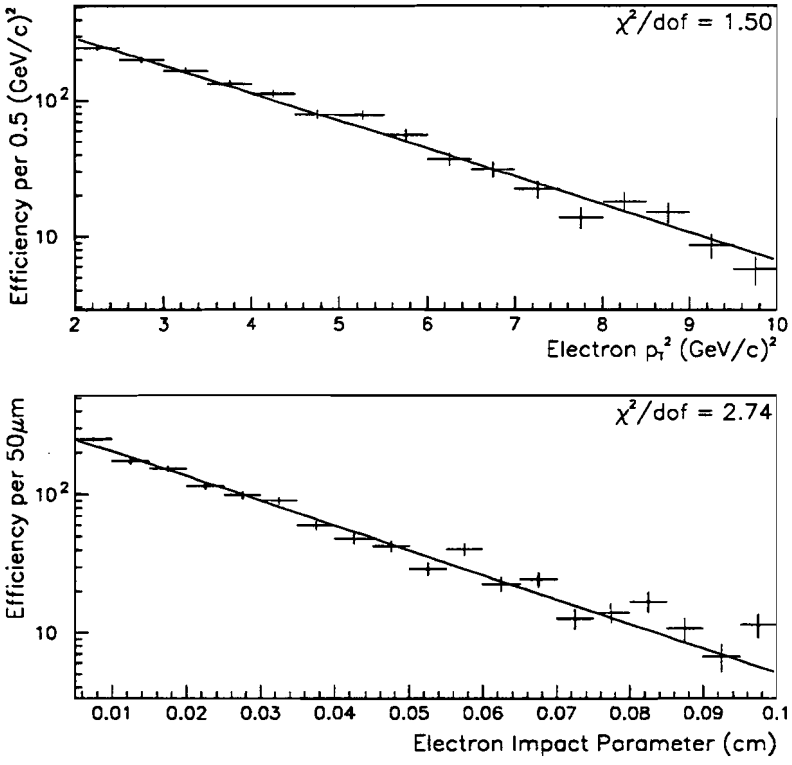

Figure 5.8: p_T^2 and d distributions of beauty MC electrons.

the b quark x_F and p_T distribution corrections. The acceptance for an electron from a semi-leptonic beauty decay is determined by including the effect of the weighting, just as was done in the case of the charm acceptance above. We find $ACC_b = 1.28 \pm .03 \times 10^{-2}$.

Plots of electron p_T^2 and d, which include the weights, are made of those electrons from beauty that pass the analysis cuts. Fig. 5.8 shows these distributions fitted using the least squares method. As in the case of the charm distributions, the vertical scale is in arbitrary units. The p_T^2 distribution is fit to the form $exp(P1 - P2 \times p_T^2)$; the d distribution form is $exp(P3 - P4 \times d)$. The shape parameters are $P2 = 0.47 \pm 0.01(GeV/c)^{-2}$ and $P4 = 41 \pm 1(cm)^{-1}$, which will be fixed in the fit of the data.

5.5 Minimum Bias Background

The number of minimum bias tracks which remain after imposing the analysis cuts is very important in this analysis. The dominant sources of background will include charged pions, because they are so abundant, and electrons from non-heavy quark processes because they will efficiently pass the electron ID cut. If these backgrounds are too large, either the heavy quark physics signals cannot be extracted from the data sample or the statistical error bars on the heavy quark physics signals will be very large.

Isolating a sample of data guaranteed to be from minimum bias events is not easy but is needed in order to measure the p_T^2 and d shapes due to minimum bias events. We wish to select a set of events recorded with the electron trigger that are consistent with being minimum bias events. The event sample must be independent from the heavy quark analysis sample. Furthermore, we want to use cuts that are similar to the analysis cuts. That way we will not need to introduce a correction if the cuts affect the p_T^2 and d shape parameters. For this study, 25% of the electron trigger sample on pair strip tapes was analyzed. Events in the minimum bias sample have exactly one reconstructed vertex, which establishes a sample independent of the heavy quark analysis sample. In addition, the minimum bias track is required to have[3] EPROB < 40 and must not have a hit in the corresponding x, y position of the muon wall. All other cuts are the same as used for the heavy quark analysis. After these cuts are imposed $\sim$1500 tracks remain from an analysis of 25% of the electron trigger data on the pair strip tapes. The fitted p_T and d distributions of these tracks are shown in Fig. 5.9. The p_T distribution is fit to $exp(P1 - P2 \times p_T)$; the d distribution form is $exp(P3 - P4/\sqrt{d})$. The shape parameters are $P2 = 3.39 \pm 0.08(GeV/c)^{-1}$ and $P4 = 0.72 \pm 0.03(cm)^{\frac{1}{2}}$, which will be fixed in the fit of the data.

[3]The EPROB cut is not necessary, but was included for historical reasons. The distribution shapes are the same with and without this cut.

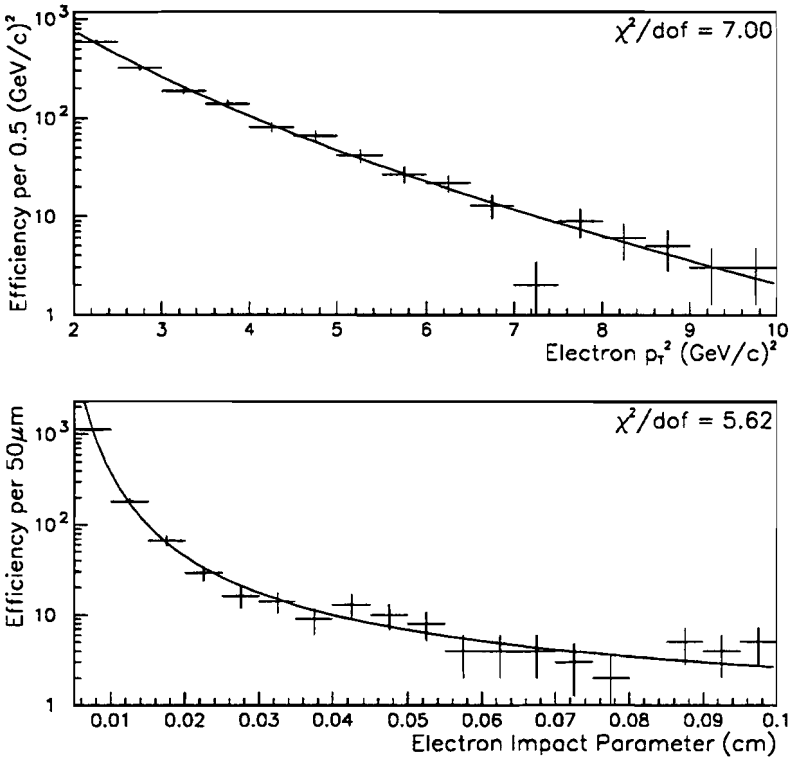

Figure 5.9: p_T^2 and d distribution of background tracks.

5.5.1 Estimate of the Number of Minimum Bias $e^{\pm}$ in the Analysis Sample

Since electrons and pions might be expected to be the dominant sources of background, it is of interest to estimate their expected yields after the analysis cuts are imposed. In this section, we make a estimate of the number of electrons from minimum bias sources in the heavy quark analysis sample. The following section makes an estimate of the pion background. Later, these results will be compared to the fit results as a consistency check.

To estimate the number of minimum bias electrons we analyze the minimum bias sample of tracks mentioned in the previous section. On this sample, we impose all analysis cuts except that we require exactly one reconstructed vertex. From this sample, 21 tracks pass the cuts. Since this study is made from 25% of the electron trigger sample, we expect this set of cuts to yield 84 tracks in the full sample. These tracks are assumed to be electrons from either minimum bias or charm events. Possible sources of minimum bias electrons are photon conversions from $\pi^0 \rightarrow 2\gamma$ decays, direct decays of light mesons and semi-leptonic decays of strange particles. We now need to estimate the amount of charm "contamination" in this sample. We begin by imposing these cuts on charm MC events. The charm acceptance, without any weighting, is $ACC(back) = (0.9 \pm 0.1) \times 10^{-4}$. The amount of charm in the background can be estimated by calculating the yield from a cross section calculation

$$\begin{aligned} N_{back}(charm) &= \mathcal{L} \times \sigma_{c\bar{c}} \times B(c\bar{c} \rightarrow eX) \times ACC(back) \\ &= (278{,}000 nucl/\mu b) \times (14 \pm 3)\mu b/nucl \times 0.21 \times (0.9 \pm 0.1) \times 10^{-4} \\ &= 74 \pm 18, \end{aligned}$$

where $N_{back}(charm)$ is the number of electrons from charm in the minimum bias background sample, $\mathcal{L}$ is the integrated luminosity in units of nucleons per μb for R3 & R4 data, $\sigma(c\bar{c})$ is the total pion induced charm production cross section in units of μb per nucleon and $B(c\bar{c} \rightarrow eX)$ is the effective branching fraction to an electron for a $c\bar{c}$ event. The value used for the total charm cross section is taken from the Chapter 6. This estimate is consistent with all of the "background" electrons coming from charm. From the one sigma error on the charm estimate, we can get a limit

on the number of minimum bias electrons in this sample. Doing this, we find that of the 84 tracks, at most $84 - (74 - 18) = 28$ of them are minimum bias electrons. Recall that this was from the full electron trigger data sample requiring exactly one reconstructed vertex. To estimate the number of electrons from minimum bias events in the heavy quark analysis sample, the limit of 28 needs to be converted to a limit when the number of reconstructed vertices is three or more.

To this end, a sample of E_T(high) trigger events were studied to determine how many have one reconstructed vertex and how many have three or more reconstructed vertices. With no analysis cuts imposed on these events, we find it is four times more likely that there are three or more reconstructed vertices. Assuming these are all minimum bias events, we have at most $4 \times 28 = 112$ minimum bias electrons in the heavy quark analysis sample.

5.5.2 Estimate of the Number of Minimum Bias $\pi^{\pm}$ in the Analysis Sample

To estimate the number of charged pions from minimum bias events, all analysis cuts except for the EPROB cut are imposed on the background sample. This yields 13,120 tracks from 25% of the electron trigger sample. If we assume these are all pions, multiplying by the mis-ID probability from Table 5.1 for EPROB ≥ 99, one arrives at an estimate of

$$N(\pi) = \frac{13,120 \times (1.1 \pm 0.3) \times 10^{-3}}{0.25} = 58 \pm 16 \tag{5.5}$$

for the full data sample. A plausibility argument is made below in Section 5.6 for why there are no pions from heavy quark decays, meaning all of these pions are from minimum bias events. Possible sources of minimum bias pions are direct production from the primary, strange particle decays and secondary interactions. In addition, some of these tracks which we call pions are actually kaons or protons. We assume that their mis-identification probability is similar to that of pions so that the estimate of 58 tracks is valid for all charged hadrons.

Adding to this the estimate of the number of electrons from minimum bias events,

we find the analysis sample should have less than ~170 tracks from minimum bias events in it. We will return to this in chapter 6 when the results are discussed.

5.6 Other Sources of Background

We now consider the contamination by charged tracks from heavy quark decays that are not electrons. The effect of this would be to add more events to the heavy quark yields from the data fit, falsely increasing the cross section. To estimate the expected contamination of the heavy quark electron signal, consider the case of pions from charm decays. An estimate of the relative contamination of the electron signal due to pions can be made given the electron ID efficiency and the pion mis-ID probability from Table 5.1 for EPROB ≥ 99 and the relative abundance of pions from charm to electrons from charm.

Suppose there are (on average) ten times more pions than electrons in heavy quark decays and that, neglecting particle identification, the imposed analysis cuts do not change this ratio. Then, for every electron that passes the EPROB cut, there are also $N(\pi)$ pions that pass, where

$$N(\pi) = \frac{A(\frac{\pi}{e}) \times P(\pi \rightarrow e)}{P(\pi \rightarrow e)} = \frac{10 \times 1.1 \times 10^{-3}}{0.19} \simeq .05, \tag{5.6}$$

$A(\frac{\pi}{e})$ is the abundance of pions relative to charm, $P(\pi \rightarrow e)$ is the pion mis-ID probability and $P(e \rightarrow e)$ is the electron ID probability. From this, we see that the contamination of the electron signal due to pions is very small. The statistical error on the charm signal will be such that this background can be neglected.

5.7 Summary

All of the tools needed to determine the cross section have been developed, which are reiterated here. The analysis is performed via a fit of the distribution of electron candidates in d vs. p_T^2 in which there are terms for minimum bias events, electrons from charm and electrons from beauty. The amplitudes of these three terms vary, but the shapes in d and p_t^2 are fixed according to the results of MC simulation (in the

case of electrons from charm and beauty) and background analysis of data. From the fit, the number of tracks from each physics type observed will be determined, then corrected for acceptance and converted into an inclusive production cross section $\sigma(Q\bar{Q}) \times B(Q\bar{Q} \rightarrow eX)$. Finally, this will be converted into a total production cross section $\sigma(Q\bar{Q})$. In the case of charm, the effect of fragmentation is model dependent and will be discussed in the next chapter. In the case of beauty, the fragmentation model does not affect $B(Q\bar{Q} \rightarrow eX)$, because all of these hadrons have nearly the same lifetime.

Chapter 6

Results

Applying the analysis cuts described in Chapter 5, 358 electron candidate tracks remain. The distribution of these candidates in d vs. p_T^2 is shown in Fig. 6.1. By collecting the fixed shape terms for minimum bias, charm and beauty events developed in Chapter 5, the function to which we fit this two dimensional distribution can be written as

$$\begin{aligned} f(d,p_T) &= exp(P1 - 3.39 \times p_T - 0.72/\sqrt{d}) + \\ & \quad exp(P2 - 4.5 \times p_T - 69 \times d) + \\ & \quad exp(P3 - 0.47 \times p_T^2 - 41 \times d). \end{aligned}$$

The first term describes the minimum bias distribution, the second term describes the charm distribution and the last term represents beauty. The fit, performed using the binned maximum likelihood method, gives the parameters and χ^2/dof shown in the first column of Table 6.2. The one-dimensional projections of the data distribution are shown in Fig. 6.2. The fit results are superimposed on the projections term-by-term. From the projections, one notes that most of the tracks are assigned to the minimum bias term. It is only at high d that the minimum bias term does not dominate.

Each fit function is integrated over the p_T^2 and d fit area to obtain the number of tracks from each type of physics process. These results are shown in Table 6.1. From this, note that the number of electrons from beauty is not significant, it is $\sim 2.5\sigma$ above zero. This means that the analysis is not sensitive to the theoretically expected beauty cross section of a few nanobarns, a result which could not have been

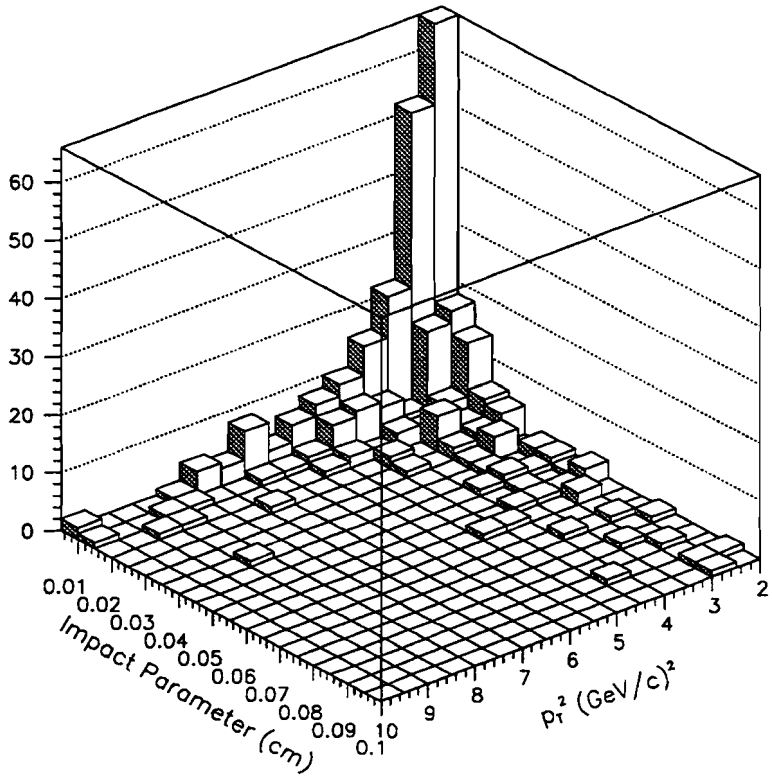

Figure 6.1: The two-dimensional d vs. p_T^2 distribution of electron candidate tracks.

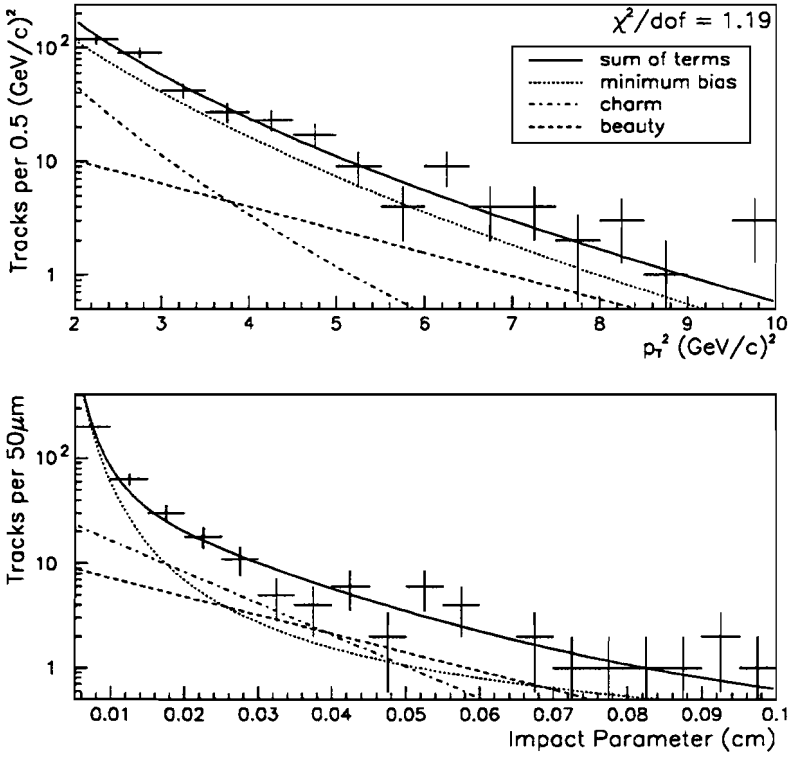

Figure 6.2: The p_T^2 and d distributions of electron candidate tracks with fit results superimposed.

anticipated before a detailed MC and data analysis. The reasons for this will be discussed later in this chapter. We can use this result to place an upper limit on the pion induced beauty cross section, which will be discussed when the total production cross sections are determined.

Table 6.1: Number of observed tracks by physics type.

Event Type	N_{obs}	N_{obs}, no beauty
Minimum Bias	236^{+23}_{-22}	243^{+23}_{-22}
$e^{\pm}$ from charm	77^{+24}_{-23}	115^{+20}_{-19}
$e^{\pm}$ from beauty	45^{+19}_{-18}	—

Because this analysis is not sensitive to beauty production, we repeat the data fit without the beauty term. The fit results are shown in the second column of Table 6.2. In Fig. 6.3, we superimpose the results of this fit on the one-dimensional data projections. Because the projections are shown on a logarithmic scale, only a small qualitative difference can be seen when comparing with the results of the previous fit. The difference is more striking when contrasting the integrated results of the two fits which are shown in Table 6.1. The increase in the minimum bias yield is not statistically significant. Most of the tracks which were previously identified with beauty decays actually come from charm decays.

Table 6.2: Fit results of the two-dimensional data distribution.

	Fit with beauty	Fit without beauty
Minimum Bias Amplitude	$0.93^{+0.09}_{-0.10}$	$0.96^{+0.09}_{-0.10}$
Charm Amplitude	$9.49^{+0.27}_{-0.35}$	$9.88^{+0.16}_{-0.18}$
Beauty Amplitude	$1.93^{+0.37}_{-0.53}$	—
χ^2/dof	1.19	1.22

We now consider the minimum bias estimates made in the previous chapter. Recall that the number of pions was estimated to be 58 ± 16; an upper limit of 112 electrons from minimum bias was also established. Using the upper limit value, the total

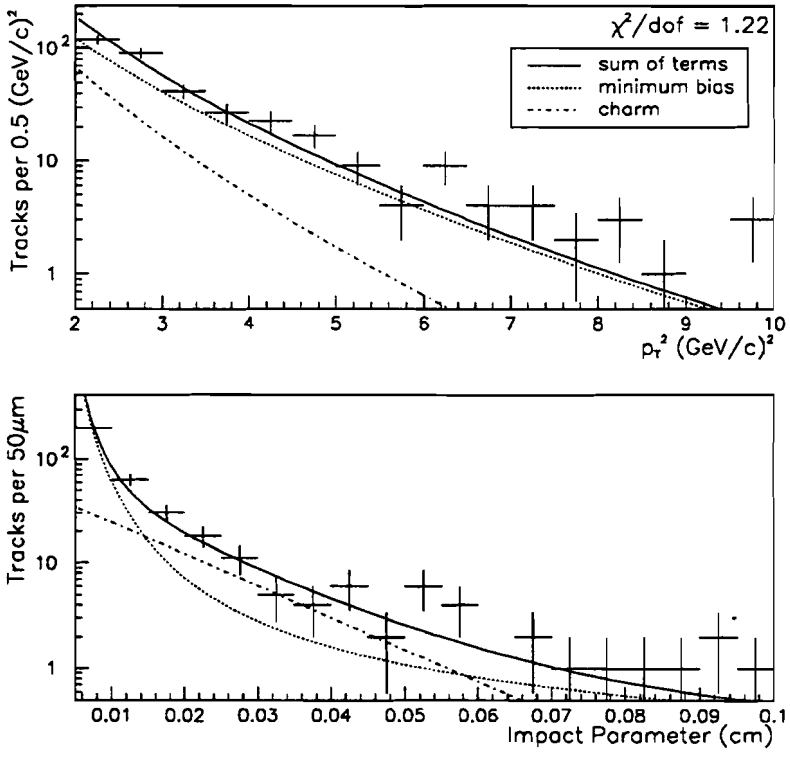

Figure 6.3: The p_T^2 and d fit projections superimposed on the data; fit with no beauty term.

number of minimum bias tracks is estimated to be 170. This is approximately 70 tracks short of the yield from the fit without a beauty term. If this estimate were not an upper limit, it would be in good agreement with the fit results because the estimate is accurate to within a factor or two or so. If we were to estimate that half of the of the 170 limit actually represented the minimum bias electron contribution, then the total minimum bias contribution would be $58 + 85 \simeq 140$, which is within a factor of two of the measured contribution $\sim$240. If the electron contribution is lower than this, we need to explain why our estimated yield is smaller than the measured yield.

Two possible explanations have been considered, but arguments made below show that only one of these is plausible. The simplest explanation is that there is another source of minimum bias tracks for which we have not accounted. One such source could be charged kaons. As mentioned in Section 5.5.2, we have assumed that kaons behave like pions as far as the electron identification is concerned. If this were a poor assumption, the estimate of the number of minimum bias hadrons would be incorrect. This background source is not considered very significant because, relative to pions, kaons are rare in minimum bias events (the number of kaons is approximately 15% of the number of pions). In addition, since kaons and pions are both hadrons, their behavior in the calorimeters cannot be very different. For these reasons, the kaon question does not present a plausible argument for the underestimate of the amount of minimum bias tracks passing the analysis cuts. The other possible explanation is due to the method for determining the pion mis-ID probability. Recall that the minimum bias pion background is estimated by using the electron mis-ID probability as determined from a study of K^0_s decays. It is possible that it is inappropriate to use this probability in an estimate of the background for the following reason. Pions from K^0_s decays, where the decay occurs between the SMDs and D1, may have a momentum distribution which is different from that of the typical pion momentum distribution and the mis-ID probability may be momentum dependent. It is very unlikely that this would change the estimated number of pions by more than a factor of two. In conjunction with a measurable electron contribution, this could approximate the measured yield.

6.1 The Heavy Quark Production Cross Sections

The cross section for the production of a $Q\bar{Q}$ pair can be expressed as

$$\sigma_{Q\bar{Q}} = \frac{N_{Q\bar{Q}}^{pro}}{N_{inc}} \frac{1}{N_{AV} A \sum_{i=1}^{N_f} t_i \rho_i / A^{\alpha}} \tag{6.1}$$

where the sum is over target foils (including the scintillator which detects target interactions), $N_{Q\bar{Q}}^{pro}$ is the number of $Q\bar{Q}$ pairs produced, N_{inc} is the integrated π^+ beam flux, t_i is the thickness of foil i in cm, $N_{AV}A$ is the number of nucleons per mole of target material and ρ_i/A^{α} is the effective density of target foil i in moles per cm^3.

The parameter α accounts for the atomic mass dependence of the cross section, which has been an item of interest for several years. To determine the cross section per nucleon one must assume some atomic mass dependence of the charm cross section. The standard parameterization of this dependence is through A^{α}. If the interaction producing the $Q\bar{Q}$ pair is characterized by large q^2 processes, the production is a short range phenomenon. This means that each target parton can be considered free, meaning the nucleus does not affect the cross section and $\alpha = 1$. If however, the interaction is a low q^2 process, production is a long range phenomenon. In this case, the fact that the partons are part of a bound nuclear state has the effect of reducing the total cross section for the following reason. Assuming the nucleus to be a sphere of uniform density, the sphere has radius $r \sim A^{1/3}$. The beam particle sees this sphere as a disk of radius r where $\sigma \sim r^2 \sim A^{2/3}$. These values represent upper and lower bounds on α. Interactions characterized by a q^2 between these two would mean α is somewhere between 2/3 and 1. E769 has recently published the result of a study of the A dependence of pion induced charm production [43] which finds $\alpha = 1.00 \pm 0.05 \pm 0.02$. Therefore, in this analysis, we assume $\alpha = 1$ for both charm and beauty[1] production. Substituting this into Eq. 6.1, the atomic mass of the target material no longer appears explicitly.

[1]There are no measurements of the A dependence of beauty production.

For this analysis, $N^{pro}_{Q\bar{Q}}$ can be rewritten as

$$N^{pro}_{Q\bar{Q}} = \frac{N^{obs}_{Q\bar{Q}\to eX}}{ACC_{Q\bar{Q}\to eX} \times B(Q\bar{Q} \to eX)} \tag{6.2}$$

where $N^{obs}_{Q\bar{Q}\to eX}$ is the number of semi-leptonic decays observed, $ACC_{Q\bar{Q}\to eX}$ is the overall acceptance for the decay and $B(Q\bar{Q} \to eX)$ is the fraction of the time one of the $Q\bar{Q}$ pair quarks decays semi-leptonically. The acceptance for both hadrons to decay semi-leptonically in the event is negligible.

Substituting Eq. 6.2 into Eq. 6.1 and multiplying both sides by $B(Q\bar{Q} \to eX)$ we obtain

$$\sigma(Q\bar{Q}) \times B(Q\bar{Q} \to eX) = \frac{N^{obs}_{Q\bar{Q}\to eX}}{N_{inc} ACC_{Q\bar{Q}\to eX}} \frac{1}{N_{AV} \sum_{i=1}^{N_I} t_i \rho_i}. \tag{6.3}$$

We have all of the information we need to calculate this quantity. For the fit that includes a beauty term, we find $\sigma(b\bar{b}) \times B(b\bar{b} \to eX) = 12.7^{+5.4}_{-4.9}$ nb and $\sigma(c\bar{c}) \times B(c\bar{c} \to eX) = 1.95^{+0.61}_{-0.59}\mu$b. For the fit without the beauty term, we find $\sigma(c\bar{c}) \times B(c\bar{c} \to eX) = 2.90^{+0.51}_{-0.48}\mu$b. These values will be rounded off after the total cross section is calculated.

To calculate the total cross sections, we need to know $B(Q\bar{Q} \to eX)$. Since all beauty hadrons have the same semi-leptonic branching fraction (see Section 4.4), we use the PDG value for B mesons $B(B \to eX) = 0.107 \pm 0.005$, from which we have $B(b\bar{b} \to eX) = 0.214 \pm 0.010$. The error on the branching fraction will be propagated into the total cross section in Section 6.2 when the systematic errors are discussed. From this effective branching fraction the total cross section is $\sigma(b\bar{b}) = 59^{+25}_{-23}$ nb, where the uncertainty is the statistical contribution only.

For charm, calculating the effective branching fraction is complicated by the choice of the fragmentation model (see Section 4.3). As a reference fragmentation model shown in Table 6.3, we choose a slightly modified version of the MC fragmentation model (see Table 4.2). A comparison shows that our modified model assumes there are only four species of charm hadrons, those with the largest fragmentation fractions. From our reference model we obtain $B(c\bar{c} \to eX) = 0.209$. We defer the discussion of its error until Section 6.2 since it is a source of systematic error. Using this value

for the effective branching fraction, we find $\sigma(c\bar{c}) = 9.3^{+2.9}_{-2.8}\mu$b for the fit that includes a beauty term and $\sigma(c\bar{c}) = 13.9^{+2.4}_{-2.3}\mu$b for the fit without a beauty term. The errors represent the statistical uncertainty on the measurements.

Table 6.3: Charm MC fragmentation and branching fractions (c.c. implicit).

Hadron	Fragmentation	$B(X_c \to eX)$
D^0	0.59	0.070
D^+	0.29	0.182
D_s^+	0.09	0.100(est)
Λ_c^+	0.03	0.045

6.2 Systematic Error

Systematic errors are those uncertainties that are not due to the statistical error of the measurement. They include such things as model dependencies and the effects of other measurements on this measurement. The systematic errors that have been studied are the effects due to

- $B(b\bar{b} \to eX)$,
- the charm fragmentation model,
- the charm hadron x_F and p_T distributions,
- the charm and beauty acceptances,
- the p_T shape of electrons from charm,
- the d shape of electrons from charm,
- the p_T shape of electrons from beauty,
- the d shape of electrons from beauty,
- the p_T shape of minimum bias tracks,

- the d shape of minimum bias tracks,
- the trigger shape uncertainty.

Fragmentation Models

The first two items in this list describe the probability that the respective heavy quark event produces a hadron which decays to an electron. We have already stated that $B(b\bar{b} \rightarrow eX) = 0.214 \pm 0.010$; this uncertainty contributes to the systematic error on the total beauty cross section.

We have already mentioned that the charm fragmentation model affects the effective branching fraction because each charm hadron has a different value of $B(X(c) \rightarrow eX)$. The fragmentation model also changes the shape of the d distribution of electrons, because electron d is strongly correlated to hadron lifetime. Since this changes the fixed shape of the d distribution, the result of the two dimensional data fit is modified. Thus $\sigma(b\bar{b} \rightarrow eX)$, $\sigma(c\bar{c} \rightarrow eX)$ and the total cross sections are affected.

Though the correct fragmentation model is not known, choices are constrained by experimental measurement. First, it is known from NA32 [9] (230 GeV/c π beam) and E653 [12] (600 GeV/c π beam) that $\frac{\sigma(D^0/\bar{D}^0)}{\sigma(D^{\pm})} \simeq 2$ for $x_F > 0$. If we assume this holds for all x_F, the reference charm fragmentation model presented above (see Table 6.3) is consistent with these measurements.

In addition, NA32 has measured [42] the production cross sections $\sigma(\pi N \rightarrow \Lambda_c X, x_F > 0) = 4.9 \pm 1.6$ (stat$\oplus$syst)μb/nucleon and $\sigma(\pi N \rightarrow DX, x_F > 0) = 9.5 \pm 1.9$(stat$\oplus$syst) μb/nucleon, where D represents the charged and neutral D mesons. From this, an estimate of $f(c \rightarrow \Lambda_c)$ can be obtained by assuming that the sum of these two cross sections represents the total charm production cross section (which is approximately true excluding D_s production). This follows from arguments similar to those made in Section 1.3, but now includes Λ_c production. From NA32, we then estimate

$$f(c \rightarrow \Lambda_c) = \frac{\sigma(\pi N \rightarrow \Lambda_c X, x_F > 0)}{\sigma(\pi N \rightarrow \Lambda_c X, x_F > 0) + \sigma(\pi N \rightarrow DX, x_F > 0)} = 0.34 \pm 0.09 \quad (6.4)$$

This information can be used to estimate the systematic error due to the charm fragmentation model uncertainty in the following way. We use two models describing

c quark fragmentation. The first model is the reference model constructed earlier from which the central value of $B(c\bar{c} \rightarrow eX)$ was determined. Its Λ_c fragmentation fraction is low according to the above estimate, but the error on $f(c \rightarrow \Lambda_c)$ is large. A reasonable alternate model would be one with $f(c \rightarrow \Lambda_c) = 0.2$, consistent with the NA32 measurement. To calculate the systematic error due to the fragmentation model uncertainty, one would then determine the total charm and beauty cross sections for each model. The systematic error contribution for the cross section of interest is then half of the cross section difference as determined from the two models. Instead of this, we choose $f(c \rightarrow \Lambda_c) = 0.1$ so that the systematic error is simply the difference of the total cross sections as determined from the two models. Our alternate model is made complete by imposing the measured D^0 to D^+ production ratio and using $f(c \rightarrow D_s^+) = 0.1$. The result of this set of constraints is shown in Table 6.4 along with the reference model. The effective branching fraction from the alternate model is $B(c\bar{c} \rightarrow eX) = 0.201$, from which we estimate $B(c\bar{c} \rightarrow eX) = 0.209 \pm 0.008$.

Table 6.4: Charm fragmentation models and branching fractions.

Hadron	$f(c \rightarrow e)$ reference model	$f(c \rightarrow e)$ alternate model	$B(X_c \rightarrow eX)$
D^0	0.59	0.53	0.070
D^+	0.29	0.27	0.182
D_s^+	0.09	0.10	0.100
Λ_c^+	0.03	0.10	0.045

Since each model gives a different charm d shape, the systematic error due to this shape is correlated with the branching fraction uncertainty. So as not to overestimate the total systematic error due to the charm fragmentation model, we proceed as follows. For each fragmentation model, we fit the data distribution and calculate $\sigma(Q\bar{Q} \rightarrow eX)$. For each result, we use the corresponding $B(c\bar{c} \rightarrow eX)$ to calculate the total charm cross section. The difference in the total cross section derived from the two models is the systematic error due to the fragmentation model. We introduce a notation that will be used throughout this section to represent the systematic error contributions. The quantity $\delta\sigma_Q(\mathrm{X})$ is the systematic error of the total $Q\bar{Q}$

quark production cross section due to source X. In addition, the quantity $\delta\sigma_{Qe}$(X) represents the systematic error of the cross section times branching fraction due to source X. With this notation, for the fit with a beauty term, we find $\delta\sigma_c$(charm frag)= 0.69μb and $\delta\sigma_b$(charm frag)= 1.2 nb. For the fit without a beauty term, we find and $\delta\sigma_c$(charm frag)= 1.19μb. These errors are added in quadrature with the other systematic errors when the final result is presented below.

Heavy Quark x_F and p_T Distributions

The x_F and p_T distributions predicted by QCD for the b-quark are expected to be accurate because the mass of the quark is so large. Therefore, the systematic error due to the theoretical uncertainty in these distributions is not considered. The systematic error due to the charm hadron distributions is estimated from the uncertainty of the experimental measurements for charged and neutral D mesons. The effect of changing these distributions is to modify the weights used in the MC analysis, thus changing the p_T^2 and d distributions of electrons from charm. This in turn changes the fit results affecting both charm and beauty yields. The error on the beauty measurement due to the charm x_F uncertainty is $\delta\sigma_{be}(x_F) = ^{+0.07}_{-0.08}$nb. For the charm cross sections the uncertainties are $\delta\sigma_{ce}(x_F) = ^{+0.013}_{-0.010}$ μb for the fit with a beauty term and $\delta\sigma_{ce}(x_F) = ^{+0.012}_{-0.010}$ μb for the fit without a beauty term. Furthermore, the error on the beauty measurement due to the charm p_T uncertainty is $\delta\sigma_{be}(p_T) = ^{+0.41}_{-0.42}$nb for beauty. For the charm cross sections, the uncertainties are $\delta\sigma_{ce}(p_T) = ^{+0.043}_{-0.040}$ μb for the fit with a beauty term and $\delta\sigma_{ce}(p_T) = ^{+0.029}_{-0.031}$ μb for the fit without a beauty term. The precision of the errors is not as high as implied by the number of digits retained. The values will be truncated once the systematic errors are combined.

Acceptance for $B(Q\bar{Q} \rightarrow eX)$

The charm and beauty acceptances contribute only to the systematic error of their respective cross sections $\sigma(Q\bar{Q}) \times B(Q\bar{Q} \rightarrow eX)$. These errors are taken from the square root of the number of electrons from MC simulation that pass the cuts. The error on the beauty cross section due to the beauty acceptance uncertainty is $\delta\sigma_{be}(ACC) = \pm 0.28$ nb. The errors on the charm cross sections due to the charm

acceptance uncertainty are $\delta\sigma_{ce}(ACC) = ^{+0.138}_{-0.121}$ μb for the fit with a beauty term and $\delta\sigma_{ce}(ACC) = ^{+0.201}_{-0.176}$ μb for the fit without a beauty term.

Electron d and p_T Shapes

The next six items in the systematic error list shown at the beginning of this section are the uncertainties due to the fixed parameters in the two dimensional data fits. Each time these are varied, the fits must be repeated, such that the results for both charm and beauty cross sections are changed. The systematic error contributions to the beauty cross section are

$$\begin{aligned}
\delta\sigma_{be}(c\ p_T) &= ^{+1.57}_{-1.36} nb \\
\delta\sigma_{be}(c\ d) &= ^{+.72}_{-.59} nb \\
\delta\sigma_{be}(b\ p_T) &= ^{+.23}_{-.24} nb \\
\delta\sigma_{be}(b\ d) &= ^{+.30}_{-.31} nb \\
\delta\sigma_{be}(m\ p_T) &= ^{+.97}_{-.99} nb \\
\delta\sigma_{be}(m\ d) &= ^{+.28}_{-.30} nb.
\end{aligned}$$

The errors on the charm cross section for the fit including a beauty term are

$$\begin{aligned}
\delta\sigma_{ce}(c\ p_T) &= ^{+.196}_{-.170} \mu b \\
\delta\sigma_{ce}(c\ d) &= ^{+.034}_{-.041} \mu b \\
\delta\sigma_{ce}(b\ p_T) &= ^{+.028}_{-.029} \mu b \\
\delta\sigma_{ce}(b\ d) &= ^{+.019}_{-.018} \mu b \\
\delta\sigma_{ce}(m\ p_T) &= ^{+.088}_{-.082} \mu b \\
\delta\sigma_{ce}(m\ d) &= ^{+.117}_{-.063} \mu b.
\end{aligned}$$

For the fit without a beauty contribution, the errors on the charm cross section are

$$\begin{aligned}
\delta\sigma_{ce}(c\ p_T) &= ^{+.147}_{-.158} \mu b \\
\delta\sigma_{ce}(c\ d) &= ^{+.086}_{-.091} \mu b \\
\delta\sigma_{ce}(m\ p_T) &= ^{+.003}_{-.004} \mu b \\
\delta\sigma_{ce}(m\ d) &= ^{+.101}_{-.100} \mu b.
\end{aligned}$$

Trigger Parameterization

Finally, there is the uncertainty due to the parameterization of the trigger and its use in the MC simulation for the trigger acceptance. Determining this error precisely is difficult because the shape is parameterized by four parameters which are correlated to one another. Varying the parameters of the trigger shape about their central values shows that their contribution to the total systematic error is negligible compared to other error sources. As a result, the systematic error due to the trigger parameterization is neglected.

Total Systematic Error

Excluding the errors due to the charm fragmentation model and the effective branching fraction for beauty, the systematic errors on the quantity $\sigma(Q\bar{Q}) \times B(Q\bar{Q} \to eX)$ are summarized in Table 6.5 for beauty and in Table 6.6 for charm. In each table, the quadrature sum of the uncertainties is shown at the bottom. Including these values with the central values from Section 6.1, we obtain

$$\begin{aligned}
\sigma(b\bar{b}) \times B(b\bar{b} \to eX) &= 12.7^{+5.4}_{-4.9}(stat)^{+2.1}_{-1.9}(syst)nb \\
\sigma(c\bar{c}) \times B(c\bar{c} \to eX) &= 1.95^{+0.61}_{-0.59}(stat)^{+.29}_{-.24}(syst)\mu b \\
\sigma(c\bar{c}) \times B(c\bar{c} \to eX) &= 2.90^{+0.51}_{-0.48}(stat)^{+.28}_{-.27}(syst)\mu b.
\end{aligned}$$

6.3 Total Cross Sections

We are now ready to determine the total cross sections including their systematic errors. For beauty, we have $\sigma(b\bar{b}) \times B(b\bar{b} \to eX) = 12.7^{+5.4}_{-4.9}(\text{stat})^{+2.1}_{-1.9}(\text{syst})$ nb from the previous section. From Section 6.2, we also know $B(b\bar{b} \to eX) = 0.214 \pm 0.010$ and $\delta\sigma_b$(charm frag)= 1.2 nb. Combining this information and rounding off the result, we find $\sigma(b\bar{b}) = 59^{+25}_{-23}(\text{stat})^{+12}_{-11}(\text{syst})$nb, which is the total pion induced beauty production cross section per nucleon. Converting this to a 90% confidence level upper limit (1.64σ), we have $\sigma(b\bar{b}) < 105$ nb. These results, along with the information

Table 6.5: Systematic errors for $\sigma(b\bar{b}) \times B(b\bar{b} \rightarrow eX)$ (nb).

Source of Error	Uncertainty
charm hadron x_F	$+0.07\ -0.08$
charm hadron p_T	$+0.41\ -0.42$
beauty acceptance	$+0.28\ -0.28$
charm $e^{\pm}p_T$	$+1.57\ -1.36$
charm $e^{\pm}d$	$+0.72\ -0.59$
beauty $e^{\pm}p_T$	$+0.23\ -0.24$
beauty $e^{\pm}d$	$+0.30\ -0.31$
min bias $e^{\pm}p_T$	$+0.97\ -0.99$
min bias $e^{\pm}d$	$+0.28\ -0.30$
Quadrature Sum	$+2.10\ -1.92$

Table 6.6: Systematic errors for $\sigma(c\bar{c}) \times B(c\bar{c} \rightarrow eX), (\mu b)$.

Source of Error	Uncertainty (fit with beauty)	Uncertainty (fit without beauty)
charm hadron x_F	$+.013\ -.010$	$+.012\ -.010$
charm hadron p_T	$+.043\ -.040$	$+.029\ -.031$
charm acceptance	$+.138\ -.121$	$+.201\ -.176$
charm $e^{\pm}p_T$	$+.196\ -.170$	$+.147\ -.158$
charm $e^{\pm}d$	$+.034\ -.041$	$+.086\ -.091$
beauty $e^{\pm}p_T$	$+.028\ -.029$	—
beauty $e^{\pm}d$	$+.019\ -.018$	—
min bias $e^{\pm}p_T$	$+.088\ -.082$	$+.003\ -.004$
min bias $e^{\pm}d$	$+.117\ -.063$	$+.101\ -.100$
Quadrature Sum	$+.289\ -.242$	$+.284\ -.274$

used to derive them, are summarized in Table 6.7. In this table, the information is truncated to reflect the precision of the measurements.

To obtain the total pion induced charm production cross section per nucleon, from the previous section recall $\sigma(c\bar{c}) \times B(c\bar{c} \rightarrow eX) = 1.95^{+0.61}_{-0.59}(\text{stat})^{+.29}_{-.24}(\text{syst})\mu\text{b}$ for the fit including a beauty term and $\sigma(c\bar{c}) \times B(c\bar{c} \rightarrow eX) = 2.90^{+0.51}_{-0.48}(\text{stat})^{+.28}_{-.27}(\text{syst})\mu\text{b}$ for the fit without a beauty term. In addition, from Section 6.2 recall $B(c\bar{c} \rightarrow eX) = 0.209 \pm 0.008$, $\delta\sigma_c(\text{charm frag}) = 0.69\mu\text{b}$ for the fit which includes a beauty term and $\delta\sigma_c(\text{charm frag}) = 1.19\mu\text{b}$ for the fit without a beauty term. Combining this information, we find $\sigma(c\bar{c}) = 9.3^{+2.9}_{-2.8}(\text{stat})^{+1.5}_{-1.3}(\text{syst})\mu\text{b}$ for the fit including a beauty term and $\sigma(c\bar{c}) = 13.9^{+2.4}_{-2.3}(\text{stat}) \pm 1.8(\text{syst})\mu\text{b}$ for the fit without a beauty term. These results, along with the information used to derive them, are also summarized in Table 6.7. The information is truncated to reflect the precision of the measurements.

Table 6.7: Summary of cross section results with systematic errors.

Description	Fit with Beauty Term	Fit without Beauty Term
Minimum Bias	236^{+23}_{-22}	243^{+23}_{-22}
$e^{\pm}$ from charm	77^{+24}_{-23}	115^{+20}_{-19}
$e^{\pm}$ from beauty	45^{+19}_{-18}	—
χ^2/DOF of fit	1.19	1.22
$\sigma_{b\bar{b}/nucl.} \times B(b\bar{b} \rightarrow eX)$	$13 \pm 5(stat) \pm 2(syst)nb$	—
$B(b\bar{b} \rightarrow eX)$	$.214 \pm .010$	—
$\sigma_{b\bar{b}/nucl.}$	$59^{+25}_{-23}(stat)^{+12}_{-11}(syst)$nb	—
$\sigma(b\bar{b})$ limit, 90% C.L.	$105nb$	—
$\sigma_{c\bar{c}/nucl.} \times B(c\bar{c} \rightarrow eX)$	$2.0 \pm .6(stat)^{+.3}_{-.2}(syst)\mu b$	$2.9 \pm .5(stat) \pm .3(syst)\mu b$
$B(c\bar{c} \rightarrow eX)$	.209	.209
$\sigma_{c\bar{c}/nucl.}$	$9.3^{+2.9}_{-2.8}(stat)^{+1.5}_{-1.3}(syst)$	$13.9^{+2.4}_{-2.3}(stat) \pm 1.8(syst)$

6.4 Conclusions

In Fig. 6.4 we show the total charm cross section prediction and the published data measurements which were discussed in Chapter 1. The charm cross section as determined in this analysis is superimposed on this plot. The two E769 measurements are slightly offset from the lab momentum of 250 GeV/c so that the error bars can be seen. As the figure shows, our pion induced charm production cross section is consistent with the NLO QCD prediction of 12 μb. We also see that this measurement is consistent (though slightly higher) with the trend shown by the other published measurements, which can be explained as follows. Recall that all of the other measurements shown in this figure are from exclusive decay modes of charged and neutral D mesons. The approximation we used to estimate these values, $\sigma(c\bar{c}) \simeq \sigma(D^{\pm}, x_F > 0) + \sigma(D^0/\bar{D}^0, x_F > 0)$, is an underestimate of the total cross section (by approximately 20%) because there are known production modes which have been ignored (e.g., D_s^+, Λ_c^+, etc). The support from the prediction and the exclusive mode measurements shows that our single lepton analysis is a reliable method with which to extract heavy quark cross sections.

In Fig. 6.5 we show the total beauty cross section prediction and the published data measurements which were discussed in Chapter 1. The cross section limit as determined in this analysis is also shown in this figure. The arrow on the error bar indicates that this measurement is an upper limit. With the data available today, it is an unresolved issue whether or not perturbative QCD calculations correctly predict the pion induced beauty production cross section. It is unfortunate that the pion induced beauty production cross section is so small in the lab momentum range of 300 GeV/c and under. The "knee" in the production cross section is a very sensitive region in which to make measurements and otherwise shows great promise in constraining the theoretical prediction.

The uncertainty of our beauty signal is large because the signal is small relative to the minimum bias signal. A more sensitive measurement could be made by removing more background, if the acceptance for seeing an electron from a beauty hadron decay did not decrease. One way to do this would be to follow the example of the NA10

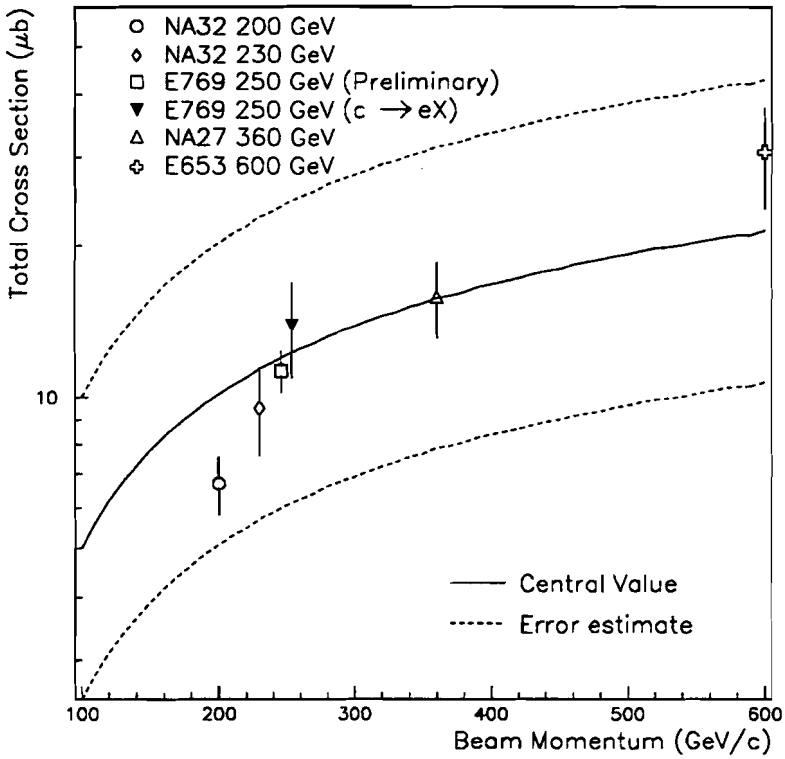

Figure 6.4: NLO QCD total pion induced charm production cross section as a function of beam energy with published measurements included.

and WA78 analyses and perform a di-lepton study. Since they have published cross sections, not limits, this would seem a logical step from a single lepton analysis. By including both electrons and muons, we would regain some of the acceptance which is lost in requiring two leptons in an event rather than just one. Such an analysis with E769 data could produce a good measurement if the vertex information in the event is used, because the NA10 and WA78 measurements have been made without this information. The utility of vertex information is apparent upon contrasting the d distributions of tracks from minimum bias, charm and beauty events as shown in figures 5.9, 5.7 and 5.8 respectively. How this information would best be utilized in a di-lepton analysis is not yet clear. One option would be to require that two leptons to pass minimal p_T and d cuts, but fit the two-dimensional distribution of only one. Another option would be to correlate the information from the two tracks, perhaps using a combined d which describes how far both tracks are from the primary vertex.

From this analysis, we are able to conclude several points. Foremost, the method is a reliable measure of the total heavy quark production cross sections, as demonstrated by the charm cross section measurement. Its sources of systematic error are different from those of exclusive mode studies, so that this measurement is complementary to the other charm cross section measurements. The fact that it yields results consistent with the exclusive mode measurements is a marvelous confirmation. Second, note that the statistical uncertainty of the charm measurement (see Table 6.7) is large relative to the measurements made from exclusive decay modes (see Table 1.2). The main reason for this is that this analysis was tuned to the observation of beauty at the expense of charm. A similar analysis (i.e., through a study of events with either a single or multiple lepton) could be performed to make an optimal charm cross section measurement. This would be of interest if the charm yield could be increased to the point that the systematic error dominated the total cross section uncertainty. Because the systematic error in this analysis is comparable to that from exclusive mode measurements, such a measurement would be competitive with other estimates of the total cross section. In addition, much of the charm systematic uncertainty is due to our lack of knowledge about charm fragmentation. As more is learned about

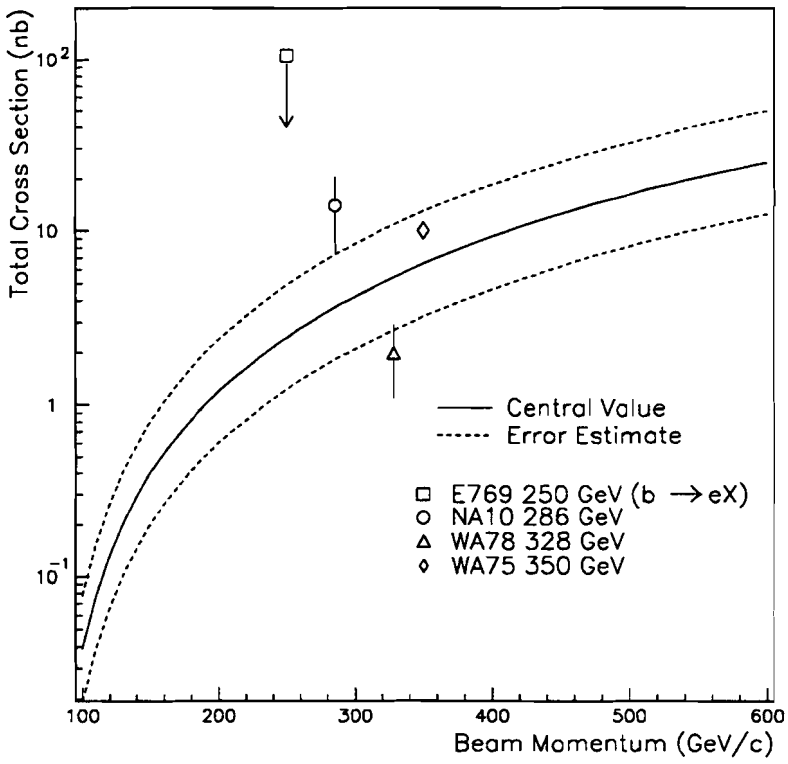

Figure 6.5: NLO QCD total pion induced beauty production cross section as a function of beam energy with published measurements included.

the fragmentation fractions, this systematic uncertainty decreases. Finally, we see the great difficulties encountered in a single lepton analysis because of the large hadronic backgrounds. This is the reason experiments are motivated to perform di- and tri-lepton analyses when measuring a small beauty signal in a large background. Though we are unable to see beauty production in the single lepton analysis, a multiple lepton analysis of E769 data shows promise especially once vertex information is included.

Appendix A

Detailed Description of the Electron Identification

A.1 Overview

A brief description of the electron identification was given in Chapter 3. In this appendix, we give a description which is intended for collaborators who wish to know about the method in more detail. Much of the information contained herein refers directly to E769 reconstruction variables which contribute to the identification of electrons. This is done in order to ease the interpretation of the code for the user. We assume here that the reader is fluent with the E769 code management system to the point that finding variables and routines poses no problem.

The task of the electron identification procedure (which is directed by the fortran routine EMPNEW) is to identify electrons in the presence of a large charged hadronic background, which are dominantly pions. For this task, we combine information from the drift chambers, electromagnetic calorimeter (SLIC) and the hadron calorimeter. Most of the work is performed using shower information from the SLIC. During reconstruction EMPNEW is called for each charged track and the returned value is stored in the EMPROB array by the track's index in the charged track list. This value of EMPROB, whose range is from zero to 100, represents the likelihood that the track is an electron based on a study performed by Rollin Morrison (the code

author) for E691. It is the value in the EMPROB array for the track of interest that is used as a cut value in the analysis to identify electrons.

A.2 Sources of $e^{\pm}$ and $\pi^{\pm}$

To be able to distinguish between $e^{\pm}$ and $\pi^{\pm}$, one must observe the performance of separate samples of electrons and pions in the spectrometer. Based on these observations, a set of characteristics are identified which can be used to distinguish the two particle types from one another. A plentiful sample of electrons can found by searching for photon conversions ($\gamma \rightarrow e^+e^-$) occurring in the target region. These are characterized by two oppositely charged particles which have very little relative transverse momentum in the region upstream of the analysis magnets. Furthermore, they must have a very small invariant mass, which would be almost zero neglecting finite detector resolution.

For pions, $K_s^0 \rightarrow \pi^+\pi^-$ decays are reconstructed. The K_s^0 is created near the target from an interaction and decays somewhere further downstream. With a proper lifetime of 2.7 cm and a typical Lorentz gamma factor of $\sim$30, it often decays in the region upstream of the analysis magnets. So, we look for two oppositely charged tracks which meet in this region and have an invariant mass near that of the kaon mass.

A.3 Charged Track Characteristics

With these samples of pions and electrons, we observe their behavior in the calorimeters as a function of several characteristics. These are

- the track momentum,
- the radial position of the energy cluster in the calorimeter,
- the amount of energy deposited in the hadrometer,
- the proximity of the extrapolated track position to the SLIC shower centroid,

- the transverse distribution of the electromagnetic shower about the centroid and
- the difference between electromagnetic calorimeter energy and the momentum measurement.

These characteristics are assumed to be uncorrelated with one another so that the contribution from each characteristic can be treated independently. To parameterize its functional dependence, each variable is typically divided into four or five bins. For each bin of a given variable, the quantities $f(e)$ and $f(\pi)$ are determined, which are respectively the fractions of electrons and pions that fall into the bin of interest.

A.4 Calculation of EMPNEW

Before we describe how the fractions f, introduced above, enter into the electron identification scheme, we define EMPNEW. For equal numbers of pions and electrons, EMPNEW is the relative probability of correctly identifying an electron, such that

$$\begin{aligned} \text{EMPNEW} &\equiv 100 \times \frac{P(e\rightarrow e)}{P(e\rightarrow e)+P(\pi\rightarrow e)} \\ &= 100 \times \frac{1}{1+\frac{P(\pi\rightarrow e)}{P(e\rightarrow e)}}, \end{aligned}$$

where $P(e \rightarrow e)$ is the probability that an electron is identified as an electron and $P(\pi \rightarrow e)$ is the probability that a pion is identified as an electron. The value of EMPNEW is then scaled to correct for the fact that the electron and pion abundances are not the same, a factor which turns out to be momentum dependent. We define the probability ratio to be

$$\frac{P(\pi \rightarrow e)}{P(e \rightarrow e)} = \prod_{i=1}^{n} \frac{f_i(\pi)}{f_i(e)}, \tag{A.1}$$

where the product is taken over the variables used to distinguish pions from electrons. In this way, the fractions of electrons and pions that fall into certain bins determine the probability that the track is an electron.

A.5 Parameterization of the Charged Track Characteristics

In regard to the electron identification procedure, we now discuss how each item listed in Section A.3 is parameterized and also discuss its relevance to particle identification. The track momentum and the radial position of the energy cluster in the calorimeter (called RAD) are combined together to form one set of fraction ratios ($\frac{f(\pi)}{f(e)}$). For each value of the IEA index, there is a fraction ratio corresponding to a momentum and energy cluster position combination. The allowed values of IEA and their meaning are shown in Table A.1. Both track momentum and shower position affect the ability to identify electrons and pions for two reasons. First, high momentum tracks produce more shower secondaries than do low momentum tracks. Thus, they are less susceptible to statistical fluctuations of the shower characteristics. Second, the central region of the SLIC is one of high track occupancy, which makes it difficult to assign calorimeter energy to the tracks.

Table A.1: The EMPNEW dependence on track momentum and radial position of the electromagnetic shower in the SLIC.

IEA	Track Momentum GeV/c)	RAD (cm)
1	$P > 20$	< 65
2	$12 < P < 20$	< 65
3	$P > 12$	> 65

For each bin of the characteristics described below, there is another fraction ratio which contributes to the product in Eq. A.1. These fractions are also a function of the IEA index. When this dependence does not appear explicitly in the discussions that follow, the binning is independent of IEA but the fraction ratios are not. Examples of explicit and implicit IEA dependence will be pointed out below.

The amount of hadrometer energy a track possesses is described by the index IH, which has the five possible values shown in Table A.2. With this classification, any track with more than 1.2 GeV in the hadrometer (E_{had}) is not an electron. The

other conditions allow for small amounts of hadrometer energy. The two entries described as "confused" are for those cases where showers overlap, usually in the central region. (Note that the IEA index does not explicitly appear. In this case, the IEA dependence affects the fraction ratios but not the hadrometer energy binning.)

Table A.2: The EMPNEW dependence on the amount of hadrometer energy possessed by a charged track.

IH	Description	
1	Not an electron	$E_{had} \geq 1.2$ GeV
2	Zero hadrometer energy	$E_{had} < 0.2$ GeV
3	Small energy	$E_{had} < 0.5$ GeV
4	Small energy, confused	$E_{had} < 1.2$ GeV
5	Very confused	

The proximity of the extrapolated track position to the SLIC shower centroid is measured by the variable $RSQD$, which is the squared difference of the two positions. The quantity $RSQD$ helps reject electron candidates whose electromagnetic character is due to a photon that hits the SLIC in the vicinity of a charged track. In addition, this information is used to separate pions from electrons because the $RSQD$ distribution for pions is larger than that for electrons. Table A.3 shows the classes of $RSQD$. (Note that this is a case where the IEA dependence appears explicitly and affects the binning in the $RSQD$ variable.)

The transverse distribution of the electromagnetic shower is characterized by its second moment ($\equiv I_2$) which is calculated from the signals of the central channel and two channels on both sides of the central channel for a given view. This is done in both the u and v views, and the smaller of the two is retained. The second moment is defined to be

$$I_2 = \frac{\sum_{i=1}^{5} E_i[x_i - POS]^2}{\sum_{i=1}^{5} E_i}, \tag{A.2}$$

Table A.3: The EMPNEW dependence on the difference between the track position and SLIC shower centroid.

IEA	$RSQD$ (cm^2)
1	$RSQD < 4.$
	$RSQD \geq 4.$
2	$RSQD < 1.92$
	$1.92 \leq RSQD < 2.24$
	$2.24 \leq RSQD < 4.$
	$RSQD > 4.$
3	$P > 12$
	$RSQD \geq 4.$

where

$$POS = \frac{\sum_{i=1}^{5} E_i x_i}{\sum_{i=1}^{5} E_i} \tag{A.3}$$

and x_i refers to the position of strip i. Table A.4 shows the binning in units of the second moment, demonstrating the meaning of the IW index. In the table, "small counter" refers to channels of single width, while "large counter" refers to channels of double width (see Section 2.10.1). Since pions tend to make showers which are wider than those of electrons of the same momentum, the second moment is a useful test of particle type.

The difference between the track's electromagnetic calorimeter energy and the momentum measured in the drift chambers is characterized in units of significance by the IR index. This is done by calculating the charged track's energy from the momentum assuming it has the mass of a π^0; the result is stored in the $P4CAL$ array. In this way significant deviations of the energy from the momentum can be determined, indicating that the track is a pion. This is true because of energy lost via punch-through or from a shower which is not transversely contained. The values of IR are shown in Table A.5 where the significance is defined as

$$\sigma = \frac{ESL - P4CAL}{DECAL}. \tag{A.4}$$

Table A.4: The EMPNEW dependence on the second moment of the electromagnetic shower.

IW	Description	(cm^2)
1	not an electron	
2	small counter	$-3.0 < I_2 < 0.0$
3	small counter	$0.0 < I_2 < 1.8$
4	small counter	$1.8 < I_2 < 5.0$
5	large counter	$-3.0 < I_2 < 0.0$
6	large counter	$0.0 < I_2 < 1.8$
7	large counter	$1.8 < I_2 < 5.0$
8	no information	

The reconstruction arrays ESL and $DECAL$ contain respectively the track's SLIC energy and the uncertainty of that energy.

Table A.5: The EMPNEW dependence on the significance of the momentum and SLIC energy difference.

IR	Description
1	$-4.0 < \sigma < -2.2$
2	$-2.2 < \sigma < -1.1$
3	$-1.1 < \sigma < 1.1$
4	$1.1 < \sigma < 2.5$
5	$2.5 < \sigma < 5.0$

The final component of the EMPNEW calculation corrects the fact that the number of pions and electrons for a given value of IEA and $RSQD$ are not equal. This correction is made by introducing a factor which multiplies the probability ratio $\frac{P(\pi \to e)}{P(e \to e)}$. The ratio used is a function of the IEA index, and is consequently momentum dependent. The reason for this is that the ratio of the number of pions to electrons is different for different values of IEA.

Bibliography

[1] W. Marciano, *Annu. Rev. Nucl. Part. Sci.* **41** (1991) 469.

[2] K. Hikasa, *et.al.*, *Phy. Rev.*, **D45** (1992).

[3] P. Nason, S. Dawson and R. K. Ellis, *Nucl. Phys.* **B327** (1988) 49.

[4] E. L. Berger, *Heavy Flavor Production*, Proceedings of a NATO Advanced Research Workshop on QCD Hard Hadronic Processes, Brad Cox ed. (1987).

[5] G. Altarelli, *et.al.*, *Nucl. Phys.* **B308** (1988) 724.

[6] M. Mangano, *et.al.*, IFUP-TH-37/92 (1992).

[7] B. W. Duke and J. F. Owens, *Phys. Rev.*, **D30** (1984) 49.

[8] J. F. Owens, *Phys. Rev.*, **D30** (1984) 943.

[9] S. Barlag, *et.al.*, *Z. Phys.*, **C49** (1991) 555.

[10] A. Reis, D^+D^0 *and* D^{*+} *Cross Sections in E769*, Internal Memorandum (1993).

[11] M. Aguilar-Benitez, *et.al.*, *Phys. Lett.*, **B161** (1985) 400.

[12] K. Kodama, *et.al.*, *Phys. Lett.*, **B284** (1992) 461.

[13] J. P. Albanese, *et.al.*, *Phys. Lett.*, **B158** (1985) 186.

[14] M. G. Cantanesi, *et.al.*,*Phys. Lett.*, **B202** (1988) 453.

[15] P. Bordalo, *et.al.*, *Z. Phys.*, **C39** (1988) 7.

[16] D. J. Summers, *A Study of the Decay* $D^0 \to K^-\pi^+\pi^0$ *in High Energy Photoproduction*, Ph.D. thesis, UC Santa Barbara (1984).

[17] J. Raab, *Lifetime Measurements of the Three Pseudoscaler D-Mesons*, Ph.D. Thesis, UC Santa Barbara (1987).

[18] T. Browder, *A Study of* $D^0\bar{D}^0$ *Mixing*, Ph.D. Thesis, UC Santa Barbara (1988).

[19] R. Jedicke, *Flavour Dependence of Hadroproduced Charm-Strange Mesons*, Ph.D. Thesis, University of Toronto (1991).

[20] M. Benot, *et.al.*, *Nucl. Instr. Meth.*, **105** (1972) 431.

[21] D. Errede, *et.al.*, *Nucl. Instr. Meth.*, **A309** (1991) 386.

[22] J. D. Jackson, *Classical Electrodynamics*, Wiley, New York (1975).

[23] P. E. Karchin, *et.al.*, *IEEE Trans. Nucl. Sc.*, **NS-32(1)** (1985) 612.

[24] W. R. Ross, *Measurement of the Decays of the Neutral D to Two Charged Pions and Two Charged Kaons*, Ph.D. Thesis, Yale University (1992).

[25] Z. Wu, *The Feynman-x Dependence of* $D^{\pm}$ *Mesons in* π^-*-Nucleon Interactions*, Ph.D. Thesis, Yale University (1991).

[26] J. P. Avondo, *et.al.*, *Nucl. Instr. Meth.*, **A241** (1985) 107.

[27] D. Green, *A Silicon Detector Readout System Using Commercially Available Items*, FERMILAB-TM-1399 (1986).

[28] D. Bartlett, *et.al.*, *Nucl. Instr. Meth.*, **A260** (1987) 55.

[29] V. K. Bharadwaj, *et.al.*, *Nucl. Instr. Meth.*, **155** (1978) 411.

[30] V. K. Bharadwaj, *et.al.*, *Nucl. Instr. Meth.*, **228** (1985) 283.

[31] T. Ferbel, *Experimental Techniques in High Energy Physics*, Frontiers in Physics Series, Addison-Wesley, Menlo Park (1987).

[32] D. J. Summers, *Nucl. Instr. Meth.*, **228** (1985) 290.

[33] C. Stoughton, D. J. Summers, *Computers in Physics*, **6** (1992) 371.

[34] J. A. Appel, *et.al.*, *Nucl. Instr. Meth.*, **A243** (1986) 361.

[35] C. Gay, and S. Bracker, *IEEE Trans. Nucl. Sc.*, **NS-34(4)** (1987) 870.

[36] T. Sjöstrand, *Comp. Phys. Comm.*, **39** (1986) 347.

[37] B. Nilsson-Almqvist, *et.al.*, *Comp. Phys. Comm*, **43** (1987) 378.

[38] R. Fernow, *Introduction to experimental particle physics*, Cambridge University Press, Cambridge (1986) 48.

[39] G. A. Alves, *et.al.*, *Phys. Rev. Lett.*, **69** (1992) 3147.

[40] D. Buskulic, *et.al.*, *Phys. Lett.*, **B297** (1992) 449.

[41] R. K. Ellis and C. Quigg, *FNAL Report N. FN-445* (1987).

[42] S. Barlag, *et.al.*, *Phys. Lett.*, **B247** (1990) 113.

[43] G. A. Alves, *et.al.*, *Phys. Rev. Lett.*, **70** (1993) 722.